6-1-2023

The Giant Accreting Protoplanet Survey (Gaplanets)—Results from a 6 Yr Campaign to Image Accreting Protoplanets

Katherine B. Follette
Amherst College

Laird M. Close
The University of Arizona

Jared R. Males
The University of Arizona

Kimberly Ward-Duong
Smith College, kwardduong@smith.edu

William O. Balmer
Amherst College

See next page for additional authors

The Astronomical Journal, 165:225 (45pp), 2023 June https://doi.org/10.3847/1538-3881/acc183

The Giant Accreting Protoplanet Survey (GAPlanetS)—Results from a 6 yr Campaign to Image Accreting Protoplanets

Katherine B. Follette[1], Laird M. Close[2], Jared R. Males[2], Kimberly Ward-Duong[3], William O. Balmer[1,4,5], Jéa Adams Redai[1,6], Julio Morales[7], Catherine Sarosi[1], Beck Dacus[1], Robert J. De Rosa[8], Fernando Garcia Toro[1], Clare Leonard[1], Bruce Macintosh[9], Katie M. Morzinski[2], Wyatt Mullen[9], Joseph Palmo[1], Raymond Nzaba Saitoti[1], Elijah Spiro[1], Helena Treiber[1], Kevin Wagner[2,12], Jason Wang (王劲飞)[10,13], David Wang[1], Alex Watson[1], and Alycia J. Weinberger[11]

[1] Department of Physics & Astronomy, Amherst College, 25 East Drive, Amherst, MA 01002, USA; kfollette@amherst.edu
[2] Steward Observatory, University of Arizona, Tucson, 933 N Cherry Avenue, Tucson, AZ 85721, USA
[3] Department of Astronomy, Smith College, Northampton, MA 01063 USA
[4] Department of Physics & Astronomy, Johns Hopkins University, 3400 N. Charles Street, Baltimore, MD 21218, USA
[5] Space Telescope Science Institute, 3700 San Martin Drive, Baltimore, MD 21218, USA
[6] Center for Astrophysics, Harvard & Smithsonian, 60 Garden Street, Cambridge, MA 02138, USA
[7] Department of Astronomy, University of Massachusetts, Amherst, MA 01003, USA
[8] European Southern Observatory, Alonso de Córdova 3107, Vitacura, Santiago, Chile
[9] Kavli Institute for Particle Astrophysics and Cosmology, Department of Physics, Stanford University, Stanford, CA 94305, USA
[10] Department of Astronomy, California Institute of Technology, Pasadena, CA 91125, USA
[11] Earth & Planets Laboratory, Carnegie Institution for Science, 5241 Broad Branch Road NW, Washington, DC 20015, USA
Received 2022 July 26; revised 2023 January 23; accepted 2023 January 30; published 2023 May 5

Abstract

Accreting protoplanets are windows into planet formation processes, and high-contrast differential imaging is an effective way to identify them. We report results from the Giant Accreting Protoplanet Survey (GAPlanetS), which collected Hα differential imagery of 14 transitional disk host stars with the Magellan Adaptive Optics System. To address the twin challenges of morphological complexity and point-spread function instability, GAPlanetS required novel approaches for frame selection and optimization of the Karhounen–Loéve Image Processing algorithm `pyKLIP`. We detect one new candidate, CS Cha "c," at a separation of 68 mas and a modest Δmag of 2.3. We recover the HD 142527 B and HD 100453 B accreting stellar companions in several epochs, and the protoplanet PDS 70 c in 2017 imagery, extending its astrometric record by nine months. Though we cannot rule out scattered light structure, we also recover LkCa 15 "b," at Hα; its presence inside the disk cavity, absence in Continuum imagery, and consistency with a forward-modeled point source suggest that it remains a viable protoplanet candidate. Through targeted optimization, we tentatively recover PDS 70 c at two additional epochs and PDS 70 b in one epoch. Despite numerous previously reported companion candidates around GAplanetS targets, we recover no additional point sources. Our moderate Hα contrasts do not preclude most protoplanets, and we report limiting Hα contrasts at unrecovered candidate locations. We find an overall detection rate of $\sim 36^{+26}_{-22}$%, considerably higher than most direct imaging surveys, speaking to both GAPlanetS's highly targeted nature and the promise of Hα differential imaging for protoplanet identification.

Unified Astronomy Thesaurus concepts: Direct imaging (387); Exoplanet astronomy (486); Exoplanet detection methods (489); Exoplanet formation (492); Exoplanets (498); Planet formation (1241); Protoplanetary disks (1300); Stellar accretion (1578); High contrast techniques (2369); Adaptive optics (2281); Astronomy image processing (2306)

Supporting material: figure sets, interactive figure

1. Introduction

To date, the field of exoplanet direct imaging has largely and necessarily been focused on detection of several tens of megayear old "adolescent" planets that are warm and self-luminous. Most detected planets have been massive ($M > 1 M_J$), nearby ($d < 50$ pc), and members of young moving groups (ages generally >10 Myr). In this section, we present the motivation for protoplanet direct imaging, outline progress in this emerging subfield, and describe synergies with other techniques.

1.1. Protoplanet Imaging Challenges

Detection of planets in very young (< 10 Myr) systems has the potential to inform where, when, and how planet formation occurs, but is notoriously difficult for several reasons. First, the nearest star-forming regions are more distant ($d \geqslant 140$ pc) than the bulk of the directly imaged planet population. This increased distance means that host stars have higher apparent magnitudes, making natural guide star adaptive optics imaging (which relies on photons from the star for wavefront sensing) difficult, while laser guide star systems cannot yet achieve the requisite contrasts at small angular separation. Distant targets

[12] NASA Hubble Fellowship Program – Sagan Fellow.
[13] 51 Pegasi b Fellow.

also require higher angular resolution to image their environs on the scale of planetary systems (~10 au, <0.″1). Visible-light adaptive optics imaging mitigates this difficulty somewhat, providing a resolution ($\sim\lambda/D$) advantage of approximately a factor of 2 over diffraction-limited near-infrared (NIR) imaging.

In the field of protoplanet direct imaging, the most widely studied systems host so-called "transitional" disks, with central cavities cleared of a majority of dusty disk material. Large (tens of astronomical unit) heavily dust-depleted transitional disk cavities are likely maintained by the presence of multiple orbiting planets in mean motion resonance whose Hill spheres overlap (Dodson-Robinson & Salyk 2011; Close 2020), or by more disruptive eccentric or noncoplanar orbits of single companions (e.g., Price et al. 2018). The outer environs of transitional disks are, however, morphologically complex. This presents a second obstacle to the direct detection of very young exoplanets embedded within them, namely the difficulty of unambiguously separating disk and planet signal.

The field of high-contrast imaging (HCI) relies on sophisticated processing algorithms for point-spread function (PSF) subtraction (e.g., locally-optimized combination of images and Karhounen–Loéve Image Processing (KLIP); Lafreniere et al. 2007; Soummer et al. 2012). These algorithms are powerful tools for isolating faint disk and planet signals, but have been demonstrated to affect the apparent morphology of disk features to varying degrees and to yield apparent point sources when structures are in fact continuous (e.g., Follette et al. 2017; Ligi et al. 2018). For this reason, most reported detections of protoplanet candidates in transitional disks have been heavily debated. These include the planet candidates LkCa 15 "b", "c", and "d" (Kraus & Ireland 2012; Sallum et al. 2015; Thalmann et al. 2015; Currie et al. 2019), HD 169142 "b" (Biller et al. 2014; Reggiani et al. 2014; Ligi et al. 2018; Gratton et al. 2019), T Cha "b" (Huélamo et al. 2011), MWC 758 "b" (Reggiani et al. 2018), HD 100546 "b" and "c" (Quanz et al. 2013; Currie et al. 2015; Quanz et al. 2015; Follette et al. 2017; Rameau et al. 2017), and AB Aur "b" (Currie et al. 2022; Zhou et al. 2022).

The only protoplanets considered unambiguous at present are PDS 70 b and PDS 70 c. PDS 70 b's nature as a bona fide accreting protoplanet is supported by multiwavelength characterization, namely its detection in thermal emission at a variety of infrared wavelengths (Keppler et al. 2018; Müller et al. 2018; Wang et al. 2021b), at Hα (Wagner et al. 2018a; Haffert et al. 2019), and in ultraviolet accretion continuum emission (Zhou et al. 2021). Likewise, PDS 70 c has been detected in IR thermal emission (Mesa et al. 2019; Wang et al. 2021b), at Hα (Haffert et al. 2019), and in submillimeter continuum emission (evidence of the presence of a circumplanetary disk; Isella et al. 2019; Benisty et al. 2021).

Prior to the discovery of PDS 70 b and c, the only confirmed object imaged inside of a transitional disk gap was the stellar-mass companion HD 142527 B (Biller et al. 2014; Close et al. 2014). Though it is not a planetary-mass object ($M_B = 0.11 \pm 0.06\,M_\odot$; Claudi et al. 2019), its tight separation (~15 au; Balmer et al. 2022), ongoing accretion ($\sim 10^{-9} M_\odot\,\mathrm{yr}^{-1}$; Balmer et al. 2022), and extreme mas ratio of ~0.05 relative to the primary ($M_A = 2.0 \pm 0.3\,M_\odot$; Mendigutía et al. 2015) make it an important benchmark system and test case for detections of accreting companions embedded in transitional disks.

Evidence of ongoing accretion onto more widely separated imaged companions has also been found. These include the substellar companions DH Tau b, GSC 6214-210 b, GQ Lup b, Delorme 1 (AB) b, and SR 12 c (e.g., Zhou et al. 2014; Santamaría-Miranda et al. 2018; Betti et al. 2022). Although their ages and separations do not make them direct analogs of protoplanets in transitional disk gaps, these more easily recovered and characterized substellar companions provide a fruitful testing ground for planetary accretion models.

In addition to the high required resolution and morphological complexity of transitional disk systems, a third obstacle to direct protoplanet detection is achieving the requisite contrasts at extremely tight separations. For example, in NIR thermal emission, contrasts of $\sim 10^{-6}$–10^{-4} are required at ~0.″1–0.″25 in order to image protoplanets inside of disk gaps, and this region lies beneath the coronagraphic masks of most extreme adaptive optics imagers.

1.2. Hα Differential Imaging

One way to mitigate the obstacles outlined in the previous section is to leverage (a) the higher resolutions of visible light adaptive optics imaging, and (b) the lower contrasts required to detect protoplanets at wavelengths where accretion emission is present.

The resolution of a 6.5 m telescope is 21 mas at Hα (656.3 nm, the brightest accretion emission line), small enough to resolve companions inside of the 0.″1–0.″25 cavities of most transitional disks. In young objects, emission at Hα is often associated with ongoing accretion, and is predicted to elevate the flux of planetary-mass objects into a modest contrast range of $\sim 10^{-3}$–10^{-2} for super-Jovian planets (Mordasini et al. 2017). Accretion is expected even for protoplanets within cleared transitional disk cavities because the primary stars in these systems are themselves still actively accreting gas (e.g., Cieza et al. 2012; Salyk et al. 2013). "Off" Hα, planet contrasts should drop below the detectability threshold, making differential imaging a powerful tool to separate direct planet light from signals that are equivalently bright in the two channels or whose brightnesses mimic the stellar Hα-to-continuum ratio, such as disk scattered light and PSF subtraction artifacts.

To date, five accreting object candidates have been identified inside of transitional disk gaps. The assertion of accretion in each case is based, at least in part, on the presence of Hα excess emission. These are: the stellar-mass companion HD 142527 B (Close et al. 2014), the protoplanets PDS 70 b and c (Wagner et al. 2018a; Haffert et al. 2019; Zhou et al. 2021), and the protoplanet candidates LkCa 15 b (Sallum et al. 2015) and AB Aur b (Currie et al. 2022). Three of these objects (HD 142527 B, PDS 70 b, and LkCa 15 b) were first detected at Hα as part of the Giant Accreting Protoplanet Survey (GAPlanetS).

1.3. Multiwavelength Disk Imaging

High-resolution submillimeter imagery of transitional disks obtained with the Atacama Large Millimeter/submillimeter Array (ALMA) strongly complements these initial accreting object detections (e.g., Pérez et al. 2014; van der Marel et al. 2016), as does NIR scattered light imagery obtained by extreme adaptive optics imagers such as the Gemini Planet Imager (Macintosh et al. 2014), Spectro-Polarimetric High-contrast Exoplanet REsearch instrument (SPHERE; Beuzit et al. 2008),

Subaru Coronagraphic Extreme Adaptive Optics System (SCExAO; Jovanovic et al. 2015), and MagAO-X (Males et al. 2018).

The proliferation of multiwavelength imagery of transitional disks over the past decade revealed the initially puzzling fact that transitional disk cavities often appear at substantially different radii in the NIR and submillimeter (e.g., Dong et al. 2012; Follette et al. 2013; Villenave et al. 2019). The prevailing theories for this now well-established discrepancy invoke so-called "dust filtration" processes, whereby the location and degree of clearing of variously sized grains is controlled by the location and mass of planets embedded in the disk (e.g., Zhu et al. 2012; Fung et al. 2014). More specifically, because large grains settle toward the midplane, protoplanets may effectively clear a submillimeter cavity while allowing higher scale-height optical/NIR-scattering small grains to filter through the cavity at the disk surface layer. Although differential clearing of large versus small grains is suggestive of the presence of planets inside disk gaps and cavities, direct inference of planet masses based on gap radii is difficult. Since scale height varies as a function of radius in the disk, so too does the "gap clearing" mass threshold.

Knowledge of disk morphology is important for protoplanet searches for several reasons. Practically speaking, cavities that are not substantially cleared of small optical/NIR-scattering grains will be poor candidates for protoplanet detections, as Hα light emitted by planets at the disk midplane is likely to be extincted by that overlying material. Furthermore, although in principle features such as differential clearing and disk asymmetries (spiral arms, dust traps, annular rings, velocity kinks, etc.) should predict the location of accreting protoplanets, detection of structure-inciting planets has not been widely successful. This indicates either that planet–disk interaction models still need to be refined or that we are not yet achieving the requisite contrasts, or both.

1.4. Outline of This Work

The Magellan Adaptive Optics System (MagAO) Giant Accreting Protoplanet Survey (GAPlanetS), whose results are reported in the remainder of this paper, surveyed 14 transitional disk host stars for evidence of accreting protoplanets. The search required development of a general framework for robust, uniform HCI processing in complex, embedded planetary systems. This paper aims to present both the results of the survey and the details of the data processing framework.

The GAPlanetS survey sample is described in Section 2. Detailed summaries of known disk morphologies and previously reported evidence for the presence of protoplanets in each system appear in Appendix A . Image preprocessing procedures, which are somewhat more complex than for NIR HCI surveys due to the instability of visible light AO PSFs, are detailed in Section 2.3. Post-processing procedures that allow for data-driven optimization of PSF subtraction algorithmic parameters, necessary for analyzing these highly morphologically complex systems, are detailed in Section 3. Strategies adopted to ensure uniform, data-driven comparison among objects in the full survey sample are described in Section 4.

Leveraging the techniques outlined in Sections 2.3–4, GAPlanetS searched for embedded planets responsible for inciting disk structures and clearing the observed central cavities of the 14 targeted transitional disks. Individual object-by-object results are detailed in Section 5 and in Appendix B. In Section 6, we present constraints on the astrometry and accretion rates of the five accreting companions and companion candidates detected in the survey, limits on the contrasts/accretion rates of protoplanet candidates undetected in our survey, and aggregate survey statistics.

2. Observations

2.1. The GAPlanetS Sample

In Table 1, we outline the physical properties of the GAPlanetS transitional disk sample. Because of the importance of varied gap radii to the interpretation of evidence for embedded planets in these systems, we report both the NIR and submillimeter gap radii in Table 1. Reviews of the literature on individual objects in the sample are provided in Appendix A, including details about previous evidence for and characterization of protoplanets.

Of the known transitional disks, relatively few are around sufficiently bright stars for natural guide star adaptive optics imaging. The selection criteria for the initial GAPlanetS sample were: (a) an r' band magnitude brighter than 11, (b) a decl. less than $+30°$ such that the object is visible from Magellan, and (c) a previously resolved NIR gap or cavity at a separation of at least $0\farcs1$ from the central star. After a successful pilot observation of LkCa 15 ($R = 10.7$), the guide star magnitude requirement was relaxed to $R < 11$, and five additional objects were added to the sample (including PDS 70, which was not at the time known to host protoplanets). Only two of these additional objects were successfully observed due to weather and time constraints, for a total of 14 targets in the GAPlanetS sample.

2.2. Data Collection

All data for the GAPlanetS campaign were taken with MagAO (Close et al. 2013; Morzinski et al. 2014, 2016) and the VisAO instrument (VisAO; Males 2013; Males et al. 2014) between 2013 April and 2018 May. The number of observations per object ranges from one to seven, with a median of three. Some objects were attempted multiple times in the same semester, either because conditions were poor during a first attempt or because observers using the MagAO infrared camera Clio2 (Morzinski et al. 2013) were observing GAPlanetS targets and contributed their visible light data to the campaign. Any imaging sequence with fewer than $10°$ of rotation on the sky ($N = 9$), fewer than 10 minutes of total integration time ($N = 1$), or an FWHM of greater than $\sim0\farcs15$ for the registered and median-combined PSF ($N = 7$) was not analyzed. Finally, seven data sets were of sufficiently low or variable quality that we were unable to extract false planets injected into the images at a contrast of 1×10^{-1}, and these were not analyzed further. In total, 23 data sets were discarded, representing 18 hr, or 20% of the total campaign time. This is consistent with typical weather and seeing site statistics for Las Campanas (e.g., Duhalde & Krzeminski 1984), where these observations were conducted classically. Table 2 summarizes the data sets that were retained and analyzed for this paper, which amount to a total of 60 hr of open shutter time. Raw, preprocessed, and post-processed data for all GAPlanetS data sets are available on the Harvard Dataverse: doi:10.7910/DVN/LW9WJJ.

2.3. Image Preprocessing

The VisAO camera cannot take zero second bias exposures, so dark frames were taken interspersed with the science frames to track both bias drifts and dark current contributions. Median

Table 1
GAPlanetS Target Properties

Object	R.A.[1]	Decl.[1]	r' Mag[2,3]	$A_{r'}$[2,4]	SpT	d[1] (pc)	Assn[16]	Member Prob.[16]	Age (Myr)	$\log \dot{M}\ (\frac{M_\odot}{yr})$	mm $r_{gap(s)}$	NIR $r_{gap(s)}$	Gap Refs
HD 142527	239.174469	−42.323241	8.2	0.8	F6[5]	159.3 ± 0.7	UCL	92.10%	16 ± 2[15]	−7.16[23]	0.″26–1.″2	0.″1–1.″0	38,50
PDS 70	212.0421	−41.39804	11.7	0	K7[15]	112.4 ± 0.2	UCL	98.70%	5.4 ± 1[36]	−10.22[37]	0.″11–0.″43	0.″2–0.″4	65,66
LkCa 15	69.82418	22.35086	11.6	0.5	K5[14]	157.2 ± 0.7	TAU	88.20%	1–2[22]	−9.13[35]	<0.″27, 0.″33–0.″41, 0.″45–0.″58	0.″21–0.″42	49,64
HD 169142	276.1241	−29.78054	8.2	0	F1[6]	114.9 ± 0.4	Field	98.90%	6^{+6}_{-3}[20]	−8.68[27]	0.″02-0.″23, 0.″28–0.″48, 0.″51–0.″56, 0.″57–0.″65	0.″004–0.″17, 0.″28–0.″48	38,42,43,55
HD 100546 n	173.3555	−70.19479	6.8	0.2	A0[6]	108.1 ± 0.4	LCC	98.90%	15 ± 3[15]	−6.44[24]	0.″02-0.″19	0.″007-0.″14	39, 51
SAO 206462	228.9518	−37.15455	8.6	0.1	F8[7]	135.0 ± 0.4	UCL	99.50%	16 ± 2[15]	−7.7[28]	<0.″38, 0.″48–0.″55	0.″18	44,56
TW Hya	165.4659	−34.70479	10.5	0.5	K7[12]	60.1 ± 0.1	TWA	99.90%	10 ± 3[21]	−8.58[33]	0.″0083–0.″033, 0.″2–0.″22, 0.″35–0.″38, 0.″45–0.″48, 0.″62–0.″65, 0.″7–0.″73	0.″083–0.″17, 0.″27–0.″42, 1.″16–1.″5	48,62
HD 100453	173.273	−54.32462	7.8	0.2	A9[5]	103.8 ± 0.2	LCC	99.30%	<−8.85[26]	0.″09–0.″22, 0.″40–0.″48	0.″09–0.″14	41,54
CS Cha	165.6032	−77.55989	11.1	1.0	K2[13]	168.8 ± 1.9	Cha I[18]	n/a	2 ± 2[18]	−8.3[34]	<0.″21	<0.″0925	38,63
HD 141569	237.4905	−3.921291	7.2	0.2	A2[6]	111.6 ± 0.4	Field	99.90%	5 ± 3[19]	−8.13[25]	0.″9 ∼ 1.″9	0.″25–0.″4, 0.″43–0.″52, 0.″60–0.″69, 1–2″	40,52,53
PDS 66	200.5309	−69.63682	10.0	0.7	K1[10]	97.9 ± 0.1	LCC	97.50%	15 ± 3[15]	−8.3[31]	···	0.″46–0.″81	60
UX Tau A	67.5167	18.23033	11.3	0.5	K2[11]	142.2 ± 0.7	TAU	98.10%	1–2[22]	−8[32]	0.″18	0.″16	47,61
V1247Ori	84.52188	−1.25603	9.9	0.3	F0[8]	401.3 ± 3.2	ϵ Ori[17]	n/a	5–10[17]	−8[29]	0.″04–0.″15	< 0.″07–0.″11	45,57,58
V4046 Sgr	273.5437	−32.79316	10.0	0	K5-7[9]	71.5 ± 0.1	BPMG	98.40%	24 ± 3[21]	−9.3[30]	0.″08–0.″3	0.″10–0.″19	46,59

Note. Relevant stellar properties for the GAPlanetS sample of young, transitional disk systems. The targets are ordered according to order of appearance in Section 5. References: [1] Gaia Collaboration et al. (2022a), [2] Gaia Collaboration et al. (2022a) DR3 photometry converted to the SDSS r' magnitude per [3](Alam et al. 2015), [4] (Pecaut & Mamajek 2013),[5] Houk & Smith-Moore (1994), [6] Gray et al. (2017), [7] Coulson & Walther (1995), [8] Vieira et al. (2003), [9] Nefs et al. (2012), [10] da Silva et al. (2006), [11] Kraus & Hillenbrand (2009), [12] Wichmann et al. (1998), [13] Appenzeller (1977), [14] Herbig & Goodrich (1986), [15] Pecaut & Mamajek (2016), [16] Gagné et al. (2018), [17] Caballero & Solano (2008), [18] Luhman (2004), [19] Weinberger et al. (2000), [20] Grady et al. (2007), [21] Bell et al. (2015), [22] Kenyon & Hartmann (2002), [23] Garcia Lopez et al. (2006), [24] Mendigutía et al. (2015), [25] Salyk et al. (2013), [26] Collins et al. (2009), [27]Wagner et al. (2015b), [28] Sitko et al. (2012), [29] Willson et al. (2019), [30] Curran et al. (2011), [31] Pascucci et al. (2007), [32] Andrews et al. (2011a), [33] Robinson & Espaillat (2019), [34] Manara et al. (2014), [35] Alencar et al. (2018), [36] Müller et al. (2018), [37] Thanathibodee et al. (2020) [38]Francis & van der Marel (2020), [39]Pineda et al. (2019), [40]Miley et al. (2018), [41]van der Plas et al. (2019), [42]Fedele et al. (2017), [43]Pérez et al. (2019), [44]Cazzoletti et al. (2018), [45]Kraus et al. (2017), [46]Kastner et al. (2018), [47]Pinilla et al. (2014), [48]Andrews et al. (2016), [49]Facchini et al. (2020), [50]Avenhaus et al. (2014), [51]Follette et al. (2017), [52]Konishi et al. (2016), [53]Perrot et al. (2016), [54]Benisty et al. (2016), [55]Monnier et al. (2017), [56]Stolker et al. (2016), [57]Ohta et al. (2016), [58]Willson et al. (2019), [59]Rapson et al. (2015), [60]Wolff et al. (2016), [61]Tanii et al. (2012), [62]van Boekel et al. (2017), [63]Ginski et al. (2018), [64]Oh et al. (2016), [65]Long et al. (2018), [66]Keppler et al. (2018).

Table 2
Descriptive Statistics for GAPlanetS Campaign Data

Object Name	Date	n_{ims}	t_{exp} (s)	t_{tot} (minute)	Rot (°)	FWHM (pix)	r_{sat} (pix)	Avg. Seeing (″)	Scale Factor
HD 142527	4/11/13	1961	2.27	74.2	65.3	4.56^{G}	6	0.56	0.88 ± 0.04
HD 142527	4/8/14	68	45	51.0	100.7	4	N/A	⋯	1.14 ± 0.02
HD 142527	4/8/14	1758	2.27	66.5	101.7	5.58^{G}	10	⋯	1.13 ± 0.03
HD 169142	4/8/14	2796	2.27	105.8	180.1	5.5	N/A	0.72	0.99 ± 0.03
TW Hya	4/8/14	1958	2.27	74.1	82.5	6.36	N/A	⋯	8.79 ± 0.11
HD 169142	4/9/14	178	15	44.5	171.6	5.01	N/A	⋯	0.98 ± 0.05
HD 141569	4/9/14	2402	2.27	90.9	55.7	17.2^{G}	4	0.70	0.94 ± 0.06
HD 141569	4/10/14	1364	2.27	51.6	36.6	6.85^{G}	4	⋯	0.96 ± 0.10
HD 141569	4/11/14	2340	2.27	88.5	58.9	8.57	N/A	⋯	0.95 ± 0.05
HD 100546	4/12/14	4939	2.27	186.9	71.6	3.92^{G}	4	⋯	1.43 ± 0.06
SAO 206462	4/12/14	3993	2.27	151.1	143.7	5.16^{G}	3	⋯	1.22 ± 0.10
V4046 Sgr	4/12/14	1414	5	117.8	156.1	7.86	N/A	⋯	1.79 ± 0.40
UX Tau A	11/15/14	52	45	39.0	13.8	9.55	N/A	⋯	1.42 ± 0.04
V1247 Ori	11/15/14	893	7/10	113.0	46.5	5.39	N/A	⋯	1.13 ± 0.02
LkCa 15	11/16/14	308	30	154.0	48.6	8.67	N/A	⋯	1.81 ± 0.03
HD 141569	5/28/15	723	5/10	84.1	54.2	5.79^{G}	5	⋯	0.94 ± 0.02
HD 142527	5/15/15	2387	2.27	90.3	117.4	5.5	N/A	⋯	1.13 ± 0.10
CS Cha	5/15/15	143	30	71.5	31.4	9.17	N/A	0.59	2.26 ± 0.05
HD 142527	5/16/15	1143	2.27	43.2	34.8	5.01	N/A	0.55	1.14 ± 0.12
V4046 Sgr	5/17/15	720	5	60.0	146.5	6.44	N/A	0.66	1.80 ± 0.10
HD 142527	5/18/15	159	30	79.5	76.8	5.24^{G}	2	0.80	1.12 ± 0.06
HD 169142	5/18/15	1731	2.27	65.5	180.6	8.17^{G}	6	⋯	1.06 ± 0.09
SAO 206462	5/26/15	408	10	68.0	15.9	6.21	N/A	0.70	1.22 ± 0.10
HD 141569	5/29/15	404	10	67.3	56.1	12.1	N/A	0.80	0.92 ± 0.03
HD 100546	5/30/15	2459	2.27	93.0	43.7	5.31^{G}	6	⋯	1.59 ± 0.20
V1247 Ori	12/11/15	878	7	102.4	21.7	6.93	N/A	0.69	1.12 ± 0.04
LkCa 15	11/18/16	252	30	126.0	36.03	12.2	N/A	0.47	1.58 ± 0.10
PDS 66	2/7/17	243^{+}	30	121.5	42.7	6.74	N/A	0.61	1.91 ± 0.02
TW Hya	2/7/17	452^{+}	30	226.0	139.6	7.98	N/A	0.69	7.17 ± 0.20
PDS 70	2/8/17	188^{+}	45	141.0	92.9	8.36	N/A	0.47	1.32 ± 0.02
HD 142527	2/10/17	242	12	48.4	16.1	4.49^{G}	8	0.66	1.22 ± 0.10
HD 100453	2/17/17	2947	3/5	160.0	61.4	4.26^{G}	4	0.60	1.10 ± 0.03
HD 169142	8/30/17	1658^{+}	2.27	62.7	171.3	5.83^{G}	3	0.70	1.13 ± 0.03
HD 142527	4/27/18	580	5	48.3	49.2	4.37	3	⋯	1.28 ± 0.06
HD 100453	5/2/18	563^{+}	15	140.8	83.3	4.34	N/A	0.64	1.26 ± 0.03
HD 100453	5/2/18	356^{+}	2.27	13.5	86.3	4.90^{G}	3	0.64	1.05 ± 0.02
PDS 70	5/2/18	209^{+}	30	104.5	90.9	7.08	N/A	0.52	1.29 ± 0.02
PDS 70	5/3/18	284^{+}	30	142.0	111.7	6.82	N/A	0.50	1.36 ± 0.02
HD 100453	5/3/18	2831^{+}	2.27	107.1	66.18	6.17	N/A	0.45	1.04 ± 0.10

Note. These statistics represent the data sets before the data quality cut step described in Section 3.1. Statistics for the final post-processings of each data set are given in Table 3. The + superscript indicates a data set observed in Simultaneous Differential Imaging, SDI^{+}, mode, which utilizes a spinning half-wave plate to mitigate polarization effects. The G superscript indicates data sets for which the stable instrumental ghost was used to estimate the FWHM of the saturated central star. Seeing statistics were measured by either the site's DIMM or by the neighboring Baade telescope, and were averaged where both measures were available. In some cases, no seeing data were available from the Magellan site monitors. Scale factors reported are the median value of the ratio of the flux of the primary (unsaturated data) or ghost (saturated data) at Hα relative to the contemporaneous continuum in individual images, as determined by aperture photometry and described in the text in Section 2.4. Uncertainties on scale factors represent the standard deviation of the scale measurements for individual images. Raw, preprocessed, and post-processed data is available for all GAPlanetS data sets on the Harvard Dataverse: doi:10.7910/DVN/LW9WJJ.

levels in each CCD channel for all dark frames taken in a given sequence were inspected for bias drifts, and the level was found to be static to within 3 analog-to-digital units ("counts"). We find that fluxes in dark frames are constant to <1%, so we utilize a median combination of all dark frames for a given data set in our calibrations, subtracting the median dark from each raw image frame.

r' band (which spans Hα) twilight sky flats were used to calibrate most data sets. Due to scheduling constraints at twilight, flat frames were not collected on every night of GAPlanetS observations. In cases where more than one *r*' band flat data set was available in a given semester, we selected the flat that was closest in time to the observations, so long as it was of high quality. During the 2017A semester, no *r*' band flats were collected, so we utilized a *z*-band flat for calibration. During the 2013A semester (containing a single GAPlanetS data set), no appropriate flat data sets were available, so we applied a 2014A flat to these data. The median number of days between flat and science exposures for all GAPlanetS data sets was five.

We find that the VisAO detector's sensitivity is flat to better than 1% in both space (across the detector) and time (from semester to semester), so the primary purpose of flat field correction is removal of near-focus dust spots on the CCD window, which attenuate light by a few to a few tens of

percents. The influence of these dust spots on final images is mitigated both by dividing by the flat image for a given semester and by dithering the star on the detector during observations. For one data set (UX Tau A), the observations were aborted before dithers were completed.

In developing the GAPlanetS pipeline, we experimented with masking dust spots and with interpolating over them using various methodologies; however, standard unmasked flat fields resulted in the highest-quality reductions of the HD 142527 B companion, both qualitatively (final image appearance) and quantitatively (signal-to-noise ratio; S/N). The majority of VisAO dust spots are static from semester to semester, and in all cases individual images were inspected for poorly corrected dust spots, and such images were discarded before final PSF subtraction.

GAPlanetS data were taken in the VisAO camera's Simultaneous Differential Imaging (SDI) mode. The MagAO wave front sensor, like the VisAO camera, operates in visible light. For all GAPlanetS observations, a 50/50 beamsplitter was used to send half of the incoming light to the wave front sensor and half to the VisAO science camera. In SDI mode, a Wollaston prism is used to further split the VisAO science beam into two equal components. One Wollaston beam is passed through a narrowband filter centered on the Hα emission line ($\lambda_{\rm central} = 656$ nm, $\Delta\lambda = 6$ nm) and the other beam is passed through a narrowband continuum filter centered nearby at a wavelength of 642 nm ($\Delta\lambda = 6$ nm). The dark-subtracted, flat-fielded 1024×1024 pixel images are therefore split into two 1024×512 "channels," representing the images of the star at Hα and the continuum. The proximity of these filters in wavelength and the minimal noncommon path makes the PSFs of the two channels extremely similar, with a few caveats, outlined in Section 2.4.

Following the splitting of the wavelength channels, all GAPlanetS images are then registered using Fourier cross-correlation against a single representative science image selected from within the sequence. The reference image itself is centered via cross-correlation with a Gaussian of equivalent FWHM. This simple registration method was found to yield the highest average S/N for the known companion HD 142527 B across many data sets.

In the case of saturated images, both registration and photometry are computed relative to an optical ghost that is present at the same location in all images. The ghost has been found to be astrometrically stable to within 1 pixel and to have a stable brightness ratio relative to the primary star of 179.68 ± 4.59 in the Hα filter and 196.31 ± 3.56 in the continuum filter. The ghost also has an FWHM 7% larger than the central PSF, indicating that it is slightly out of focus and is likely produced by a reflection off of the backside of the 6 mm thick MagAO 50/50 beamsplitter. A full description of MagAO astrometric and ghost calibration is provided in Balmer et al. (2022).

All GAPlanetS images contain a bright ring of emission at the boundary of the AO system's "control radius," or "dark hole." The location of the control radius is defined by the boundary between spatial frequencies that are sensed versus unsensed by the wave front sensor. When imaging guide stars with r′ band magnitudes fainter than ∼8, the pyramid WFS camera is binned to 2×2 pixels in order to obtain sufficient signal for wave front correction. This effectively halves the control radius in such images. The MagAO control radius is ∼0.″25 (30 pixels) in bin 1 and ∼0.″12 in bin 2. Only five of 14 GAPlanetS targets (HD 142527, HD 100546, HD 141569, HD 100453, and HD 169142) have r' band magnitudes brighter than 8; therefore, an $r = 30$ pixel control radius. The remaining nine GAPlanetS systems were imaged with a control radius of 15 pixels. This is relevant in that the dark hole is the region in which the adaptive optics system most effectively concentrates starlight into the central PSF, and we concentrate our search and optimization algorithms in this region of the images, which happens to also correspond approximately to the size of the cleared central cavities of most GAPlanetS systems.

The 1024×512 pixel channel images are cropped after registration to reduce processing time. The size of the cropped region was chosen to be 451×451 pixel (3.″5) square, slightly smaller than the 521 pixel channel width so that images would be equivalently sampled across dithers.

The final step before PSF subtraction is a by-eye inspection of the registered image frames. Images where the adaptive optics control loop is fully open are rejected in the initial phase of the pipeline. An additional by-eye rejection step allows us to discard images where the loop is formally closed, but in the process of breaking or re-closing. At this stage, we also reject several types of artifacts, namely any images with: (a) cosmic rays within 50 pixels of the central star, (b) severe instrumental artifacts such as mid-image dithers, and (c) incompletely removed dust spot artifacts within the AO control radius ($r \sim 30$ pixels). A median of 97.8% of Hα images are retained following this rejection step, with a standard deviation of 4.6%. For continuum images, a median of 95.3% of images are retained with a standard deviation of 7.4%; this larger proportion of rejected images is due to an increase in the number of dust spots on the bottom half of the detector. Data set statistics reported in Table 2 record the total number of closed-loop images and total integration times prior to this rejection step. The statistics for the proportion of images used in final analyses are reported in Table 3. They reflect an additional frame selection step described in detail in Section 3.1.

A coarse grid search of `PyKLIP` parameters defining (a) the geometry of separately modeled annular zones in the images, (b) the size of the PSF reference library, and (c) the complexity of the PSF model is then conducted for this subset of images. The details of this methodology, including motivation for the choice of parameters to optimize, is provided in Section 3.2, and the optimized values for `pyKLIP` parameters are provided in Table 3.

2.4. SDI Processing and Mitigation of Possible Sources of Line versus Continuum Mismatch

Since a Wollaston prism operates by splitting light according to polarization state, and scattered light from circumstellar disks (which is present in all GAPlanetS targets) is polarized, there is a reasonable expectation that individual pairs of line and continuum images will contain some differences in scattered light contributions. This is mitigated in several ways.

First, data are highpass filtered to remove low spatial frequency structures (including extended disk emission and the AO control radius) before PSF subtraction. Second, the majority of the cavities where the search for accreting protoplanets was concentrated are sufficiently cleared of small grain optical scatterers that this contribution is minimal. Nevertheless, we mark the location of known scattered light

Table 3
Summary of Optimization Results for Each GAPlanetS Data Set

General Data Set Parameters						Data Quality Cut Parameters				KLIP Optimization Parameters			
Object	Date	$N_{\rm total}$	Bin	$r_{\rm sat}$	IWA	$C_{\rm fakes}$	Cut	FWHM	Cut Classification	$N_{\rm false}$	Annuli	Movement	KL Modes
CS Cha	5/15/15	143	2	⋯	7	0.05	30	7	down and up inside 0.″2	2	6	2	3
HD 100453	2/17/17	2947	1	3	4	0.01	10	4	clustered, increasing	5	5	3	10
HD 100453	5/2/18	356	1	2	3	0.01	40	3	clustered, increasing	8	8	1	20
HD 100453	5/2/18	563	1	4	4	0.01	30	3	clustered, increasing	7	13	1	20
HD 100453	5/3/18	2831	1	4	4	0.01	70	3	turnover at 0.″07	7	19	1	20
HD 100546	4/12/14	4939	1	8	8	0.01	10	5	clustered, increasing	3	13	1	10
HD 100546	5/30/15	2459	1	2	4	0.05	50	4	turnover at 0.″12	5	25	2	5
HD 141569	4/9/14	2402	1	5	5	0.01	70	5	turnover at 0.″15	4	1	1	5
HD 141569	4/10/14	1364	1	2	6	0.01	50	6	turnover at 0.″15	3	2	4	1
HD 141569	4/11/14	2340	1	4	4	0.01	10	4	clustered, increasing	5	4	5	20
HD 141569	5/28/15	723	1	⋯	7	0.05	70	7	decreasing	2	2	4	2
HD 141569	5/29/15	404	1	9	9	0.01	0	4	increasing	4	1	5	5
HD 142527	4/11/13	1961	1	⋯	3	0.01	10	3	clustered, increasing	8	14	1	20
HD 142527	4/8/14	1758	1	⋯	4	0.01	0	4	clustered, increasing	5	25	1	100
HD 142527	4/8/14	68	1	11	11	0.01	0	5	increasing	2	21	1	10
HD 142527	5/15/15	2387	1	2	4	0.01	50	4	clustered, increasing	5	2	2	20
HD 142527	5/16/15	1143	1	2	6	0.05	80	4	turnover at 0.″3	5	20	1	20
HD 142527	5/18/15	159	1	6	6	0.01	0	4	clustered, increasing	4	2	7	5
HD 142527	2/10/17	242	1	2	3	0.05	0	4	increasing	5	25	1	5
HD 142527	4/27/18	580	1	3	3	0.05	0	3	clustered, increasing	8	22	1	10
HD 169142	4/8/14	2796	1	⋯	4	0.01	80	4	turnover at0.″3	5	1	1	20
HD 169142	4/9/14	178	1	6	6	0.01	50	5	clustered, increasing	3	20	1	4
HD 169142	5/18/15	1731	1	3	5	0.01	20	5	clustered, increasing	4	6	2	20
HD 169142	8/30/17	1658	1	2	4	0.05	70	4	turnover at CR	5	6	2	20
LkCa 15	11/16/14	308	2	⋯	6	0.05	5	7	clustered, increasing	2	4	6	20
LkCa 15	11/18/16	252	2	⋯	7	0.05	10	11	mostly increasing	1	10	1	20
PDS 66	2/7/17	243	2	⋯	5	0.01	40	5	clustered, increasing	2	2	1	1
PDS 70	2/8/17	188	2	⋯	7	0.05	40	7	down and up in inner 0.″15	2	1	1	1
PDS 70	5/2/18	209	2	⋯	6	0.05	5	6	clustered, increasing	2	4	1	4
PDS 70	5/3/18	284	2	⋯	6	0.05	30	6	down and up in inner 0.″1	2	3	7	50
SAO 206462	4/12/14	3993	2	3	4	0.01	30	4	down and up	5	1	1	3
SAO 206462	5/26/15	408	2	⋯	4	0.05	30	4	clustered, increasing	3	1	2	2
TW Hya	4/8/14	1958	2	⋯	5	0.01	50	5	turnover at 0.″15	2	5	2	1
TW Hya	2/7/17	452	2	2	6	0.01	0	6	increasing	2	6	6	50
UX Tau A	11/15/14	52	2	⋯	8	0.05	8	30	clustered, increasing	2	6	2	50
V1247 Ori	11/15/14	893	2	⋯	4	0.01	50	4	turnover at CR	3	2	9	10
V1247 Ori	12/11/15	878	2	⋯	5	0.01	60	5	turnover at CR	2	2	6	50
V4046 Sgr	4/12/14	1414	2	2	5	0.01	50	5	turnover at 0.″15	2	21	2	20
V4046 Sgr	5/17/15	720	2	⋯	4	0.01	50	4	down and up	3	13	1	50

Note. The leftmost block of columns give general data set parameters, where N_{total} is the total number of images in the data set prior to implementing the data quality cut and "Bin" is the binning of the wave front sensor, which determines the location of the control radius (30 pixels for bin 1, 15 for bin 2). The central block of columns give the parameters for the data quality cuts, where $C_{\rm fakes}$ is the contrast of injected fake planets used to compute contrast curves. The rightmost block of columns are the derived optimal values from `pyKLIP-PE`, where $N_{\rm false}$ is the number of injected false planets between the inner working angle (IWA) and control radius used to compute the optimal parameters.

structures in our final images when there is reason to be concerned about the fidelity of observed signals. Finally, on-sky rotation tends to reduce residual polarization structure across full sequences.

We also note that most GAPlanetS data taken after the 2017A semester are free of differential polarization effects because of the addition of a spinning half-wave plate to the instrument. This half-wave plate spins at 2 Hz, modulating the polarization state of the two Wollaston channels at 8 Hz throughout the image sequence and attenuating polarization noise by a factor of 40 for a 5 s image (Close et al. 2018). These "GAPlanetS^{+}" data sets are indicated in Table 2 with a + symbol.

A second concern regarding comparison of line and continuum channels stems from the fact that the central stars of many of the GAPlanetS targets are themselves actively accreting, and are thus measurably brighter in Hα. Indeed, this is the primary reason to expect that protoplanets within their disk gaps will also be accreting. In such cases, high spatial frequency scattered light disk features that survive the highpass filtering algorithm that is applied before PSF subtraction should be brighter in Hα than in the continuum and may be mistaken

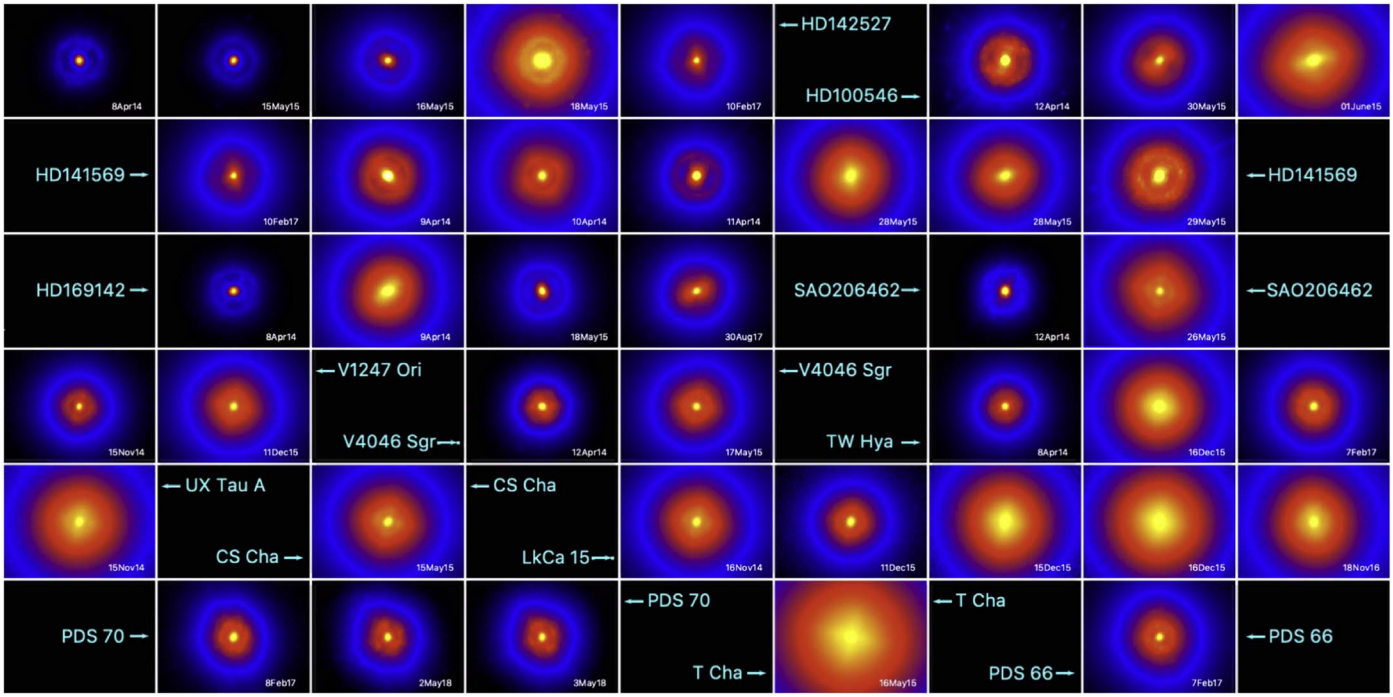

Figure 1. Median combinations of the images in each GAPlanetS image sequence, normalized to 1 by dividing by the peak pixel and arranged from brightest to faintest *r*' band magnitude. The extreme variability in the PSF between objects and among images of the same object acquired on different nights is apparent in the variable size of the PSFs. The VisAO PSF is highly dependent on weather conditions.

for accreting protoplanets. We mitigate this effect by quantifying and compensating for the brightness differential at the two wavelengths directly.

We measure the Hα/continuum brightness ratio of the star for each image in the sequence using aperture photometry of the star (or the ghost in the case of saturated images). We report the median and standard deviation of these line-to-continuum scale factors for each data set in the rightmost column of Table 2. We then use these computed scale factors to complete "conservative" SDI reductions for all data sets. This is done by multiplying the KLIP-ADI reduced continuum image by the scale factor before subtraction from the Hα image to create an SDI image. This compensates for the difference in the brightness of the primary star at the two wavelengths and should remove both stellar residuals and scattered light structures, including any scattered light emission from circumprimary and circumsecondary disk structures. If any apparent point sources disappear when the continuum image is scaled and subtracted, scattered starlight may be the source of the emission. We also compute a direct subtraction of the continuum image from the Hα image. This is most appropriate in cases where nearby disk structures are not a concern.

3. Post-processing

3.1. Data Quality Cuts

Operating at visible wavelengths, GAPlanetS PSFs are more unstable on short timescales than NIR high-contrast images. Figure 1, which shows the median-combined PSF of each GAPlanetS image sequence, demonstrates this. Although estimation of Strehl ratios is difficult in this regime (<20%), we note that in cases where seeing data are available, the median value of $\mathrm{FWHM_{VisAO}/FWHM_{BDAvg}}$ (where BDAvg is the average of the reported seeing from the Magellan Baade telescope and the summit Differential Image Motion Monitor) is 11%, indicating approximately a factor of 10 improvement over seeing-limited imaging. The image resolutions are, on the other hand, a median of 2.8 times the diffraction limit at Hα, indicating substantial room for improvement in visible light adaptive optics imaging technology (see Section 7.2).

Large variations in the stellar PSF appear to decrease the quality of post-processed images in some cases. Lower-quality (higher FWHM) images also limit our ability to extract tightly separated point sources. In order to mitigate the effects of this variation, we built on the concept of "Lucky imaging" (Fried 1978) and developed a data-driven method to cull a proportion of the lowest-quality images for each data set. Our contrast-curve-based approach is outlined below, and its benefits are highlighted in Figure 2.

1. Eleven subsets of the full image sequence were created for each GAPlanetS data set by culling 0%, 5%, 10%, 20%, 30%, 40%, 50%, 60%, 70%, 80%, and 90% of the lowest-quality images. The metric for image quality was the peak value of a 2D Moffat fit to the central star (unsaturated data) or the ghost (saturated data). This peak value should closely trace instantaneous wave front error in the absence of significant variability on the timescale of individual exposures.
2. False planets were injected into the raw images at a contrast of 10^{-2} or 5×10^{-2} (this value for each data set is indicated in Table 3) in a spiral pattern separated by 85° in azimuth and 0.5 FWHM radially.
3. Raw images were highpass filtered with a 0.5 × FWHM Gaussian highpass filter to remove low spatial frequency structure.

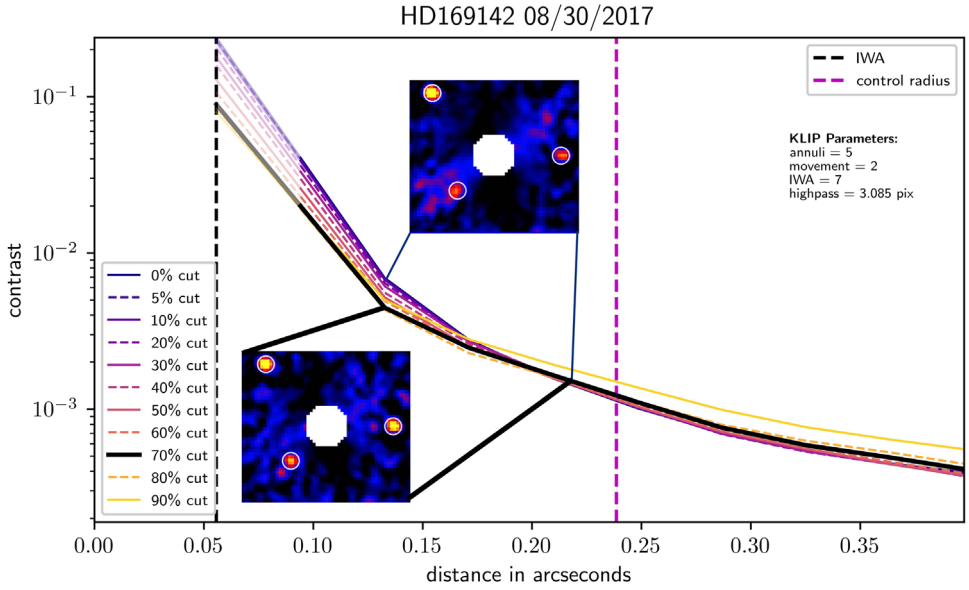

Figure 2. A representative set of contrast curves for a single data set demonstrating the methodology used to choose a "data quality cut". The colored curves reflect the contrast achieved after discarding varying proportions of the lowest-quality images. In this case, the curves converge after ∼0.″2, but the achieved contrast inside of this radius varies with the proportion of data discarded. Inset images are S/N maps showing three planets injected into raw images at separations of 0.″12, 0.″17, and 0.″22 with no data discarded (top, 0% cut) and with the selected optimal amount of data discarded (bottom, 70% cut). Recovery of the innermost two planets is markedly improved in the lower plot, increasing their recovered S/Ns by ∼2. The outer planet is recovered at equivalent S/N in both reductions, reflective of the converging of the contrast curves at this separation.

4. These images with injected false planets were passed through the KLIP algorithm with a fixed set of KLIP parameters that expertimentation indicated would yield high-quality reductions for all data sets (namely `annuli` = 5, `movement` = 2), and the ratio of their recovered-to-injected brightness was used to determine the throughput of the KLIP algorithm as a function of separation.
5. Steps 2–3 were repeated twice, with the locations of the innermost injected false planet rotated by 75 degrees each time.
6. Throughput values (which correct for KLIP self-subtraction, a strong function of angular separation) for the three sets of false planet injections were averaged in order to capture azimuthal variation in the PSF. Cases where the innermost planets were not recovered at a contrast of 10^{-2} in all three injections resulted in a repetition of steps 2–4 at a brighter injected planet contrast (5×10^{-2}). If the innermost planets were not robustly recovered at a contrast of 10^{-1}, the data set was excluded from the sample.
7. The unadulterated (no false planet) images were also passed through KLIP with the same parameters (`annuli` = 5, `movement` = 2), and the noise level was estimated as the standard deviation at each separation (corrected to reflect a t-distribution, following Mawet et al. 2014).
8. The noise level was multiplied by 5 to represent a 5σ detection and divided by the throughput to compute the detection limit at each separation, resulting in a contrast curve for each data quality cut.
9. As the optimal cut varies radially for many data sets, the proportion of images to discard was determined by eye, prioritizing the inner ∼0.″25 where planets are most likely to be found.

We note that several of the choices outlined above may have substantial influence on the "answer" for the optimal cut, most notably the choice of KLIP parameters and the aggressiveness of the highpass filter applied before PSF subtraction. We also note that our by-eye choice of the "optimal" cut is somewhat subjective, as there are several competing concerns.

First, the cut with the lowest contrast varies radially. The most common pattern (11 data sets) appears to be a crossing of curves near the AO control radius, perhaps due to a shift in the dominant noise source at this boundary. We choose to minimize the contrast curve in the inner regions where, notably: (a) accreting protoplanets are most likely to reside (Close 2020), and (b) moderate improvements in contrast are likely to yield pronounced differences in detectability. In cases where the lowest curve was only marginally lower than others inside the control radius, but was substantially higher outside the control radius, we selected a curve that balanced these two regions.

We computed contrast curves for each of the 11 cuts under 5, 10, 20, and 50 KL mode PSF subtractions. In most cases, the optimal contrasts agreed across KL modes; however, in some cases, we were forced to balance variations among them in selecting the optimum.

From a practical standpoint, the KLIP algorithm is computationally intensive, and removing some subset of images from the analysis can lead to substantial improvements in processing time. Since we apply a grid search algorithm to optimize `pyKLIP` parameters (see Section 3.2), culling the data sets was important in making processing and optimization more tractable. For this reason, in cases where contrasts were equivalent among data quality cuts, we chose the most aggressive cut.

The final adopted values for data quality cuts for each data set are given in Table 3. Figure 3 shows a representative sample of common patterns seen in these data.

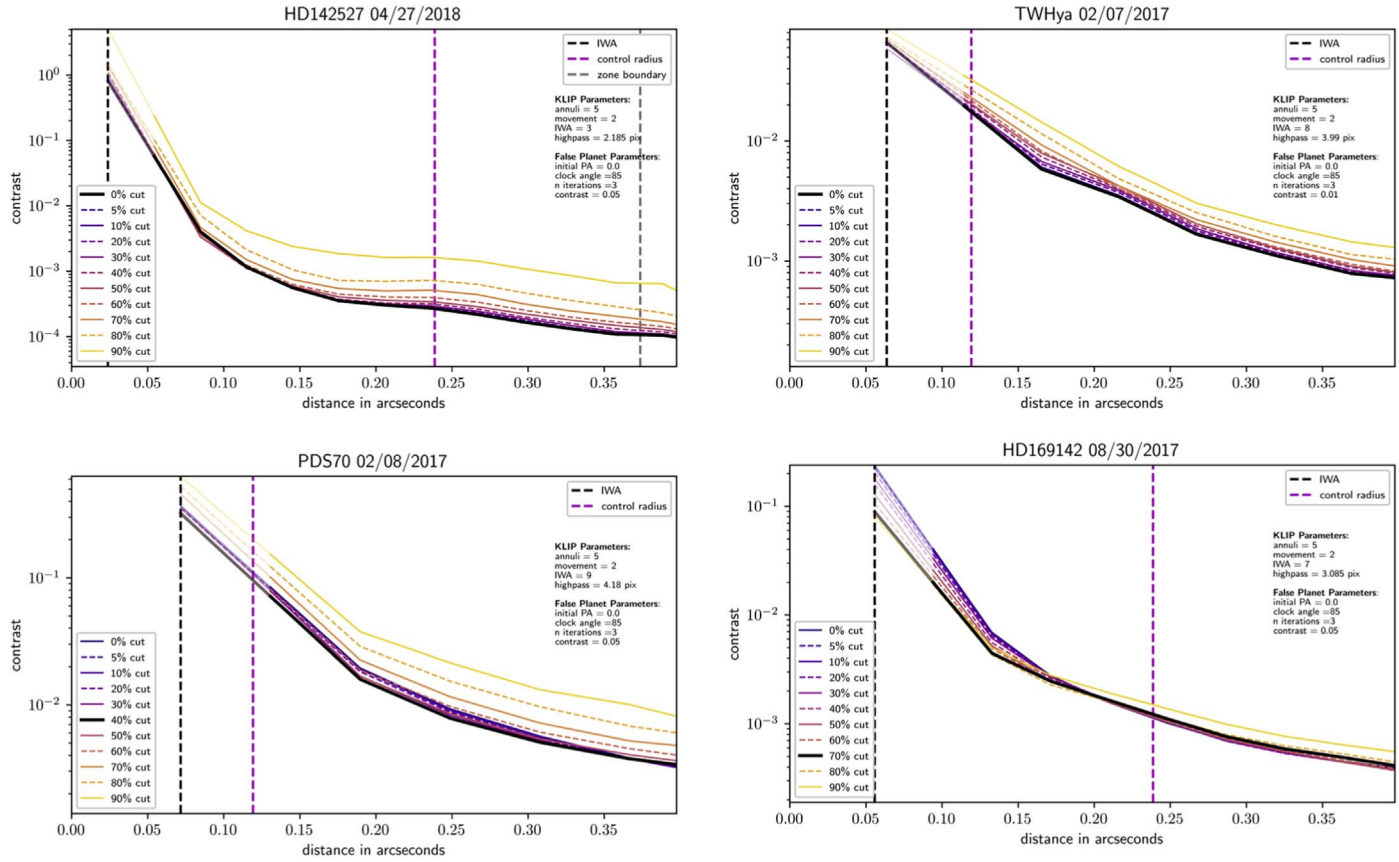

Figure 3. A representative sample of contrast curves used to cull GAPlanetS data sets before KLIP optimization. Each of our four classifications is represented here, namely (clockwise from upper left: clustered, sequential, turnover, and down-and-up). Each colored line represents the post-KLIP contrast achieved by culling different proportions (0%, 5%, 10%, 20%, 30%, 40%, 50%, 60%, 70%, 80%, and 90%) of the lowest-quality images from the sequence, where the FWHM of a Moffat fit to the central star (for unsaturated data) or ghost (for saturated data) is used as a proxy for image quality. The curve is extrapolated inward to the inner working angle following the slope of the two closest points at which throughput was computed. The curves are given higher transparency in this extrapolated region. Curves were computed with a standard set of KLIP parameters (`annuli` = 5, `movement` = 2), and are shown here for 10 KL modes (though 5, 10, 20, and 50 mode reductions were also generated and compared before making a final choice). The optimal cut was determined by eye, prioritizing achieved contrast inside of the AO control radius (though several concerns were balanced, as described in the text). Plots for all GAPlanetS data sets are available as a figure set (39 images).

(The complete figure set (39 images) is available.)

By-eye examination of the contrast curves that we used to determine data quality cuts resulted in four basic classifications among the 39 data sets. We hypothesize that these classifications are driven by a combination of (a) overall atmospheric quality, (b) variability in atmospheric quality, (c) the dominant noise regime at each separation in the image, and (d) the preservation of rotational space for the PSF library in the image sequence. An in-depth exploration of these trends is beyond the scope of this work. A sample of each of the four families of curves can be seen in Figure 3.

Clustered—data sets ($N = 16$) show equivalent, overlapping contrast curves at all separations for a range of data quality cuts from 0% to N% where N is usually in the range of 30%–50%. After this cutoff, the curves generally evolve upward (toward poorer contrasts) as the cuts get more aggressive. We hypothesize that this coincides with the point at which the total amount of rotation in the data set begins to decrease as more data are discarded.

Turnover—data sets ($N = 9$) show a marked crossing of contrast curves at some turnover point that ranges in distance from $0\farcs15$–$0\farcs3$. Inside of the turnover, the contrast generally improves as more data are discarded. The magnitude of this improvement varies. Outside of the crossover, the opposite is true, though the curves are generally more tightly clustered as distance from the star increases. We hypothesize that this turnover corresponds primarily to a switch from a speckle-limited regime at close separation to a photon-noise-limited regime at greater distance.

Dipping—curves show an improvement in contrast at all separations as an increasing proportion of data is discarded up to a certain threshold, after which the contrast gets poorer again as more data are discarded. Sometimes this is true at all separations ($N = 2$), but this pattern is seen more often in the inner ($r < 0\farcs2$) regions only while the outer regions exhibit some other pattern ($N = 8$).

Sequential—curves show a global evolution in which the contrast is either improving ($N = 1$) or worsening ($N = 4$) steadily as the amount of data discarded increases.

Further optimization of this approach is warranted, and includes incorporation into our broader post-processing grid search and more rigorous exploration of the patterns outlined above as they relate to data set properties and noise regimes.

3.2. Optimization of KLIP Parameters with `pyKLIP-PE`

Variation in the final appearance of PSF-subtracted images according to algorithmic parameters is now a well-established

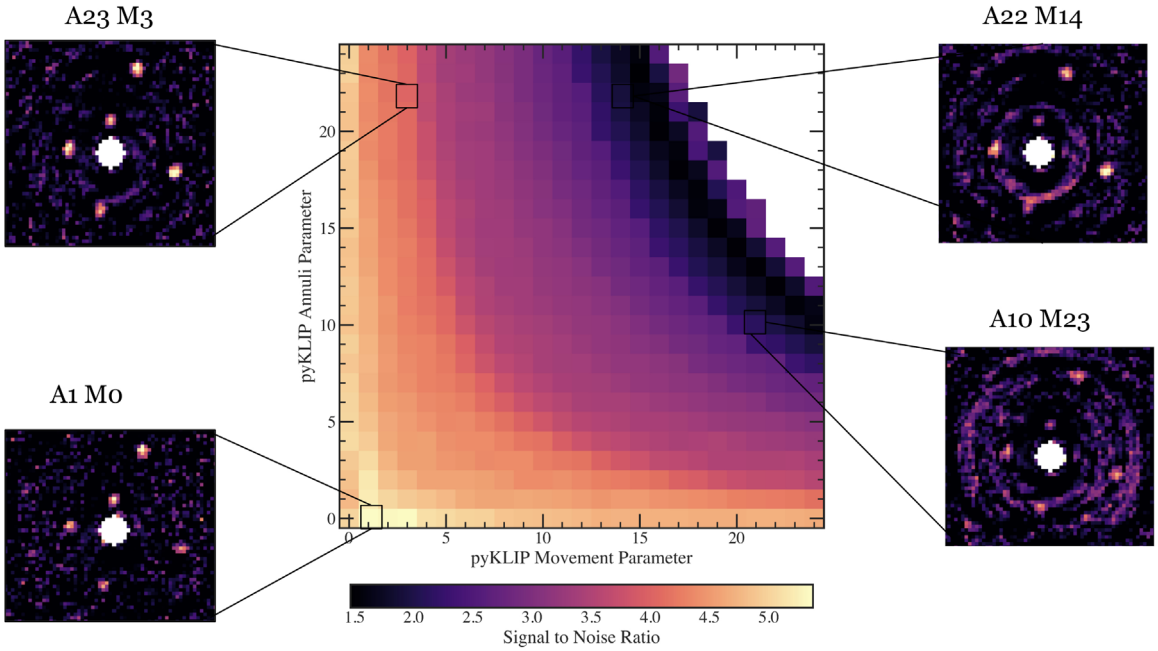

Figure 4. A representative `pyKLIP-PE` output heat map depicting the quality of recovery of the innermost false planet (of five total) injected at $r \sim 0\farcs06$ into the continuum imagery of HD 169142. The *x*- and *y*-axes of the central heatmap represent the values of the tunable KLIP `annuli` and `movement` parameters, respectively. The value in each cell of the heatmap is equal to the peak S/N of the innermost false planet when reduced under those `pyKLIP` parameters and with a 10 KL mode PSF model. Each pixel therefore represents one KLIP reduction; this is further shown in the inset images, which depict the full S/N maps for four of the pixels in the heatmap. There is a clear optimal region for robust extractions of this innermost planet signal, and other combinations of KLIP parameters that are suboptimal. The white region in the upper-right corner reflects KLIP annuli/movement combinations for which no reference images remain in the PSF library and KLIP cannot be completed. The heatmap is shown here for 10 KL modes, the innermost planet, and the four selected annuli/movement combinations only. However, a fully interactive version of this figure is available, which allows the user to select an arbitrary movement/annuli combination, injected planet, KL mode, and image quality metric.

fact (e.g., Milli et al. 2012; Meshkat et al. 2013; Follette et al. 2017) and can be easily seen in Figure 4. In order to make well-justified data-driven decisions about optimal parameter choices for each morphologically complex GAPlanetS system, we completed a coarse grid search of select KLIP parameters for each data set individually.

This "`pyKLIP` Parameter Explorer" (`pyKLIP-PE`) algorithm calculates a number of post-processed image quality metrics for real and/or injected point sources with a range of `pyKLIP` `annuli`, `movement`, `subsections`, and `numbasis` (KL modes) parameters. In this work, we have chosen to optimize recovery of false planets injected into continuum images. Injection of synthetic planets allows us to balance post-processed image quality across a broad image region, optimize data sets without known point sources, and avoid cognitive biases in the selection of parameters for recovery of controversial planet candidates. A companion paper to this work (Adams Redai et al. 2023) details the `pyKLIP-PE` algorithm and validation of its use for optimization of point-source recovery in GAPlanetS data. Here, we summarize the results in broad strokes, and refer the reader to Adams Redai et al. (2023) for details.

To make `pyKLIP-PE` computational time tractable for the entire GAPlanetS database, we applied fixed choices for the `pyKLIP` `subsections` ($n = 1$), `IWA` (IWA = FWHM), and `highpass` (0.5 × FWHM) parameters. These were selected to optimize point-source recovery (by applying an aggressive highpass filter) in a region where we might reasonably expect to resolve point sources (beyond 1 FWHM of the central star).

False planets are constructed by scaling images of the central star (unsaturated data sets) or ghost (saturated data sets) to a particular contrast. Individual exposures are used for this purpose so that the PSF of the injected companion in each image mirrors that of the star, as would be expected for a true planet. For each data set, planets are injected between $r = 1.5 \times$ FWHM and the AO control radius with an angular separation of 85° and a radial separation of 1 FWHM for AO bin 1 (control radius = 30 pixels) data sets, and 0.5 × FWHM for bin 2 (control radius = 15 pixels) data sets.

Contrasts for injected planets are iterated upon until their recovered S/Ns under a conservative choice of KLIP parameters (`annuli` = 5, `movement` = 2) has an average across 5, 10, 20, and 50 KL modes of 6.5–7.5. This S/N ∼ 7 threshold was selected to be somewhat higher than the canonical detection threshold of S/N = 5 so that a range of KLIP parameter combinations would result in robust (S/N > 5) detections.

The result of the `pyKLIP-PE` algorithm is a multidimensional array of image quality metrics (planet S/N, false-positive pixel count, etc.) for various combinations of KLIP parameters. In principle, there could be one dimension to this grid for each of the more than 20 parameters of the `pyKLIP` algorithm. However, we have chosen to focus on optimizing only a few key parameters and have made data-driven decisions about reasonable fixed choices for others, as described in detail in Adams Redai et al. (2023).

3.2.1. Optimized Parameters

The principal `pyKLIP` parameters optimized for the final GAPlanetS reductions were the `annuli`, `movement`, and `numbasis` (KL mode) parameters, described briefly below.

1. The pyKLIP annuli parameter sets the number of concentric, equal width, annular zones that are analyzed separately by KLIP. The exact width of the annuli in pixels varies very slightly among data sets due to variation in IWA, but ranges from roughly 225 pixels wide for 1 annulus to ∼9 pixels wide for 25 annuli.
2. The pyKLIP movement parameter controls rotational masking. All images where a planet would have rotated by fewer than a given number of pixels between the target image and the reference image(s) are excluded when constructing a PSF for the target image, thereby limiting self-subtraction. Low values of the movement parameter are thus "aggressive" values, with very few images excluded from the reference set and more prominent self-subtraction. A single movement value applied in multiple zones across an image is also more aggressive for annuli near the center of the image, where a given number of pixels of rotation about the image center translates to a larger angular exclusion criterion. When the movement parameter becomes high enough, there are no remaining reference images that meet the exclusion criterion, and KLIP reductions are impossible.
3. The pyKLIP numbasis parameter determines the number of principal components, or "KL modes," used to construct the final PSF. KL modes are a set of orthogonal basis vectors constructed from the PSF reference library, where the first mode is the vector that describes the most variance, and each subsequent mode describes some additional (smaller) amount of variance in the data set. Thus, increasing the number of KL modes increases the complexity of the PSF model.

3.2.2. Image Quality Metrics

The pyKLIP-PE algorithm extracts four image quality metrics for injected (or real) companions. These are: (1) the peak pixel values of each planet in the S/N map ("peak S/N metric"), (2) the average S/N of all positive pixels within 0.5 × FWHM radially and 5° azimuthally of each planet in the S/N map ("average S/N metric"), (3) the achieved contrast at the location of each planet, and (4) the number of false-positive ($>5\sigma$) pixels between the IWA and the AO control radius. An additional two metrics, which we call "neighbor quality" metrics, are computed by smoothing the peak and average signal-to-noise metrics across pyKLIP's movement and annuli parameters. These metrics are based on the anecdotal understanding prevalent in the community that the most robust KLIP detections are those where small variations in KLIP parameters do not substantially affect the recovered planetary S/N.

In this work, we choose a simple equally weighted sum of all six normalized metrics. We then average the sum of these normalized metrics across all false planets, thereby balancing recovery of signals throughout the region of interest. As a further measure to ensure robustness, we average the 5 and 20 KL mode aggregate parameter quality maps before selection of a final movement, annuli combination. As described in detail in Adams Redai et al. (2023), these particular KL modes were chosen based on the statistical distribution of optimal parameter choices for HD 142527 B recovery under a range of optimization scenarios.

Effectively, this methodology means that the algorithm attempts to select an annuli and movement combination that results in robust (according to all six metrics) extraction of injected planets throughout the region of interest for both low ($n = 5$) and moderate ($n = 20$) PSF model complexity. Once this combination of annuli and movement parameters is chosen, the final choice of "optimal" KL mode is made by maximizing the sum of all six metrics for that data set averaged over all injected planets. Optimal annuli, movement, and numbasis (KL mode) parameters selected using this methodology are reported for each data set in Table 3. Unless otherwise indicated, all post-processed images shown in this work have pyKLIP parameters selected via this methodology.

Figure 5 shows two examples of normalized parameter quality maps for all six image quality metrics averaged across all injected continuum planets and among 5 and 20 KL modes. The aggregate parameter quality map is shown in the large panel at right, and the optimal annuli and movement parameters are indicated. A complete description of how we arrived at this method, as well as detailed discussion of the features of these maps, can be found in Adams Redai et al. (2023).

4. Survey Analysis Methodologies

In this section, we provide explanations of various methods used to generate the final, optimized images and sensitivity limits for the GAPlanetS companion candidate search, results of which appear in Sections 5 and 6. We also detail the tools used for candidate characterization, including the procedure for obtaining a final estimation of mass accretion rate.

KLIP-ADI images—are shown in Section 5 and Appendix B for all GAPlanetS targets. For those targets with known companions or companion candidates detected in GAPlanetS data, all epochs (including nondetection epochs) are shown in the main body of the text for completeness. As there are less robust 2σ–4σ excess signals at a number of locations in most data sets, additional epochs for objects without recovered candidate companions are shown in Appendix B. Some of these signals may prove in the future to be protoplanets upon higher-contrast follow-up and/or additional epochs of observation. The positions of confirmed and candidate companions in GAPlanetS systems are compiled from the literature in Table 4, and these positions are indicated in the ASDI images for each system.

Optimization strategies—One important consideration in extracting point-source signals from these data is whether to conduct analyses on post-processed images that have undergone conservative KLIP parameter optimization (on false planets injected into the continuum data, as described and shown in Section 3.2.), or to optimize on the known location of the companion(s) in Hα images. The relative merits of each of these strategies is discussed in detail in Adams Redai et al. (2023). In short, optimization on false planets injected into the continuum data is a robust method that is substantially less likely to yield false-positive detections. We apply it to all data sets to achieve a uniform analysis. However, there is necessarily a penalty in the final S/N of recovered Hα companions by virtue of the optimizations being done on a different (albeit contemporaneous and close in wavelength) data set and averaged over planets located throughout the region of interest rather than at a particular PA and separation. In the case of very robust high-S/N recoveries, this penalty is of minimal concern as the

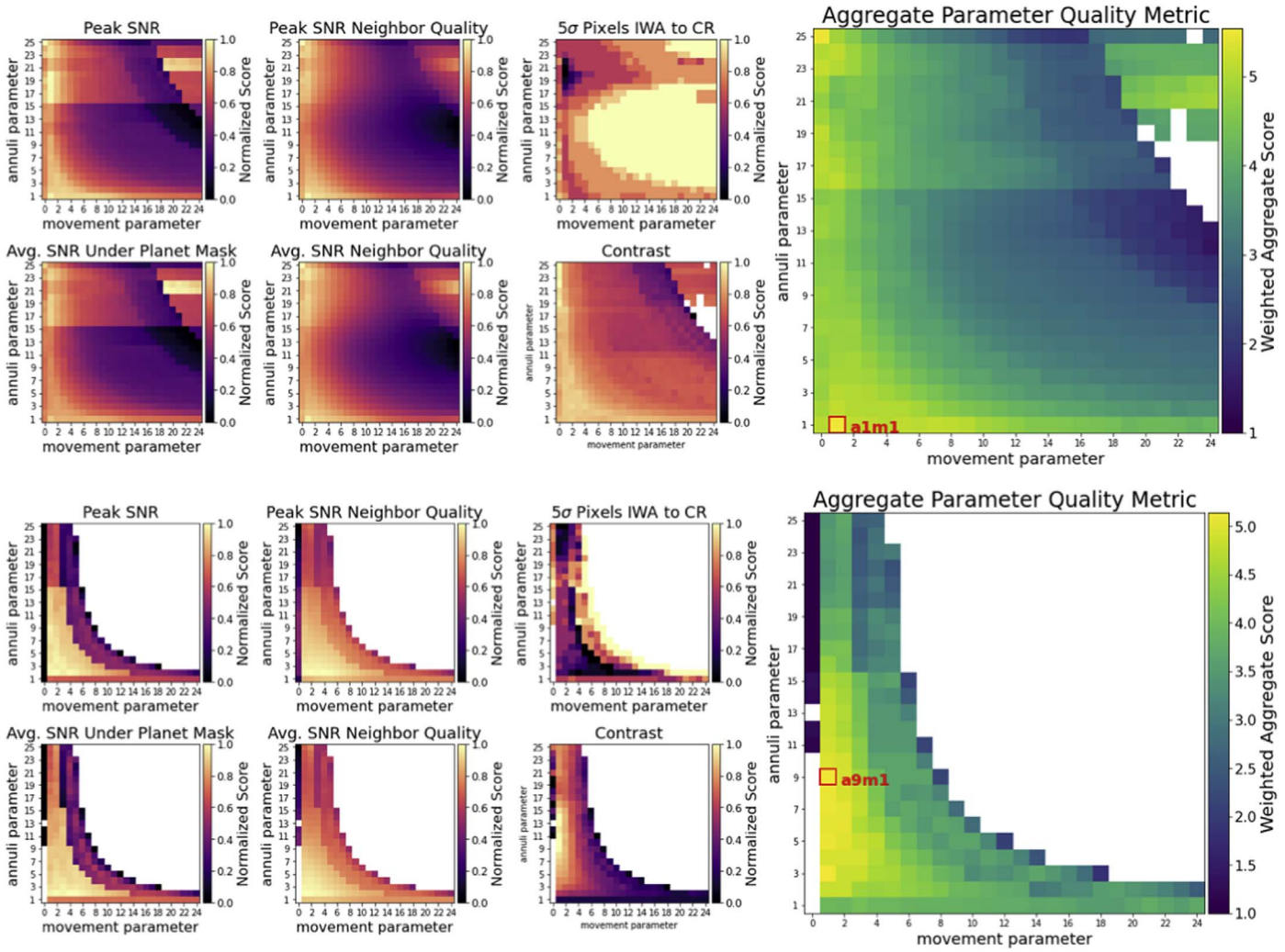

Figure 5. Sample `pyKLIP` parameter quality heatmaps for two representative data sets (top: HD 169142 04/08/2014, bottom: CS Cha 05/15/2015) and for all six post-processed image quality metrics. Each small subpanel maps the normalized value of a different image quality metric, and each pixel represents the value of that metric averaged across all of the false planets in the `pyKLIP` post-processed image with the `movement` and `annuli` values indicated on the *x*- and *y*-axes, respectively. In this case, the heatmaps for 5 and 20 KL modes have also been averaged to ensure stability among low and moderate KL modes. The individual metrics in the six subpanels are weighted (equally in this case) and combined to form an aggregate parameter quality metric (rightmost panel), from which an "optimum" parameter combination is selected (indicated in red). The nature of each individual metric is described in detail in the text. White pixels represent either parameter combinations for which metrics were not able to be extracted (often the case for `movement` = 0) or where the aggressiveness of the rotational mask leaves no reference images in the PSF library (upper right of each plot). Plots for all GAPlanetS data sets are available as a figure set (39 images).

(The complete figure set (39 images) is available.)

companion is recovered using both strategies. However, in the case of detections at or near the detection threshold, this S/N penalty may result in nonrecovery of the companion under the continuum optimization method. In cases where the point-source nature of the companion is robustly established in the literature (HD 142527 B and PDS 70 b and c, all of which have been detected at continuum wavelengths in addition to Hα) and the companion is unrecovered under the standard survey optimization methodology, we report optimizations done directly on the Hα imagery at the companion location as well. We note that such direct optimization on the Hα images, though it is more likely to result in a recovery of planetary signal, risks overfitting and should be interpreted with caution. To mitigate this somewhat, we adopt a relatively conservative version of this direct optimization approach by averaging across several KL modes and image quality metrics (for difficult HD 142527 B recoveries) or across several known companions (for PDS 70).

ASDI images—All KLIP image panels (Figures 7–13 and all figures in Appendix B) show Hα (left) and continuum (middle left) reductions, as well as two ASDI images. The first (middle right) image is a conservative reduction computed by scaling the `pyKLIP`ed continuum image up by the median stellar Hα/continuum brightness ratio (as described in Section 2.4). The second (right) ASDI reduction is computed by subtracting the two at a 1:1 scale. The relative fidelity of the two types of SDI reduction is nuanced and is discussed in detail in Section 2.4. To recap briefly here, scaling and subtracting by the Hα/continuum brightness ratio should effectively remove both scattered light and stellar residuals, where present. However, in the absence of such signals/residuals, the 1:1 scaled reduction is the more accurate indicator of Hα excess.

Table 4
Reported and Predicted Positions for Companions and Companion Candidates

Object	Label	Epoch(s)	Sep (pix)	Sep Error (pix)	PA (deg)	PA Error (deg)	Source
Previous GAPlanetS Detected Objects with Epoch-Specific Location Measurements/Predictions							
HD 142527	B	04/11/2013	10.2	0.1	126.0	0.5	Balmer et al. (2022)
HD 142527	B	04/08/2014	9.7	0.2	115.9	1.0	Balmer et al. (2022)
HD 142527	B	05/15/2015	8.4	0.2	109.6	0.8	Balmer et al. (2022)
HD 142527	B	05/16/2015	8.6	0.3	108.6	1.0	Balmer et al. (2022)
HD 142527	B	05/18/2015	8.6	0.2	110.2	0.7	Balmer et al. (2022)
HD 142527	B	02/10/2017	6.4	0.2	77.8	2.0	Balmer et al. (2022)
HD 142527	B	04/27/2018	4.8	0.3	58.0	1.8	Balmer et al. (2022)
PDS 70	WiPb	02/08/2017	23.3	0.2	149.7	0.3	Wang et al. (2021b)
PDS 70	WiPc	02/08/2017	28.1	0.1	283.8	0.2	Wang et al. (2021b)
PDS 70	WiPb	05/02/2018	22.6	0.1	146.8	0.3	Wang et al. (2021b)
PDS 70	WiPc	05/02/2018	27.7	0.1	281.2	0.1	Wang et al. (2021b)
PDS 70	WiPb	05/03/2018	22.6	0.1	146.7	0.3	Wang et al. (2021b)
PDS 70	WiPc	05/03/2018	27.7	0.1	281.2	0.1	Wang et al. (2021b)
LkCa 15	S14b	11/16/2014	11.7	1.0	256	3	Sallum et al. (2015)
LkCa 15	S14c	11/16/2014	10.1	1.5	318	11	Sallum et al. (2015)
LkCa 15	S14d	11/16/2014	10.9	8.8	14	30	Sallum et al. (2015)
LkCa 15	S16b	11/18/2016	12.2	0.8	248	2	Sallum et al. (2016)
LkCa 15	S16c	11/18/2016	10.9	0.5	301	2	Sallum et al. (2016)
LkCa 15	S16d	11/18/2016	10.3	2.0	348	5	Sallum et al. (2016)
Other Candidate Detections and Predictions from the Literature							
PDS 70	Z20d	Feb–Jul 2020	13.8	NR	310	NR	Zhou et al. (2021)
HD 169142	O07	June 2007	14.6	2.5	250.0	5.0	Okamoto et al. (2017)
HD 169142	O12-13	2012-2013	42.8	NR	175.0	NR	Osorio et al. (2014)
HD 169142	R13	June 2013	19.6	4.0	7.4	11.3	Reggiani et al. (2014)
HD 169142	B13	July 2013	13.8	3.8	0.0	14.0	Biller et al. (2014)
HD 169142	B14	April 2014	22.6	NR	33.0	NR	Biller et al. (2014)
HD 169142	G15-17A	2015–2018	14.5	1.9	239.0	11.5	Gratton et al. (2019)
HD 169142	G15-18B	2015–2018	23.8	1.0	17.0	8.0	Gratton et al. (2019)
HD 169142	G15-18C	2015–2018	24.8	1.1	308.0	9.0	Gratton et al. (2019)
HD 169142	G15-18D	2015–2018	39.9	0.9	39.0	5.0	Gratton et al. (2019)
HD 169142	B18	July 15, 2018	13.3	4.4	55.5	4.0	Bertrang et al. (2020)
HD 100546	Q11	May 2011	59.0	1.5	7.0	1.4	Quanz et al. (2013)
HD 100546	C15	Jan 2015	16.5	1.1	150.9	2.0	Currie et al. (2015)
HD 100546	S15-16	2015–2016	57.2	0.9	11.5	1.1	Sissa et al. (2018)
HD 100546	F15-16	2015–2016	121.3	NR	10	NR	Fedele et al. (2021)
SAO 206462	C16	March 2016	8.9	0.6	19.0	3.0	Cugno et al. (2019)
SAO 206462	C19	July 13, 2019	53.6	0.2	212.4	0.7	Casassus et al. (2021)
TW Hya	I16	Dec 2016	105.7	8.5	242.5	2.1	Ilee et al. (2022)
TW Hya	T17	May 2017	108.9	0.1	237	1	Tsukagoshi et al. (2019)
TW Hya	H19	March 15, 2019	20.1	1.3	190	1	Huélamo et al. (2022)
CS Cha	G17	Feb–Jun 2017	165.6	0.6	261.4	0.2	Ginski et al. (2018)
HD 100453	W17	Feb 17, 2017	132.83	0.40	132.32	0.18	Wagner et al. (2018b)
HD 100453	G19	April 7, 2019	135.1	4.0	132.7	0.8	Gonzalez et al. (2020)
V1247Ori	W12-13	2012–2013	5.2	0.8	305.5	5.5	Willson et al. (2019)

Note. Compilation of reported and predicted positions for objects with GAPlanetS detections (top) and nondetections (bottom). The "Label" in column 2 corresponds to the text label at this candidates' location in Figures 8, 9, 10, 11, 13, 15, and Appendix B Figures 20, 21, 23, 27 and 28. Text labels correspond to the first letter of the last name of the study author and the epoch of observation (not publication). In cases where the candidate was detected more than once, the full range of dates at which it was recovered is indicated. In these cases, the "Sep Error" and "PA Error" columns indicate the full range of possible positions due to both apparent orbital motion and astrometric uncertainty reported in the original reference, and the "sep" and "PA" columns are the central value for each of these ranges. An "NR" designation indicates that the uncertainty value was not reported in the publication.

We show both, as well as the `pyKLIP`-reduced Hα and continuum images in order to provide full context with which to judge the fidelity of any apparent signals.

Robustness of signals among Hα and SDI images—is an important concern in extracting accurate photometry and astrometry for GAPlanetS candidates. The highest-fidelity signals are present in both Hα and SDI images. While the SDI process helps to remove disk signal and stellar residuals, as well as the continuum contribution of objects like HD 142527 B, it can also induce false-positive signals into SDI imagery. This occurs when a negative speckle in the KLIP-processed continuum images is reversed during SDI

subtraction, becoming positive. Negative continuum speckles with sufficient amplitude to mimic planetary signals are relatively uncommon, but are visible and appear point-source-like in several GAPlanetS data sets ($n = 2$). These spurious point sources are marked with yellow "x" symbols in all SDI images where they are apparent.

Multiepoch combinations—(post-KLIP mean combinations) are utilized in cases where independent data sets were acquired for a given object within several days of one another. Although this technique of combining post-processed KLIPed images from multiple near-in-time epochs has been shown to yield detections in some cases where single epoch images do not reveal a high-S/N source (e.g., Wagner et al. 2018a), we caution that accreting companions are also likely variable, so higher-S/N detections will only result in cases where the object is accreting at a detectable rate in both epochs. Given the detectable level of Hα variability seen on night-to-night timescales in GAPlanetS objects (see Balmer et al. 2022), accretion rates derived from combined data should be interpreted with caution.

Contrast curves–are shown at Hα for all data sets in Figures 6, 14, 16, and 17. These contrast units are then translated into generalized mass accretion rate limits for the overall survey in Section 6.

Astrometry and photometry of detected companions—is computed via the Bayesian KLIP Astrometry (BKA) technique described in detail in Wang et al. (2016) and implemented via `pyKLIP`. In short, the technique creates a forward model by projecting one or more PSFs onto the KL basis set. This results in a post-processed PSF that replicates the complex shape of the planetary core and self-subtraction lobes unique to a given data set, choice of KLIP parameters, and point-source location. This forward-modeled PSF is adjusted astrometrically and photometrically to produce quality-of-fit posterior distributions. BKA input can be either a single fixed PSF or a time-variable PSF cube. Given the demonstrated high degree of PSF variation in GAPlanetS data, we have opted for the latter. Our input PSF model is therefore a time series of normalized image stamps, one per image in the sequence.

Contrasts of companion candidates are also fit with BKA. In our case, we ensure that the PSF model has a fixed contrast relative to the primary star by multiplying the (normalized) PSF model by a fixed contrast relative to the central star. Preprocessed images are also normalized prior to injecting false planets and running KLIP by dividing each image by the peak value of a Moffat fit to the central star in the case of unsaturated data orthe ghost multiplied by the established ghost-to-star scale factor in the case of saturated data. By normalizing the input images to a peak value of one and the input PSF to the "best guess" contrast, this ensures that the simulated point source is modeled at a fixed contrast relative to the time-varying central PSF. After computation of the forward model, the post-processed PSF brightness is iterated upon during BKA analyses with a scale factor parameter that we multiply by the initial contrast guess to get the final best-fit contrast value for a companion.

We report the median values of BKA posterior distributions for separation, position angle, and contrast for each GAPlanetS companion candidate, with the 67% credibility interval reported as the uncertainty. Uncertainty on absolute astrometric calibration of the instrument and the location of the central star in the images is incorporated into the error estimation for those

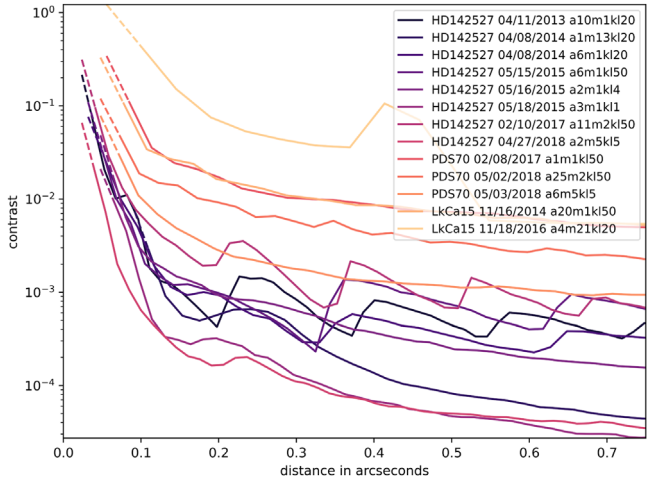

Figure 6. Throughput-corrected 5σ contrast curves of all epochs for continuum false planet optimized `pyKLIP` reductions of the three previously reported GAPlanetS companion and companion candidate-hosts: HD 142527 (seven epochs), PDS 70 (three epochs), and LkCa 15 (two epochs). Throughput was computed as described in the text, with a correction for the small number of independent noise samples near the star following Mawet et al. (2014). Solid curves indicate regions where throughput-corrected contrast was computed directly. The curves are also projected inward from the innermost throughput measurement to the inner working angle, and this extrapolated region is indicated with a dashed line.

quantities. However, the reported error bars for contrast encompass only the 67% credibility interval for the scale factor posterior and not any uncertainties in photometric calibration, which we propagate separately into accretion rate estimates as described in detail in Section 6.

In order to further quantify the strength of our detections, we utilize the `PlanetEvidence` class (Golomb et al. 2019) within `pyklip` to conduct a Bayesian model comparison and make a more conservative S/N estimate for each companion detection. These values are reported in Table 5. `PlanetEvidence` uses the nested sampling implementation `pyMultiNest` (Feroz et al. 2009; Buchner 2014) to compare two models: H_0, where the image contains only speckle noise, and H_1, where the image contains a source at the position of the companion. `PlanetEvidence` returns marginal distributions of the parameters for the source and null cases, and calculates the S/N of the detection within the fitting region and the evidence values for H_0 and H_1 (Z_0 and Z_1). The log-ratio of these evidence values, $\log B_{10} = \log Z_1/Z_0$, enables us to quantify the confidence with which one model can be favored over the other. This framework provides a more robust estimate of the quality of the detection because it better captures asymmetric speckle noise, which can dominate at very close separations. Values for $\log B_{10} > 5$ are considered "strong" evidence against the null hypothesis.

We note that `PlanetEvidence`-extracted S/N and $\log Z_1/Z_0$ values are sensitive to the size of the BKA fitting region, and can vary by $\sim$10% based on this choice. We adopt a 15 pixel square fitting region for all forward model fits except in cases where nearby residual structure results in a clear under- or over-subtraction of the point-source candidate.

5. Individual Object Results

This section outlines GAPlanetS results for each transitional disk in the sample and describes in basic terms the recovery (or

Table 5
Results of BKA Forward Model Fitting

Object	Date DD-MM-YY	Separation (mas)	PA (deg)	log(C)[a]	log(Z_1/Z_0)	S/N	Δmag[b] (mag)	log($L_{H\alpha}$) ($L_\odot$)	log($M\dot{M}$) A17[c] (M^2_{Jup} yr^{-1})	log($M\dot{M}$) A21[d] (M^2_{Jup} yr^{-1})
Hα Fits to Protoplanetary Companions and Candidates										
PDS 70 c	2017-02-08	246.9 ± 4.4	284.2 ± 0.6	−2.53 ± 0.16	11	4.5	6.02 ± 0.41	−5.48 ± 0.19	−6.5	−5.6
LkCa 15 "b"	2014-11-16	69.7 ± 6.1	242.6 ± 2.7	−1.52 ± 0.28	18	3.5	3.14 ± 0.69	−3.82 ± 0.29	−4.6	−4.1
CS Cha "c"	2015-05-15	68.1 ± 1.4	76.3 ± 1.1	−1.29 ± 0.03	11	4.3	2.34 ± 0.08	−3.00 ± 0.1	−3.7	−3.3
Hα Fits to Stellar Companions									log($\dot{M}$) A17 ($M_\odot$ yr^{-1})	
HD 142527 B	2013-04-11	82.7 ± 1.3	128.2 ± 0.6	−2.68 ± 0.01	453	13.6	6.83 ± 0.06	−4.07 ± 0.25	−10.8	⋯
HD 142527 B	2014-04-08	74.5 ± 1.5	120.4 ± 0.8	−2.77 ± 0.02	87	8.2	6.79 ± 0.05	−4.07 ± 0.3	−10.8	⋯
HD 142527 B	2015-05-15	67.4 ± 1.8	110.7 ± 1.1	−2.65 ± 0.09	54	4.6	6.49 ± 0.4	−3.86 ± 0.39	−10.5	⋯
HD 142527 B	2015-05-16	71.6 ± 1.5	107.7 ± 0.8	−2.76 ± 0.13	58	6.2	6.76 ± 0.46	−3.92 ± 0.39	−10.6	⋯
HD 142527 B	2015-05-18	72.6 ± 1.3	109.6 ± 0.7	−2.62 ± 0.01	145	10.3	6.44 ± 0.3	−3.93 ± 0.38	−10.6	⋯
HD 142527 B	2018-04-27	43.7 ± 1.3	54.4 ± 1.5	−2.9 ± 0.07	28	4.1	6.99 ± 0.36	−3.99 ± 0.39	−10.7	⋯
HD 100453 B	2018-05-02	1033.9 ± 13	133.1 ± 0.2	−2.96 ± 0.01	inf	30.6	7.35 ± 0.3	−4.54 ± 0.19	−11.8	⋯
Continuum Fits to Stellar Companions										
HD 142527 B	2013-04-11	82.6 ± 1.4	127.9 ± 0.6	−3.01 ± 0.05	162	6.4	7.53 ± 0.13	⋯	⋯	⋯
HD 142527 B	2014-04-08	71.3 ± 2.2	118.3 ± 1.5	−2.99 ± 0.15	14	4.2	7.47 ± 0.37	⋯	⋯	⋯
HD 142527 B	2015-05-15	63.9 ± 2	112.9 ± 1.5	−2.95 ± 0.2	12	2.8	7.38 ± 0.6	⋯	⋯	⋯
HD 142527 B	2015-05-16	76.6 ± 2.5	107.6 ± 1.2	−3.14 ± 0.31	11	2.2	7.84 ± 0.83	⋯	⋯	⋯
HD 142527 B	2015-05-18	73.7 ± 1.4	110.2 ± 0.8	−2.85 ± 0.02	88	7.5	7.12 ± 0.29	⋯	⋯	⋯
HD 142527 B	2018-04-27	42.1 ± 2.1	54.6 ± 2.3	−3.27 ± 0.56	5	1.80	8.17 ± 1.42	⋯	⋯	⋯
HD 100453 B	2018-05-02	1035.1 ± 13	133 ± 0.2	−3.13 ± 0.01	inf	31.1	7.81 ± 0.29	⋯	⋯	⋯

Notes.
[a] Reported uncertainty in contrast reflects only the 67% credibility interval of the BKA posterior fit to the photometric scale factor. Full photometric errors are reflected in the Δmag column.
[b] For all Hα fits, this is the Δmag relative to the stellar continuum, calculated by multiplying the candidate contrast by the Hα-to-Continuum scale factor for the star (given in Table 2). The uncertainty reported on this quantity reflects a full photometric error accounting, as described in detail in the text.
[c] Accretion rates estimated from the empirical L_{acc}–L–Hα scaling law of Alcalá et al. (2017). These are reported as $M\dot{M}$ values in units of M^2_{Jup} yr^{-1} for the protoplanets and protoplanet candidates, as their masses are not well constrained. For the stellar companions, the known masses are used to estimate a true accretion rate in $M_\odot$ yr^{-1}. We estimate the uncertainty on accretion rates derived under this model as ± 1 dex, as described in detail in the text.
[d] Accretion rates estimated from the theoretical L_{acc}–L–Hα scaling law of Aoyama et al. (2021), reported only for those candidates that are not known stellar companions, as the accretion paradigm applied in these models is planetary in nature. We estimate the uncertainty on accretion rates derived under this model as ± 2–3 dex, as described in detail in the text.

lack thereof) of confirmed or candidate protoplanets. In each case, the data have been preprocessed as described in Section 2, culled as described in Section 3.1, post-processed with `pyKLIP` with parameters optimized for false planets injected into continuum images as described in Section 3.2, and images and contrast curves generated following the methods described in Section 4.

The object-by-object results are aggregated in this section into previously reported GAPlanetS detections (Section 5.1), new planet candidates (Section 5.2), other objects for which known or candidate companions exist in the literature (Section 5.3), , and objects with no known or candidate companions (Section 5.4). Survey-level analyses follow in Section 6. Literature predictions for the locations of companions and companion candidates are shown in all images, and these predictions are compiled in Table 4. In most cases, literature candidate companions are not detected in GAPlanetS imagery, and detection limits at their predicted locations are summarized in Section 6.2.

In cases where companions or companion candidates are successfully detected in Hα and/or Continuum GAPlanetS imagery, best-fit astrometry and photometry, computed as described in Section 4, is summarized in the text. Astrometric and photometric fit statistics and forward models follow in Section 6.1.

5.1. Objects with Previously Reported GAPlanetS Detections

GAPlanetS data have already revealed three low-mass accreting companions and companion candidates: HD 142527 B, LkCa 15 "b", and PDS 70 b, reported in Close et al. (2013), Sallum et al. (2015), and Wagner et al. (2018a), respectively. In this section, we present uniform reprocessings of the data for each of these targets under the GAPlanetS campaign framework, as well as contrast curves for all epochs (see Figure 6).

5.1.1. HD 142527

The HD 142527 GAPlanetS data sets served as an excellent resource for optimizing and testing registration, centering, flat-fielding, data set selection, and parameter optimization techniques for the GAPlanetS pipeline. The presence of the robust, high-S/N companion HD142527 B allowed us to gauge the relative efficacy of various algorithmic choices on the recovery of the real companion at tight separation.

GAPlanetS data were collected for HD 142527 in 2013, 2014, 2015, 2017, and 2018. We include continuum-optimized imaging and contrast results for all epochs in Figure 7, and Hα optimized reductions for the most difficult detections in Figure 8.

Photometric and astrometric monitoring and orbit fitting of HD 142527 B are the subject of a companion paper (Balmer et al. 2022) and are not discussed in detail here. Importantly, Balmer et al. (2022) refined the orbit of the companion and demonstrated that it is significantly misaligned ($\theta > 30°$) with respect to both the inner and outer disk components. We touch briefly on consistency between our astrometric and photometric fits and those of Balmer et al. (2022) in Section 6.

Figure 7 demonstrates that HD 142527 B is easily recovered in Hα, continuum, and SDI imagery in data sets from 2013 (S/N = 10.5/7.5/5.6 for Hα, continuum, and 1:1 scaled SDI imagery, respectively), 2014 (S/N = 6.8/3.6/4.6), 2015 May 15 (S/N = 9.0/3.7/8.0), 2015 May 16 (S/N = 5.7/3.5/4.1) and 2015 May 18 (S/N = 7.0/5.2/4.5) following the bulk survey strategy of optimizing on false planets injected into continuum images.

The 2017 and 2018 HD 142527 data sets are substantially more difficult detections than the 2013–2015 epochs, as the predicted separation of HD 142527 B is much tighter in these epochs (0.″05, ∼6pix). We attempted both continuum-optimized and Hα companion-optimized reductions of these data sets. The companion is recovered in 2018 Hα data at an S/N of 3.9 in the direct Hα optimized reduction, but is not recovered in 2017 under either optimization method. The reason for this is readily visible in the contrast curves of Figure 6, which reveal that even the most highly optimized `pyKLIP` reduction of the 2017 data set boasts nearly an order-of-magnitude poorer contrast at the location of the companion than the next-lowest-quality data set. This is likely a result of both the extremely tight separation of the companion at this epoch and the small amount of on-sky rotation obtained (16.°1). More detail on the nature of the 2018 recovery is provided in Balmer et al. (2022).

The source of the ∼140 au (Avenhaus et al. 2014) gap in HD 142527 has been debated, in particular whether the binary companion HD 142527 B can be solely responsible for carving the wide central cavity (Fukagawa et al. 2006; Biller et al. 2012; Casassus et al. 2015; Price et al. 2018). In 2014 and 2015, we conducted deep imaging of the system to search for outer companions in the wide disk gap, allowing the detector to saturate out to near or beyond the companion's location. No additional candidates were found in either epoch.

5.1.2. PDS 70

We observed PDS 70 as part of the GAPlanetS campaign in 2017 and 2018. Hα emission from PDS 70 b from data taken in 2018 on two consecutive nights was reported in Wagner et al. (2018a), establishing PDS 70 b as an accreting protoplanet. Frame selection, highpass filter, and KLIP parameters were tuned aggressively to allow for robust recovery of the companion at ∼4σ in the combination of post-processed SDI imagery from the two 2018 nights. Hα line emission was subsequently resolved in both PDS 70 b and c by Haffert et al. (2019) with the Very Large Telescope (VLT) Multi Unit Spectroscopic Explorer (MUSE) instrument, and in ultraviolet accretion continuum emission with the Hubble Space Telescope (HST) by Zhou et al. (2021), lending additional credence to the original detection.

Figure 9 shows the continuum false planet optimized reductions for all three PDS 70 epochs, as well as the combination of the two 2018 nights. Overplotted on these images are the predicted locations of the two known companions at the epoch of observation, derived from the orbital fits of Wang et al. (2021b). Contrast curves for all PDS 70 epochs are shown in Figure 6. By optimizing on false continuum planets injected at a range of separations between the IWA and control radius of each data set, the GAPlanetS reduction framework is intentionally conservative. Both PDS 70 planets lie considerably outside the control radius; thus, the lack of recovery under the standard pipeline is unsurprising. While neither companions is robustly recovered, a ∼3σ excess signal appears within 1 FWHM of the predicted location of PDS 70 c in both Hα and ASDI images for the 2017 epoch and in ASDI images for the 2018 May 2 epoch.

Both known planets are recovered with more targeted optimization (see Figure 10). As the PDS 70 b and c companions exist at known locations and their bona fide planetary nature is

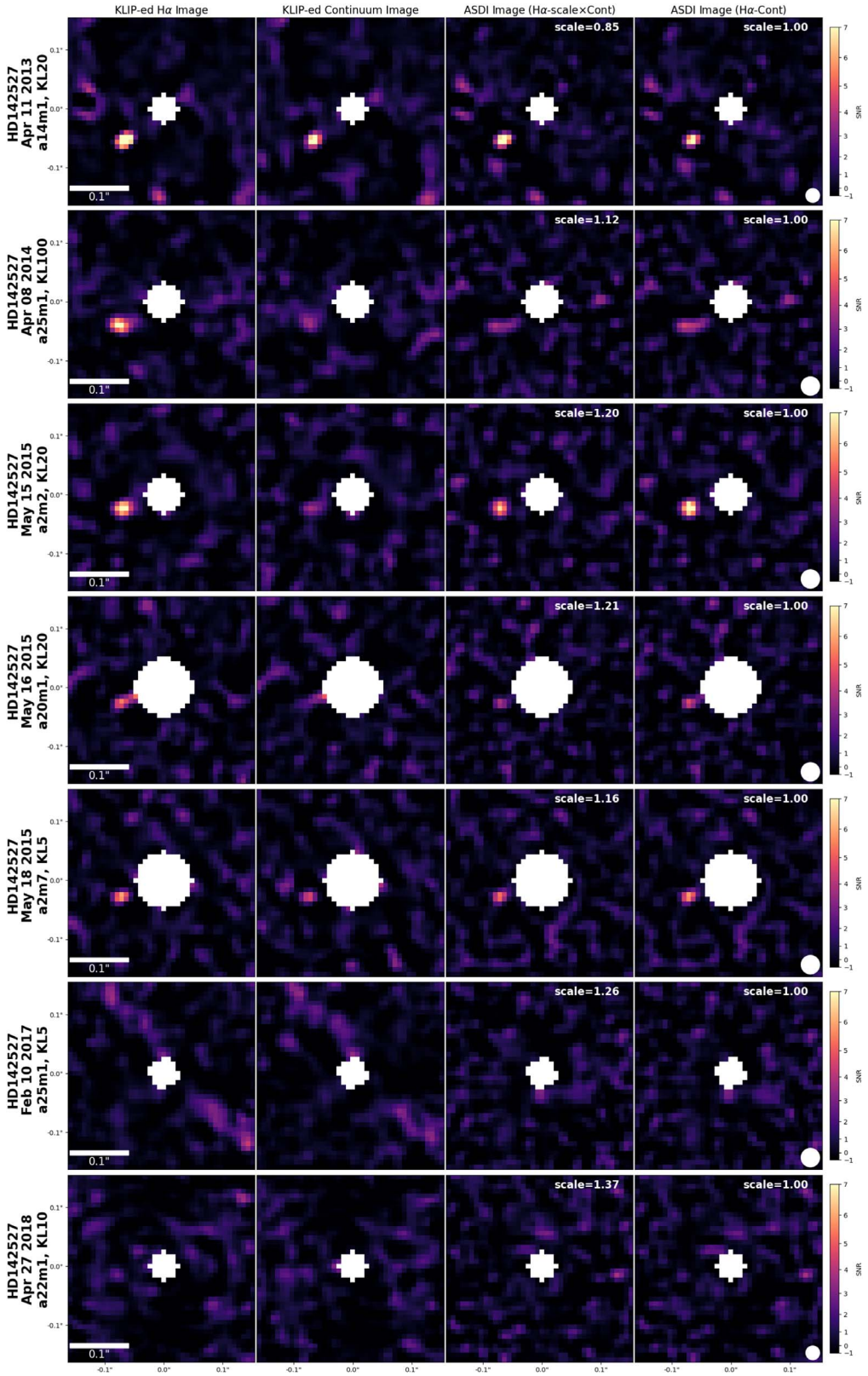

Figure 7. KLIP reductions of the H-alpha (left) and continuum (middle left) images for all HD 142527 epochs. KLIP parameters were optimized with `pyKLIP-PE` based on the recovered signal of false planets injected into the continuum images. The middle right panel shows a conservative SDI reduction created by multiplying the continuum KLIP image by the median Hα/continuum scale factor for the primary star (reported in table 2) and subtracting it from Hα imagery, which should effectively remove scattered light emission and continuum artifacts. The rightmost panel shows the unscaled Hα – continuum reduction, which is most appropriate in regions where no scattered light artifacts are present. The lack of a resolved inner disk component in HD 142527 makes scattered light from circumstellar material of minimal concern; however, there may be some contribution to these signals from a circumsecondary disk.

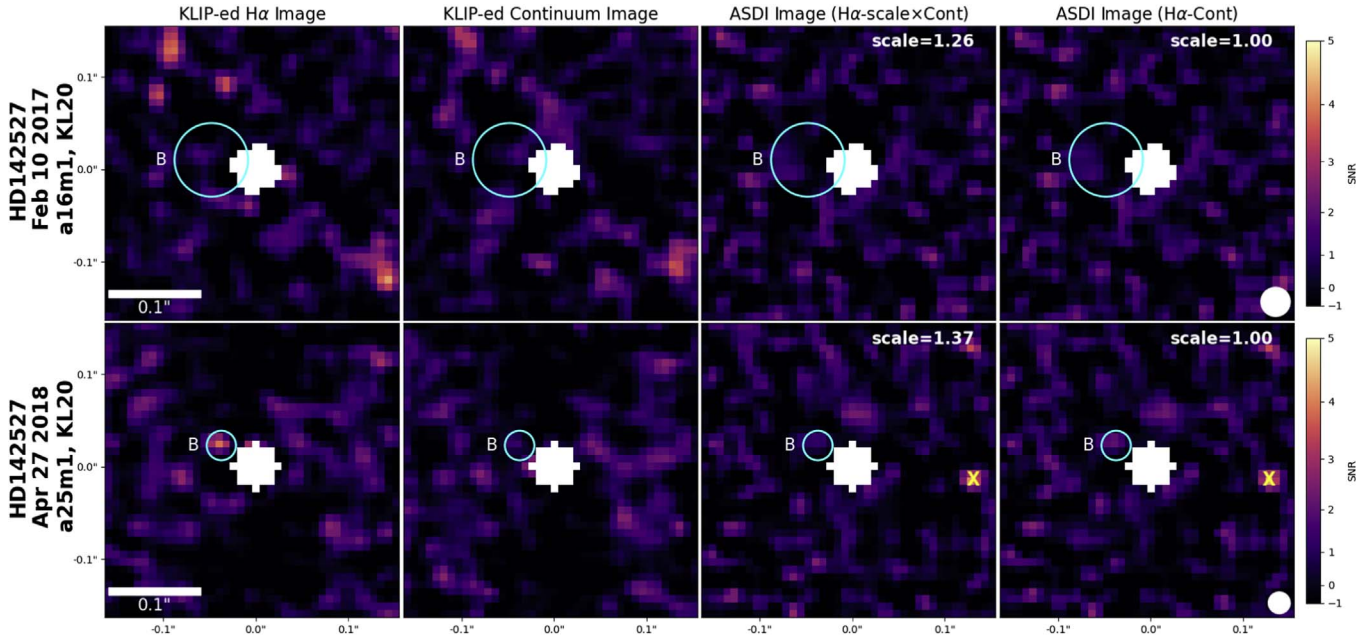

Figure 8. The same as Figure 7, except for the most difficult HD 142527 B detection epochs. Here, KLIP parameters have been optimized on the known location of the companion in the Hα images (cyan circle labeled "B"; Balmer et al. 2022), resulting in a recovery of the companion in the 2018 data, but nonrecovery in 2017. The yellow "x" marks a strong negative continuum speckle.

well established, we follow the same procedure as for the more difficult HD 142527 B recoveries in order to recover their signals where possible. Namely, we optimize directly on the average S/N metric at the known planet location(s) in the Hα images. We choose to average this S/N metric across both known planet locations in order to achieve a relatively conservative approach to this direct Hα optimization.

We note that this optimization is done using the Hα images only and not SDI images. Because of the prevalence of false point sources induced during subtraction of KLIP-ed continuum imagery, we believe that optimizing on the Hα images is a more robust approach.

Reductions tuned to maximize the average S/N metric across both planets in 20 KL mode Hα post-processed imagery are shown in Figure 10, with their optimized KLIP parameters given in the labels on the left-hand side of each subpanel. The companions are only readily visible in SDI imagery using this methodology, but both are marginally recovered. A signal consistent with PDS 70 c is present in all three SDI epochs, with classically computed S/Ns of [3.8, 2.6, and 2.9] and [3.1, 3.0, and 3.4] in 1:1 scaled and conservatively scaled SDI images, respectively. It is also marginally recovered in Hα at an S/N of 3.7 in the 2017 epoch. PDS 70 b is recovered only in the 2018 May 3 epoch at an S/N of 3.3 in 1:1 scaled SDI imagery and 2.8 in conservatively scaled SDI imagery.

We extract detailed astrometry and photometry only from the 2017 Hα detection of PDS 70 c, as forward model fitting of SDI imagery is more complex and beyond the scope of this work. We note, however, that the positions of the marginal detections of PDS 70 b and PDS 70 c in 2018 SDI imagery are entirely consistent with their `whereistheplanet` predicted orbital positions (see Figure 10), which incorporates the astrometry of Wagner et al. 2018a and other works.

Our 2017 detection of PDS 70 c extends the time baseline of its astrometry by 9 months. The companion is detected at a separation of 246.9 ± 4.4 mas and a PA of $284.2 \pm 0.^{\circ}6$. This is inconsistent at the $\sim 5\sigma$ level with the `whereistheplanet` (Wang et al. 2021a) prediction for the separation of the planet at this epoch (223.2 ± 0.9mas), though the PA prediction ($283.^{\circ}8 \pm 0.^{\circ}2$) is consistent . Our best-fit photometry suggests a Δmag of 5.5 ± 0.2 relative to the stellar continuum, brighter by nearly 2 mag than the 7.7 ± 0.2 reported from VLT MUSE observations taken a year later by Haffert et al. (2019). Possible sources of these discrepancies are discussed in Section 6.1.

5.1.3. LkCa 15 b

LkCa 15 was observed three times as part of the GAPlanetS campaign, in 2014, 2015, and 2016. The 2014 epoch is the original Hα discovery epoch for LkCa 15 "b", as well as the highest-contrast epoch (see Figure 6). The 2015 data were of very poor quality and were discarded before KLIP optimization due to a failure to recover injected planets at a contrast of 10^{-1}. The 2016 data set is of intermediate quality, though substantially poorer in contrast than the 2014 epoch, and the companion candidate is not recovered.

The existence of multiple protoplanet candidates in close proximity to the inner disk rim of LkCa 15 has been the source of some controversy. Recent work by Currie et al. (2019) resolved the inner disk component previously imaged by Thalmann et al. (2016) in polarized intensity, this time in NIR total intensity light with SCExAO on Subaru and in the thermal infrared with Keck/NIRC2. The authors interpret the smooth resolved inner disk rim as inconsistent with the existence of multiple protoplanets at similar separation; however, their results cannot explain observed orbital motion in the sparse aperture masking detections (Sallum et al. 2016), nor is an inner disk artifact consistent with the presence of Hα excess emission in the companion.

Mendigutía et al. (2018) attempted spectroastrometric detection of Hα emission from the LkCa 15 "b" planet candidate and reported symmetric extended Hα emission. However, their observation relied on long-slit spectroscopy that does not appear to have been well aligned with the predicted position of

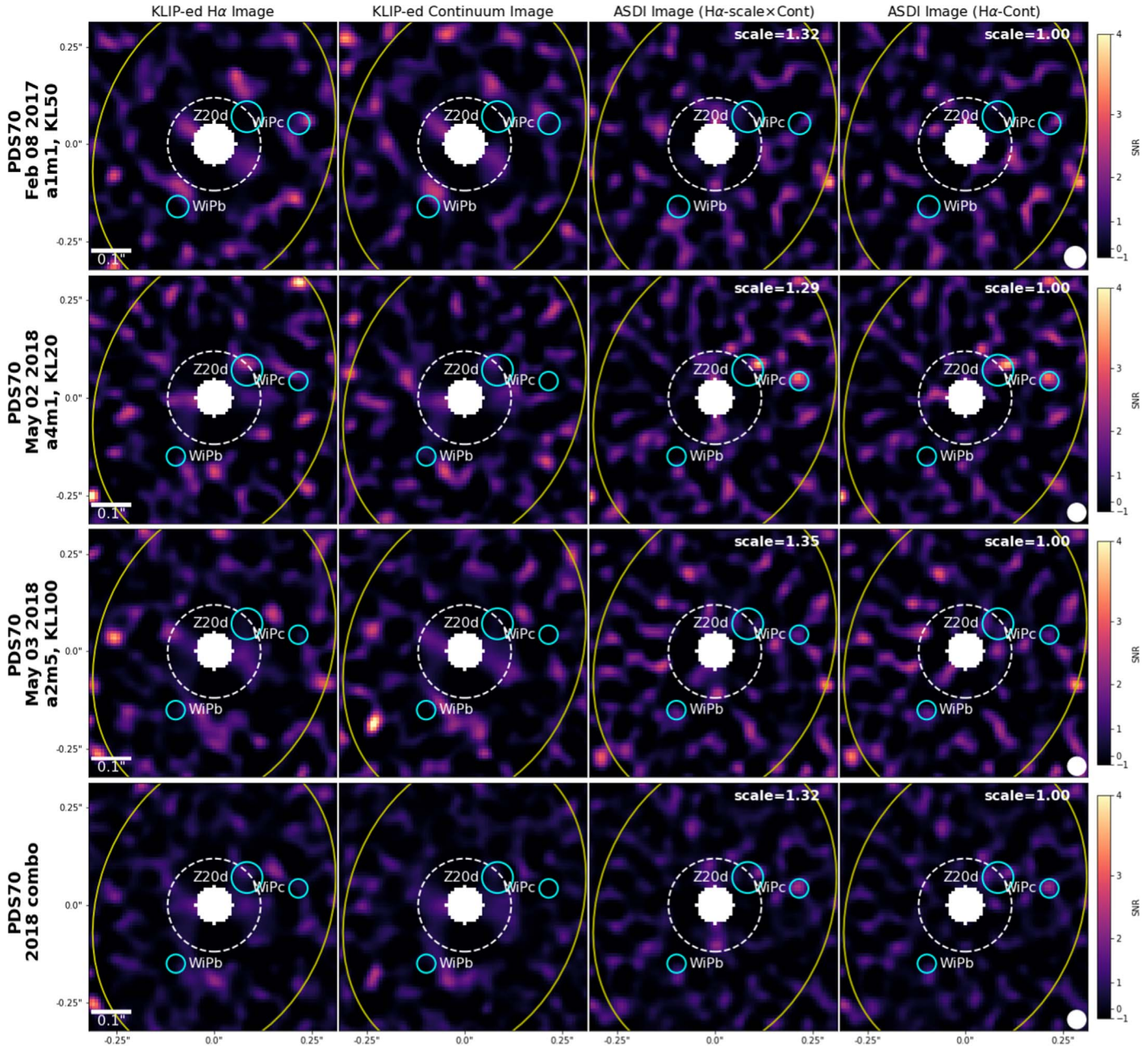

Figure 9. Post-processed GAPlanetS images for all PDS 70 epochs. KLIP parameters were optimized for false planets injected into the continuum channel, resulting in marginal (S/N $\sim$ 3) recoveries of PDS 70 c in 2017 and on 2018 May 2, but a nonrecovery of PDS 70 b in all epochs. The cyan "WiPb" and "WiPc" circles mark the predicted location of the planet at the precise epoch of our observations, computed using Wang et al. (2021a). The cyan circle labeled "Z20d" marks the location of a third point-source candidate from Zurlo et al. (2020). The yellow ellipse marks the inner edge of the known scattered light cavity in this system.

LkCa 15 "b" at that epoch. Even if the companion was in the slit, the reported detection threshold was a contrast of 5.5 mag at Hα, close enough to the Δmag of 5.2 ± 0.3 reported in Sallum et al. (2015) that even a small decrease in luminosity relative to the original 2014 November Hα detection epoch (as might be expected if accretion onto the companion is stochastic) would render the planet undetectable.

As the nature of the point-source candidates in the LkCa 15 disk has been debated and their proximity to the resolved inner disk rim firmly established, we adopt the most conservative approach in this work—optimizing on false continuum planets only. We also overplot an ellipse in Figure 11 at the edge of the imaged inner disk rim. While the LkCa 15 "c" and "d" candidates are coincident with the inner disk rim, the "b" candidate lies significantly inside of it and is less likely to be a scattered light artifact, though we note that disk signals at similar separation to planet candidates can influence extracted KL modes (Lawson et al. 2022), and further vetting of this candidate is warranted.

Because of the tight separations of the companion candidates, the comparatively large PSF (FWHM $\sim$6 pixels, 50 mas), and the limited space available inside of the AO control radius for bin 2 data ($r = 15$ pixels), we injected only one false planet inside the control radius (at a separation of 12 pixels/0.″10 and a PA of 0°) to optimize these data.

Using our conservative methodology, we recover the 2014 Hα excess signal first reported in Sallum et al. (2015) with a classically computed S/N of 5.0 in the Hα images, 4.9 in the

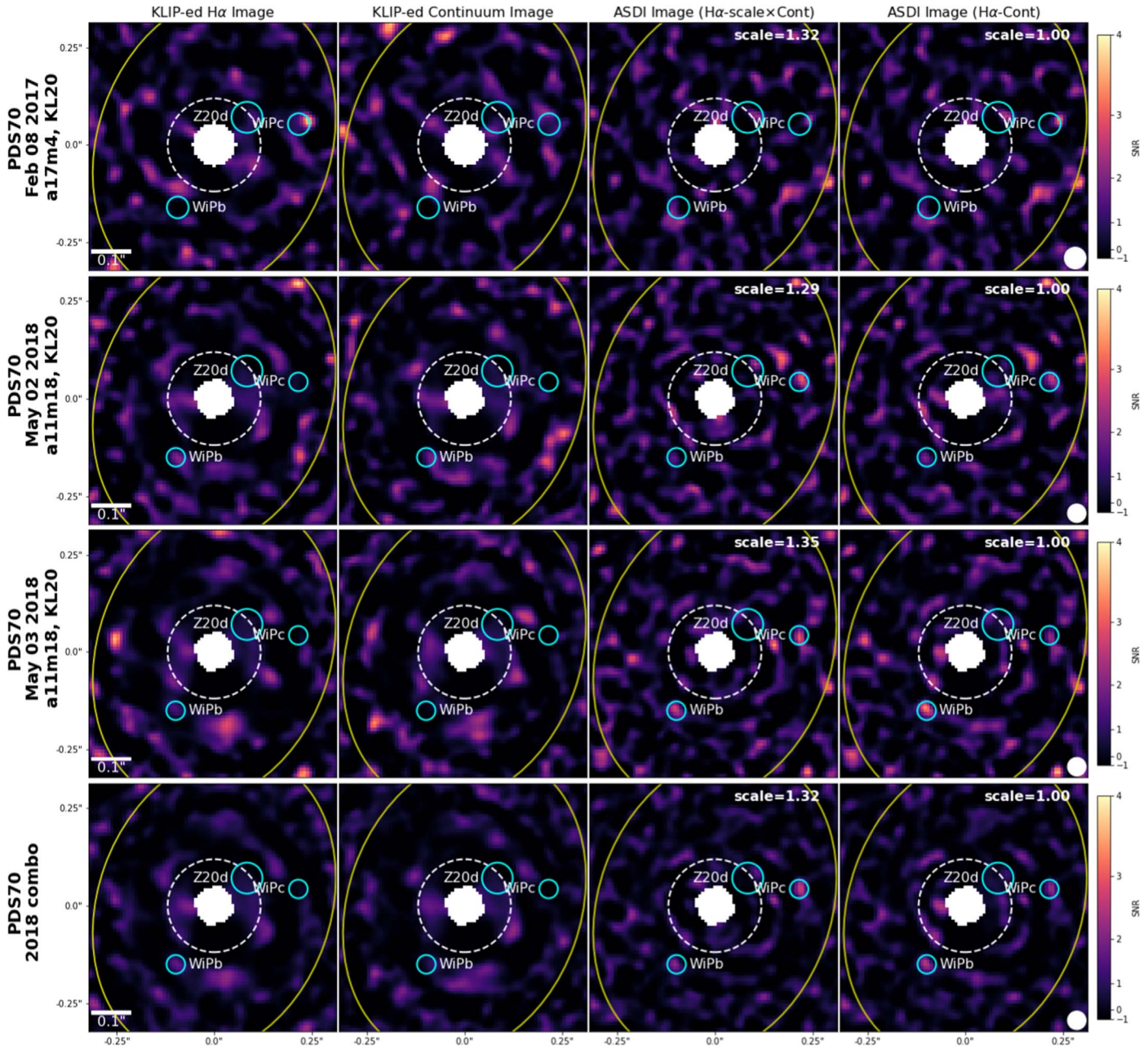

Figure 10. Post-processed GAPlanetS images for all PDS 70 epochs. KLIP parameters were optimized to maximize the average S/N metric at the locations of the PDS 70 b and c planets in Hα (left-hand panel). Although S/Ns are low at Hα, the parameters selected result in recovery of PDS 70 c in SDI imagery in all three epochs and recovery of PDS 70 b in the 2018 May 3 epoch. The cyan circle labeled "Z20d" marks the location of a third point-source candidate in this system from Zurlo et al. (2020). The cyan "WiPb" and "WiPc" circles mark the predicted location of the planet at the precise epoch of our observations, computed from Wang et al. (2021a). The yellow ellipse marks the inner edge of the known scattered light cavity in this system.

1:1 scaled Hα–continuum SDI reduction, and 2.9 in the conservatively scaled SDI reduction.

Best-fit BKA astrometry from the 2014 Hα epoch produces strong evidence ($Z_1/Z_0 = 18$) for a point source with a separation of 69.7 ± 6.1 mas, a PA of $242\overset{\circ}{.}6 \pm 2\overset{\circ}{.}7$, and a Δmag of 3.1 ± 0.3. This is inconsistent at the $\sim 1\sigma$–2σ level with the astrometry and photometry derived from the same data in Sallum et al. (2015), which placed the planet at a slightly wider separation (93 ± 8mas), higher PA ($256^\circ \pm 3^\circ$), and $\sim$1 magnitude fainter ($\Delta\mathrm{Mag} = 5.2 \pm 0.3$). This discrepancy is discussed in greater detail in Section 6.1.

While we recover a clear Hα signal in the 2014 epoch at the location of the previously reported LkCa 15 "b" planet candidate that is well fit by a point-source forward model, its nature remains ambiguous. The "b" candidate lies inside of the known scattered light inner disk rim, suggesting that it is not part of that structure. Although there is no apparent, comparable, point source in the continuum images, scaling them up by the stellar Hα-to-continuum ratio and subtracting it from Hα suppresses the signal heavily, meaning that it cannot be ruled out as a scattered light source. At the same time, a compact scattered light structure located inside the disk cavity would itself be a notable result.

The optimized 2016 SDI reductions appear to show a low-S/N ($\sim$2.5) arc of excess emission to the west of the star consistent with the known inner disk rim. The predicted location of

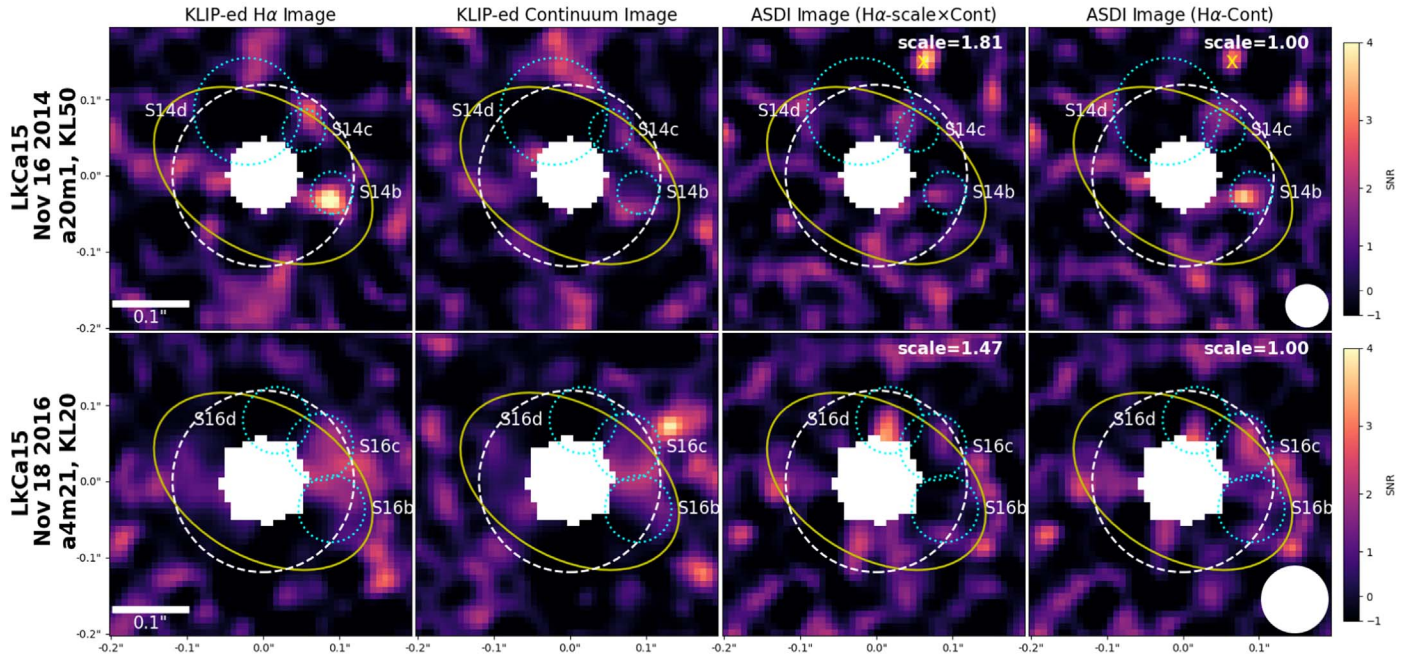

Figure 11. KLIP reductions of both LkCa 15 epochs, with parameters optimized by equally weighting all six post-processed image quality metrics across 5 and 20 KL modes for the single false planet injected into the continuum images inside of the control radius (at separation $= 0\farcs1$, PA $= 0$). The locations of candidate companions from the literature are indicated with cyan circles ("S14b," "S14c," "S14d," Sallum et al. 2015; "S16b," "S16c," "S16d," Sallum et al. 2016). The yellow "x" marks a strong negative speckle just outside the control radius in the continuum images, which appears bright in SDI imagery.

LkCa 15 "b" lies inside of this rim, but it is not recovered. The contrast of these data are a factor of 5 or more worse than the 2014 epoch at all separations, making the lack of recovery of the candidate unsurprising. The high `pyKLIP movement` value converged upon by the continuum false planet optimization equates to a small reference library for PSF subtraction, with a large degree of rotation between reference and target images. High rotational mask reductions are often used to resolve disk structures in ADI imagery, and this is likely the reason why the apparent disk rim is seen in 2016 but not 2014. Its appearance in SDI imagery is, however, surprising and could suggest an additional Hα emission source (i.e., the LkCa 15 "b" protoplanet) located to the west of the star, adding to the light being scattered by dust grains at this location.

There is also a $\sim 3\sigma$ excess signal in the 2016 images at the predicted location of the "d" protoplanet candidate; however, there is a comparable signal to the south opposite this feature, which is suggestive of a wavefront error (phase) induced speckle.

In summary, we reproduce here, with a systematic and robust pipeline designed to minimize false positives, the original LkCa 15 "b" Hα detection reported in Sallum et al. (2015). We do not, however, recover the LkCa 15 "c" or "d" protoplanetary candidates, though this does not rule them out as protoplanets, as our achieved contrasts are modest at best.

5.2. Objects with New Protoplanet Candidates

5.2.1. CS Cha

One epoch of GAPlanetS data was obtained for the CS Cha AaAb spectroscopic binary (unresolved, sep < 44 mas; Kurtovic et al. 2022) in 2015. Although we do not see evidence of the wide polarized companion CS Cha B in post-processed images of this epoch (see Section 5.3), we do find tentative evidence of a much more tightly separated point-source candidate with a classically computed S/N of 6.6 at Hα (`PlanetEvidence` S/N = 4.3) located at a separation of 68 mas and a PA of 76°, as seen in Figure 12.

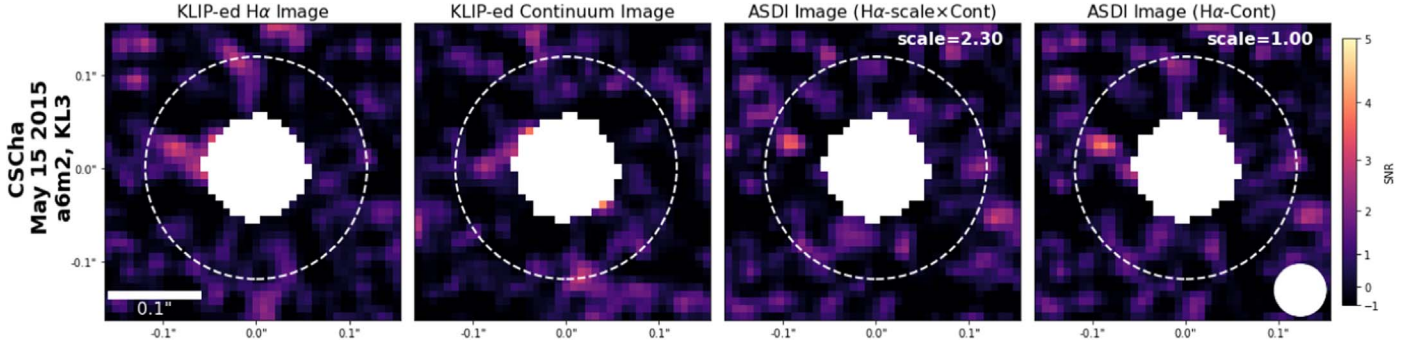

Figure 12. Final KLIPed Hα (left), Continuum (middle left), stellar Hα/continuum-scaled ASDI (middle right), and 1:1 scaled ASDI (right) imagery for the single GAPlanetS CS cha epoch. The new candidate companion, CS Cha "c" is apparent to the east of the star in Hα and SDI imagery.

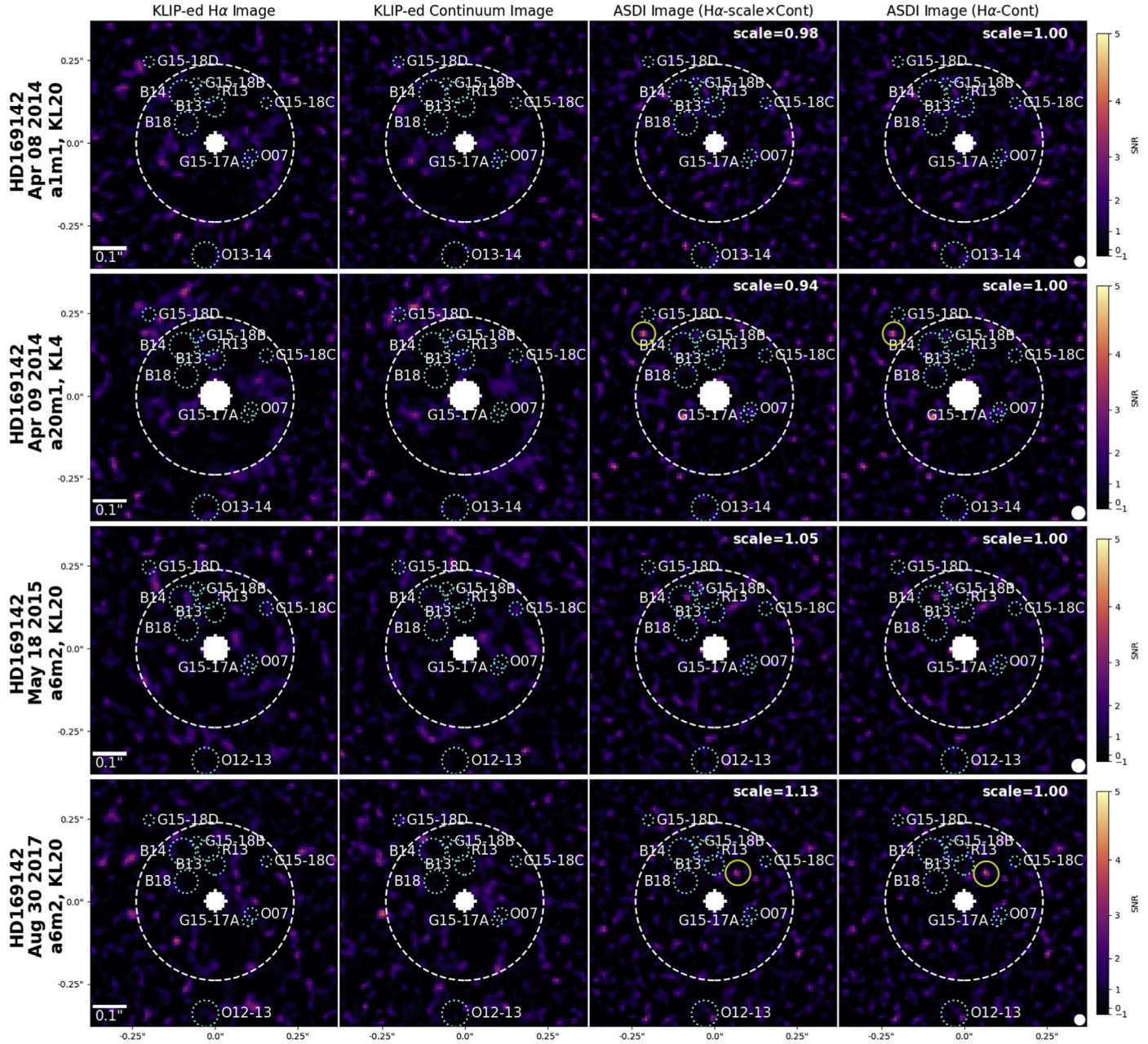

Figure 13. KLIPed Hα (left), Continuum (middle left), stellar Hα/continuum-scaled ASDI (middle right), and 1:1 scaled ASDI (right) imagery for all HD 169142 epochs. `pyKLIP` reduction parameters (indicated in the text labels to the left of each image panel) have been optimized for recovery of false continuum planets injected between the IWA and control radius, as described in detail in the text. The AO control radius of the images is indicated with a white dashed circle. The locations of candidate companions from previous work are indicated with dashed cyan circles at the literature detection epoch listed in Table 4 ("O07," Okamoto et al. 2017; "O12–13," Osorio et al. 2014; "R13," Reggiani et al. 2014; "B13" and "B14," Biller et al. 2014; "G15-17A," "G15-18B," "G15-18C," and "G15-18D," Gratton et al. 2019; "B18," Bertrang et al. 2020). Yellow "x" symbols indicate locations where apparent companions are introduced into SDI imagery through subtraction of a negative continuum speckle. The most compelling 3σ–4σ point-source candidates are indicated with yellow circles, though there are reasons to be skeptical of each, as detailed in the text.

The observed separation of this candidate is roughly twice the value of the spectroscopic binary CS Cha A's maximum predicted projected separation, suggesting that the imaged companion is not the other member of the binary. This detection places the candidate companion firmly within the disk's submillimeter continuum (<210 mas; Francis & van der Marel 2020) and scattered light (<92.5–337 mas; Ginski et al. 2018) cavities and interior to the probable inner edge of the gas cavity (CO temperature peak at 128 mas; Kurtovic et al. 2022). Simulations in Kurtovic et al. (2022) predict a Saturn-mass planet near the inner edge of the gas cavity, roughly consistent with the separation of the detected candidate. We note that their mass estimate is dependent on a viscosity assumption, and the presence of Hα emission may be suggestive of a more massive companion.

Its moderate contrast of 0.05 (3.2 mag) relative to the (spectroscopic binary) primary suggests that the CS Cha "c" candidate may be massive or accreting at a very high rate. When corrected to a contrast relative to the stellar continuum (rather than the actively accreting primary), the contrast is even more moderate—2.3 mag. However, lack of detection in

continuum imagery is more suggestive of a planetary nature. Due to these ambiguities and the lack of a second epoch, we refer to this detection as a protoplanet "candidate" throughout the remainder of this work.

5.3. Objects with Known Companions or Companion Candidates in the Literature

Six of the remaining transitional disks in the GAPlanetS sample have previous reports of planetary, brown dwarf, or stellar-mass companions from NIR high-contrast imagery, a submillimeter point source interpreted as evidence of a circumsecondary disk, or a so-called ALMA "velocity-kink" indicative of possible inflow onto an embedded planet (e.g., Rabago & Zhu 2021). In each case, the reported location of the planet candidate(s) at the literature detection epoch is given in Table 4 and shown in all KLIPed images of the system. True companions will in most cases have undergone some small amount of orbital motion since this original detection epoch.

Three of the companions—HD 100546, HD 169142, and SAO 206462—have previously reported planet candidates at low to moderate separation ($<0\farcs5$) from the central star. Hα, Continuum, and ASDI images for all epochs of HD 169142 are shown in Figure 13 in order to demonstrate the difficulty of assessing protoplanet candidates in highly morphologically complex systems, while the other two objects' reductions are shown in Appendix B. The contrast curves for all HD 100546, HD 169142, and SAO 206462 epochs are shown in Figure 14.

The remaining three objects—TW Hya, HD 100453, and CS Cha—have more distant ($>0\farcs5$) known or candidate companions, of which only HD 100435 B is recovered in GAPlanetS imagery. `PyKLIP` ASDI reductions for the highest-contrast epochs of these objects are shown in Figure 15. Optimized imagery of the inner regions of these three systems is shown in Appendix B. Contrast curves for all TW Hya, HD 100453, and CS Cha epochs are given in Figure 16.

5.3.1. HD 169142

GAPlanetS data of HD 169142 were collected on four nights—two consecutive nights in 2014, one night in 2015, and one night in 2017. All four epochs are shown in Figure 13. The data do not show a consistent excess at or near the location of any of the planet candidates across epochs; however, there are marginal signals consistent with Hα excess near the location of several candidates in single epochs. These signals do not rise to the level of candidates in our analysis because they are neither consistent across epochs nor have sufficiently high S/N. However, some may later prove to be true planetary signals in light of future observations at higher contrast.

We include all epochs of HD 169142 in the main body of the text as a demonstration of the difficulty of candidate identification in morphologically complex systems under variable conditions (and, potentially, intrinsic variability in protoplanet candidates' Hα emission). For example, one of the more apparently compelling candidates in the images is a $\sim$3.5σ point source just outside the control radius near the Gratton et al. (2019) "D" candidate in the 2014 April 9 epoch (marked with a yellow circle in Figure 13). The lack of similar signal in the higher-contrast 2014 April 8 epoch just 1 day earlier, as well as its proximity to the AO control radius (immediately outside of which a bright ring of variable signal induced by the wavefront control loop appears in raw images), means that it does not rise to the level of a candidate in our analysis. Another $\sim$4σ excess source appears to the northwest of the star in the 2017 August 30 epoch at similar separation as the Reggiani et al. (2014) and Biller et al. (2014) candidates (also indicated with a yellow circle in Figure 13). The 3 yr time baseline between the original candidate identification epochs and this observation may allow for this degree of orbital motion; however, there is not a compelling excess at the same location in the Hα imagery, and similarly strong excess is not seen near this location in the other epochs, so this candidate is also marginal. We conclude that it and the other candidates at similar separation are most likely scattered light features from a clumpy inner disk ring at this separation, consistent with their lack of recovery in SDI imagery.

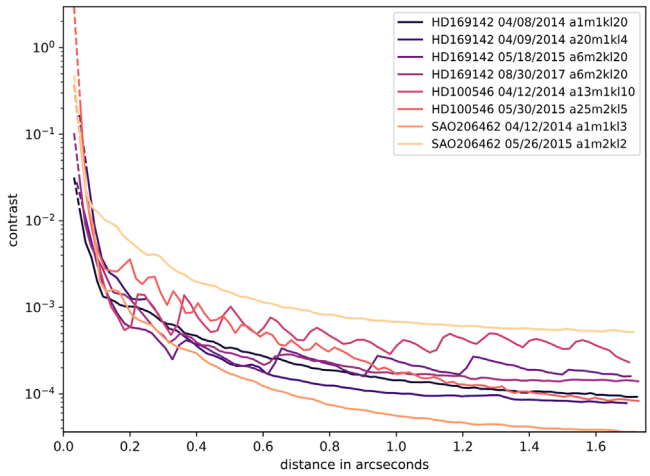

Figure 14. Throughput-corrected 5σ contrast curves of all epochs for continuum false planet optimized `pyKLIP` reductions of the three GAPlanetS targets with reported close ($<0\farcs5$) companion candidates in the literature: HD 100546 (two epochs), HD 169142 (four epochs) and SAO 206462 (two epochs). Throughput was computed as described in the text, with a correction for the small number of independent noise samples near the star following Mawet et al. (2014). Solid curves indicate regions where throughput-corrected contrast was computed directly. The curves are also projected inward from the innermost throughput measurement to the inner working angle, and this extrapolated region is indicated with a dashed line.

5.3.2. HD 100546

The GAPlanetS data for HD 100546 were analyzed in detail in Follette et al. (2017) and Rameau et al. (2017); however, we have taken advantage of improvements to the GAPlanetS pipeline since initial publication and reprocessed the data, allowing us to place more stringent limits on the Hα luminosity of the HD 100546 "b" and "c" planet candidates, as given in Table 6. No Hα excess signals were seen in the vicinity of either candidate in either GAPlanetS epoch (see Appendix B, Figure 20).

5.3.3. SAO 206462

GAPlanetS data were collected for SAO 206462 (HD 135344 B) in 2014 and 2015. No Hα excess signals were detected at or near the location of the Cugno et al. (2019) or Casassus et al. (2021) candidates in either epoch, and the best limit on the contrast at the location of these candidates is provided in Table 6. Images of both SAO 206462 epochs are shown in Appendix B, Figure 21.

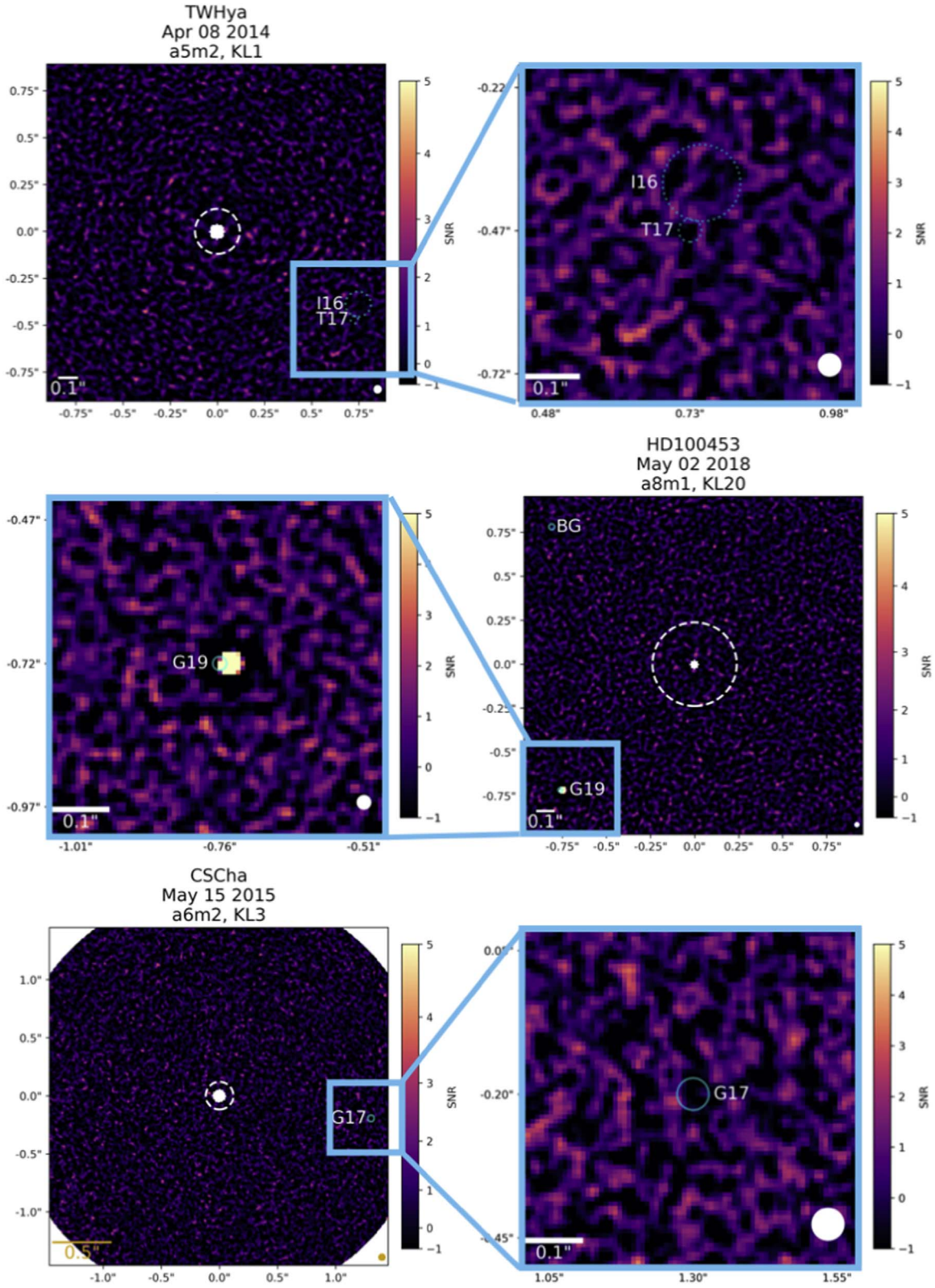

Figure 15. Wide-field and narrow-field views of the 1:1 scaled ASDI reduction from the highest-contrast epoch for all three GAPlanetS targets with known wide companions (CS Cha B, HD 100453 B) and companion candidates (TW Hya). No clear Hα excess signal is present at the location of the wide TW Hya candidate(s) reported in Ilee et al. (2022; "I16") or Tsukagoshi et al. (2019; "T17"), nor is it apparent from the known, highly embedded CS Cha B companion ("G17," Ginski et al. 2018). Hα excess is, however, apparent from the HD 100453 B companion at a location consistent with its reported position in 2019 (Gonzalez et al. 2020; "G19").

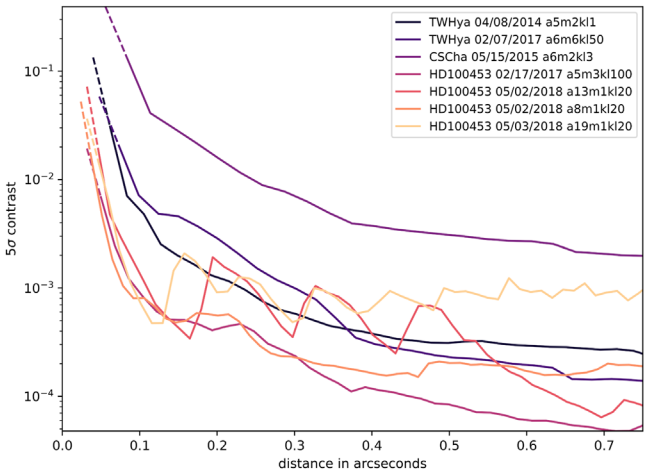

Figure 16. Throughput-corrected 5σ contrast curves for continuum false planet optimized `pyKLIP` reductions of all epochs for the three GAPlanetS targets with reported wide (>0.″5) companions or companion candidates in the literature: TW Hya (two epochs), CS Cha (one epoch), and HD 100453 (three epochs). Throughput was computed as described in the text, with a correction for the small number of independent noise samples present near the star implemented following Mawet et al. (2014). Solid curves indicate regions where throughput-corrected contrast was computed directly. The curves are also projected inward from the innermost throughput measurement to the inner working angle, and this extrapolation region is indicated with a dashed line.

5.3.4. TW Hya

GAPlanetS data of TW Hya were collected in 2014 and 2017. The highest-contrast (2014) ASDI epoch is shown in a wide-angle view in Figure 15, together with a zoomed-in view of the region surrounding the location of the candidate previously reported by Tsukagoshi et al. (2019) and Ilee et al. (2022). We note that TW Hya is accreting at an enormously high rate compared to the other objects in the sample, and the primary star is 6–8 times brighter at Hα than at the continuum in both epochs. This makes the difference between the 1:1 scaled SDI and the conservatively scaled SDI images striking and is an extreme example of the possible impact of incompletely removed stellar residuals on 1:1 scaled SDI images. At the same time, it is a clear demonstration of the power of measuring the stellar Hα/continuum ratio and scaling continuum imagery by it prior to SDI subtraction, as the residuals are very effectively removed in the conservatively scaled reduction shown in Figure 22. We do not find any evidence of Hα excess signals at the locations of the Tsukagoshi et al. (2019) or Huélamo et al. (2022) point-source candidates, nor elsewhere in the disk; however, both epochs are shown in Appendix B, Figure 22.

5.3.5. HD 100453

GAPlanetS data were collected for HD 100453 on one night in 2017 and two nights in 2018. The outer M dwarf companion HD 100453 B and a previously known background star at similar separation to the northeast are easily resolved, as seen in Figure 15. No additional point-source candidates are apparent in the imagery, including in the combination of the two 2018 data sets. A gallery of all HD 100453 epochs is shown in Appendix B, Figure 23.

HD 100453 B is a wide M star companion, robustly recovered in both Hα and Continuum imagery in all GAPlanetS epochs, though it is saturated in all but the 2018 May 2 short exposure data set. For this reason, we extract astrometry and photometry from the companion only at this epoch, and these values are given in Table 5. As the M dwarf companion is well characterized (Collins et al. 2009; Wagner et al. 2018b), we do not examine it in detail in this work.

HD 100453 B exhibits Hα excess, a clear indication of ongoing accretion, and an estimate for its accretion rate is given in Table 5. In contrast, the known background star to the northeast of the primary star is fully removed via ASDI except in the case of the deepest data set, when some excess remains because the background star is saturated (see Appendix B, Figure 23).

5.4. Objects without Companion Candidates in the Literature

There are a number of GAPlanetS targets for which there are no previous reports of planet candidates at detectable separations (though there is a report of a very close companion to V1247 Ori, indicated in the images but under the inner mask), and there are no specific morphology-based predictions for protoplanet locations. These systems are HD 141569, PDS 66, UX Tau A, V1247 Ori, and V4046 Sgr. No compelling point sources are detected in any of the epochs for these objects, though KLIP-ADI and ASDI images are shown for all epochs in Appendix B. Contrast curves for all epochs are given in Figure 17.

6. Survey Results

6.1. Overview of Companion and Companion Candidate Photometry and Astrometry

In this section, we summarize our recovery of each of the five GAPlanetS companions and companion candidates. In all cases where the candidate recovery is sufficiently robust in Hα and/or continuum imagery, we extract astrometry and photometry using BKA as described in Section 5, and report the best-fit values in Table 5.

Figure 18 shows Bayesian KLIP astrometry models for all GAPlanetS point-source detections except for HD 142527 B, whose BKA fits we recompute under the unified GAPlanetS framework and report in Table 5, but which are similar to those described in detail in Balmer et al. (2022). Each image panel shows a stamp of the final optimized post-processed image, the corresponding best-fit forward model, and the residuals.

Our BKA fits returned "strong" evidence ratios for all five companions/candidates reported in Section 6. For PDS 70 c, LkCa 15 "b," and CS Cha "c," no point source is recovered in the continuum, lending credence to the assertion of a planetary nature. HD 142527 B and HD 100453 B are recovered robustly in both Hα and continuum imagery, consistent with their nature as stellar companions. In both cases, planet-to-star contrast is more moderate at Hα than in the continuum for all epochs, suggestive of active accretion.

Compared to past observations, we find:

1. HD 142527 B's astrometry is entirely consistent with the observed position of the companion at similar epochs from other facilities, as discussed in detail in Balmer et al. (2022). We consider this excellent validation of our instrumental astrometric solution for VisAO.
2. Although we have conducted HD 142527 reductions under a more conservative KLIP optimization framework, all astrometry is consistent with Balmer et al.

Table 6
Limits on Undetected Protoplanet Candidates

Object	Candidate Label	Separation (mas)	PA (deg)	Observation Epoch(s)	Source	GAPlanetS Best Epoch	Log Contrast At Planet	Δmag
HD 169142	O07	116 ± 20	250 ± 5	Jun-07	Okamoto et al. (2017)	8-Apr-14	−3.85	>9.6
HD 169142	O12-13	340	175.0	2012–2013	Osorio et al. (2014)	8-Apr-14	−4.17	>10.4
HD 169142	R13	156 ± 32	7.4 ± 11.3	Jun-13	Reggiani et al. (2014)	8-Apr-14	−3.95	>9.9
HD 169142	B13	110 ± 30	0 ± 14	Jul-13	Biller et al. (2014)	8-Apr-14	−3.78	>9.5
HD 169142	B14	180	33.0	Apr-14	Biller et al. (2014)	8-Apr-14	−3.99	>10.0
HD 169142	G15-17A	115 ± 15	239 ± 11.5	2015–2018	Gratton et al. (2019)	8-Apr-14	−3.84	>9.6
HD 169142	G15-18B	189 ± 8	17 ± 8	2015–2018	Gratton et al. (2019)	8-Apr-14	−3.99	>10.0
HD 169142	G15-18C	197 ± 8.5	308 ± 9	2015–2018	Gratton et al. (2019)	8-Apr-14	−3.99	>10.0
HD 169142	G15-18D	317 ± 7	39 ± 5	2015–2018	Gratton et al. (2019)	8-Apr-14	−4.15	>10.4
HD 169142	B18	105.8 ± 35.3	55.5 ± 4.0	15-Jul-18	Bertrang et al. (2020)	8-Apr-14	−3.75	>9.4
HD 100546	Q11	480 ± 40	8.9 ± 0.9	May-11	Quanz et al. (2013)	12-Apr-14	−4.97	>12.0
HD 100546	C15	131 ± 9	150.9 ± 2	Jan-15	Currie et al. (2015)	12-Apr-14	−3.79	>9.1
HD 100546	S15-16	455 ± 7	11.5 ± 1	2015–2016	Sissa et al. (2018)	12-Apr-14	−4.91	>11.9
HD 100546	F15-16	964.0	10	2015–2016	Fedele et al. (2021)	12-Apr-14	−5.30	>12.9
HD 100453	G19	1074.0 ± 31.8	132.7 ± 0.8	Apr-19	Gonzalez et al. (2020)	2-May-18-long	−4.76	>11.6
V1247Ori	W12-13d	41.5 ± 6.5	305.5 ± 5.5	2012–2013	Willson et al. (2019)	11-Dec-15	−1.94	>4.7
SAO206462	C16	71.1 ± 5	19 ± 3	Mar-16	Cugno et al. (2019)	12-Apr-14	−3.06	>7.4
SAO206462	C19	425.9 ± 1.2	212.4 ± 0.7	Jul-19	Casassus et al. (2021)	12-Apr-14	−4.54	> 11.1
CSCha B	G17	1316.5 ± 5	261.4 ± 0.2	Feb-Jun 2017	Ginski et al. (2018)	15-May-15	−3.18	>7.1
TW Hya	I16	840.7 ± 67.2	242.5 ± 2.1	Dec 2016	Ilee et al. (2022)	7-Feb-17	−4.14	>8.2
TW Hya	T17	865.4 ± 1	237 ± 1	May-17	Tsukagoshi et al. (2019)	7-Feb-17	−4.15	>8.2
TW Hya	H19	160 ± 10	190 ± 1	15-Mar-19	Huélamo et al. (2022)	7-Feb-17	−3.11	>5.6
PDS 70	Z20d	110	310	Feb-July 2020	Zhou et al. (2021)	2-May-18	−2.64	>6.3

Note. Limits for planet candidate nondetections. The "Candidate Label" column indicates the text marking the candidate in our figures. Separation and PA, as well as the errors on these quantities, are derived from the original detection papers, with separations translated to pixels using the VisAO plate scale of 7.95 mas pixel^{-1} (Balmer et al. 2022). The "Observation Epoch" column indicates the date of the original observations used to identify the candidate(s), and the reference that reported it appears in the "Source" column. The GAPlanetS epoch with the highest achieved contrast at the candidate's separation is indicated in the "GAPlanetS Best Epoch" column, and the logarithm of the achieved contrast at the candidate separation in this epoch is indicated in the "Log contrast at planet" column. This is translated to a limiting Hα magnitude relative to the stellar continuum by multiplying achieved contrast by the stellar Hα-to-Continuum scale factor, as described in detail in the text.

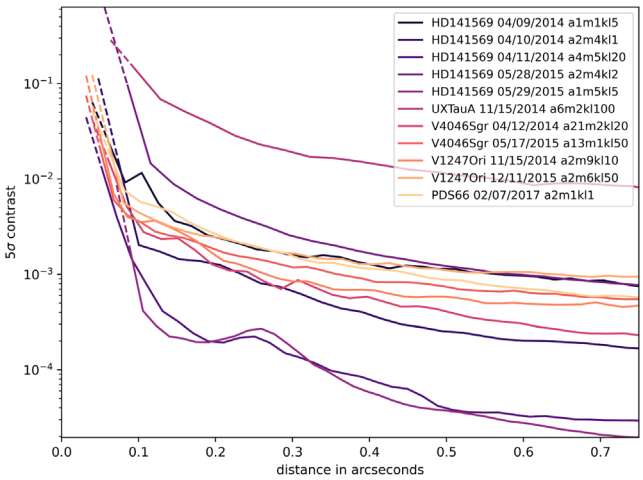

Figure 17. Throughput-corrected 5σ contrast curves for continuum false planet optimized `pyKLIP` reductions of all epochs for the four GAPlanetS targets without reported companion candidates in the literature: HD 141569 (five epochs), UX Tau A (one epoch), V4046 Sgr (two epochs), V1247 Ori (two epochs), and PDS 66 (one epoch). Throughput was computed as described in the text, with a correction for the small number of independent noise samples present near the star implemented following Mawet et al. (2014). Solid curves indicate regions where throughput-corrected contrast was computed directly. The curves are also projected inward from the innermost throughput measurement to the inner working angle, and this extrapolation region is indicated with a dashed line.

(2022) to within error bars except for two of the three continuum epochs, where the companion is recovered at $S/N < 3$ (2014 April 8 and 2015 May 15 astrometry disagrees with Balmer et al. 2022 at the 2σ level). This suggests that BKA fitting is relatively robust to the choice of KLIP parameters, except in cases where S/N is very low.

3. Measurement of the HD 142527 B companion's continuum Δmag is consistent epoch-to-epoch to within error bars. It is also consistent with the continuum Δmag measured by SPHERE ZIMPOL (Cugno et al. 2019). This suggests that our photometric extractions for GAPlanetS data are broadly consistent with other HCI instruments.
4. Measurement of HD 142527 B's Hα Δmag is lower than the Continuum Δmag at all epochs, with an average brightness increase of 0.9 mag over the continuum, suggestive of ongoing accretion. Our measurements are consistent with the observed Hα Δmag of Cugno et al. (2019) and with one another to within error bars. This is in conflict with the tentative evidence for accretion variability reported in Balmer et al. (2022), likely as a result of improved photometric extraction procedures described in detail in Section 6.2.
5. PDS 70 c is detected at the same PA as predicted by `whereistheplanet` in 2017, but at a significantly ($\sim 5\sigma$) wider separation. As our astrometric solution has been extensively validated with astrometry of Trapezium cluster members and HD 142527 B, this offset is likely accurate, and the orbital properties of PDS 70 c should be updated.
6. PDS 70 c's best-fit Hα contrast translates to it being nearly 2 mag brighter relative to the host star in the 2017 epoch than the estimate of Haffert et al. (2019). Accretion rate variability for young stars is estimated to be on the order of $\sim$0.5 dex (Hartmann et al. 2016), a factor of 2 smaller than the magnitude differential between our observations and Haffert et al. (2019).
7. LkCa 15 "b"'s astrometry and photometry is marginally ($\sim 1\sigma$–2σ) inconsistent with the values reported for the same data set in Sallum et al. (2015), appearing at a tighter separation and lower PA. Improvements in the centering algorithm, VisAO astrometric solution, and post-processing techniques likely contribute to the observed astrometric offset of LkCa 15 "b" relative to previous estimates, as does the smaller IWA.

While our characterization of HD 142527 B is consistent with existing literature, for PDS 70 c and LkCa 15 "b," our measurements of astrometry and photometry present inconsistencies with literature values. There are several possible reasons for this. Perhaps the most likely is that the extracted photometry and astrometry of companions, like many other qualities of post-processed images, are dependent on the choice of pre- (e.g., data quality cut, highpass filter value) and post- (e.g., IWA, `annuli`, and `movement`) processing parameters. Based on comparison of our BKA fits of HD 142527 B with those of Balmer et al. (2022) for the same data sets but with different pre- and post-processing choices, we believe that extracted astrometry of high-S/N ($S/N > 3$) sources is relatively robust to algorithmic parameters. Photometry, however, appears to be somewhat more sensitive to choices such as the BKA fitting area, especially as they effect the structure of the residuals, to which the photometry is very sensitive.[14] Importantly, uncertainty of this nature is not captured in our error estimates.

Absolute and relative photometric calibration of post-processed high-contrast images is also notoriously difficult. Though we have validated our photometric extractions relative to published photometry of HD 142527 B and attempted to rigorously quantify photometric uncertainties (see Section 6.2), systematic errors remain possible.

6.2. Determination of Accretion Rates and Limits

BKA-derived photometric contrasts for detected companions and final post-processed contrast limits for nondetected companion candidates from the literature are translated to accretion rates following the procedure described in this section. They appear with uncertainties in Tables 5 and 6.

6.2.1. Computation of Hα Line Luminosities

In previous work (e.g., Close et al. 2014; Sallum et al. 2015; Wagner et al. 2015b; Follette et al. 2017; Rameau et al. 2017), Hα line luminosities ($L_{H\alpha}$) and limits on this quantity have been computed following the equation:

$$L_{H\alpha} = 4\pi d^2 \, z \, \Delta\lambda \, 10^{(M_{H\alpha,*}+\Delta H\alpha)/-2.5} \quad (1)$$

where d is the distance in centimeters, z is the instrumental zero-point of the Hα filter (1.733×10^{-5} erg cm^{-2} s^{-1} μm^{-1} as determined by Males 2013), $\Delta\lambda$ is the width of the Hα narrowband filter (0.006 μm), $M_{H\alpha,*}$ is the star's extinction

[14] At the same time, we note that extraction of PDS 70 c astrometry and photometry in both continuum false planet optimized extractions (`annuli` = 1, `movement` = 1, `numbasis` = 50) and direct Hα optimized extractions (`annuli` = 17, `movement` = 4, `numbasis` = 20) is consistent within error bars despite extreme variation in KLIP parameters.

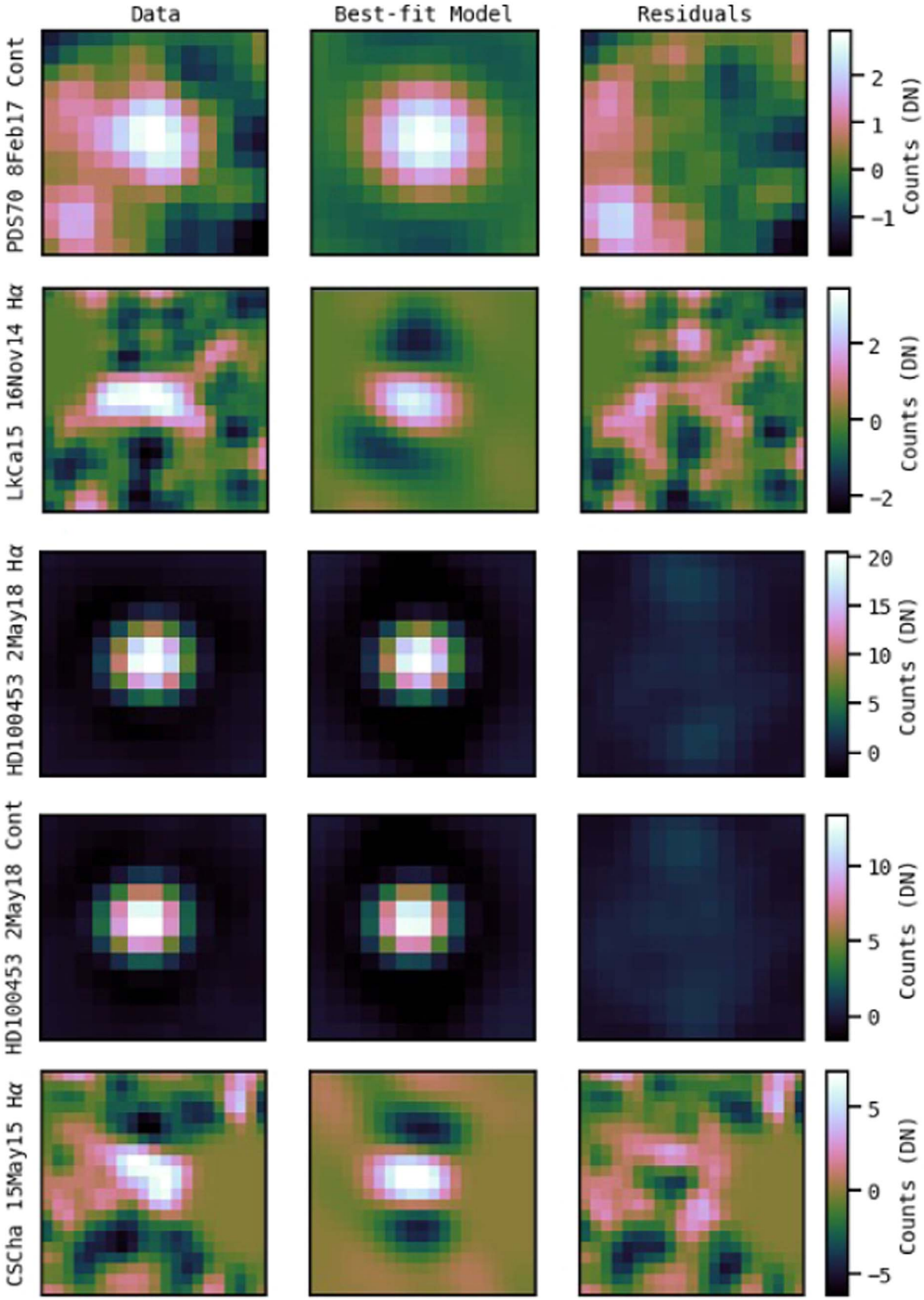

Figure 18. KLIPed data (left) compared to best-fit BKA forward models (middle),) and the residuals of their subtraction (right). Fits are shown for all companions whose photometry and astrometry could be extracted from Hα and/or Continuum GAPlanetS imagery, except for HD 142527 B, as qualitatively and quantitatively similarfits to the same data are shown in Balmer et al. 2022. Fit statistics are reported in Table 5.

corrected *continuum* magnitude in the Hα bandpass, and ΔHα is the difference between the star and companion brightness at Hα in magnitude units (computed as $-2.5\log_{10}$(contrast)).

As the stellar continuum magnitude at Hα utilized in Equation (1) is not known, we use the apparent magnitude at the Sloan Digital Sky Survey (SDSS) *r*' band as a proxy. We note that the *r*' band is both centered near Hα (making the effect of any continuum slope across the bandpass minimal) and ~25 times wider than the narrowband Hα filter width (making the contribution of any stellar Hα emission small compared to the overall *r*' band flux). To achieve uniformity in the *r*'-band apparent magnitude estimates for our targets, we convert Gaia DR3 G, G_{BP}, and G_{RP} photometry (Gaia Collaboration et al. 2022a) to SDSS *r*'-magnitudes following the best-fit conversions of Alam et al. (2015). We note that these values are consistent with the values of the Gaia Synthetic Photometry Catalog (GPSC; European Space Agency & DPAC Consortium 2022; Gaia Collaboration et al. 2022b) to within 0.1 mag for all eight GAPlanetS targets that are also in the GPSC.

r'-band photometry is subject to nonnegligible extinction in nearby star-forming regions, and this effect should be compensated for in estimating "true" *r*'-band apparent magnitudes for young stars. We estimate line-of-sight extinction to each GAPlanetS target by computing $E(\mathrm{BP}-\mathrm{RP}) = (\mathrm{BP}-\mathrm{RP})_{obs} - (\mathrm{BP}-\mathrm{RP})_0$, where $(\mathrm{BP\text{-}RP})_{obs}$ is the observed Gaia BP-RP color of each system, and $(\mathrm{BP\text{-}RP})_0$ is the intrinsic color derived from an update to Pecaut & Mamajek (2013) [15] for a pre-main-sequence star of the same spectral type, assuming the spectral types reported in Table 1. *E*(BP-RP) values have been shown to closely approximate literature *E(B−V)* values (within 0.2 mag; Andrae et al. 2018); therefore, we convert *E*(BP-RP) to an *r*'-band extinction following standard Milky Way extinction laws ($R_V = 3.1$, $A_{r'}/A_V = 0.758$). We list our $A_{r'}$ estimates, which are subtracted from the derived *r*'-band apparent magnitudes to compute a non-extincted r' magnitude estimate, in Table 1. We note that this estimate is based on stellar photometry alone, and that additional extinction toward companion candidates as a result of intervening circumstellar material is possible.

In this work, we also implement two minor corrections to the calculation described in Equation (1) for estimating $L_{H\alpha}$. First, because the central stars of our targets are themselves still actively accreting, the measured $\Delta H\alpha$ between the companion and the star is not really a Δ magnitude relative to the stellar *continuum*. To make it so, we multiply the measured contrast ($L_{H\alpha,comp}/L_{H\alpha,*}$) by the stellar H$\alpha$-to-continuum scale factor ($L_{H\alpha,*}/L_{Cont,*}$, determined with aperture photometry as described in Section 2.3 and reported in Table 2) to compute the companion's Hα brightness ratio relative to the stellar *continuum*($L_{H\alpha,comp}/L_{Cont,*}$). This value is reported in Tables 5 and 6 as Δmag. Due to the scale factor correction, it is not a direct magnitude conversion of the observed star-to-companion contrast, but rather a best estimate of the Hα excess *unique to the companion*.

$L_{H\alpha}$ is also, properly, a *line* luminosity, meaning the companion's continuum luminosity should be removed from the estimated Hα luminosity before using the derived value as a *line* luminosity. In the case where we detect continuum emission from the companion (HD 142527 B and HD 100453 B), this is easily done by substituting $\Delta Cont$ for $\Delta H\alpha$ into Equation (1) and subtracting the resulting continuum luminosity. In the case where an object is not detected at continuum wavelengths (PDS 70 c, LkCa 15 "b," and CS Cha "c"), the contribution of the object photosphere to the Hα luminosity is unknown. However, we note that the predicted absolute continuum *r*'-band magnitude of even a very massive, very young planet is extremely faint (*r*' = 14 for a 10M_J planet at 1 Myr; Baraffe et al. 2015) compared to the Hα absolute magnitudes that we estimate for our planetary companions and companion candidates ($M_{H\alpha}$ of 7.3, 8.8, and 12.3 for CS Cha "c," LkCa 15 "b," and PDS 70 c, respectively). It is thus reasonable to assume that any continuum contribution to the observed Hα luminosity for lower-mass companions is negligible.

In practice, these corrections and approximations make the equation used to compute Hα line luminosity:

$$L_{H\alpha} = 4\pi d^2 z \Delta\lambda 10^{(m_{r',*} - A_{r',*} - 2.5\log(\mathrm{CS}))/-2.5} - L_{cont}, \quad (2)$$

where $m_{r',*}$ is the stellar *r*'-band apparent magnitude, $A_{r',*}$ is the estimated *r*'-band extinction, C is the observed Hα contrast of the companion, S is the stellar Hα-to-Continuum scale factor, and L_{cont} is the continuum contribution to the Hα luminosity (used only in the case of a continuum detection of the companion, otherwise assumed negligible).

As BKA does not natively propagate absolute photometric uncertainties, we compute our own uncertainty estimates for the final companion Δmag by propagating the uncertainties on a number of individual quantities into magnitude space. These uncertainties are: the 67% credibility interval on the best-fit scale factor (the "alpha" value) from the BKA MCMC, uncertainty in the stellar Hα-to-continuum scale factor (estimated as the standard deviation in the scale factors of individual images in each observing sequence), and uncertainty in the stellar peak used to normalize imagery prior to BKA (estimated as the median photon noise of the best-fit stellar (unsaturated) or ghost (saturated) photometry). We also include uncertainty in the ghost-to-star scale factor in the case of saturated data, a value derived from the standard deviation of the residuals to the linear fit between ghost and stellar Moffat fit peak values in all unsaturated GAPlanetS data sets (230 ± 50 at Hα, 245 ± 50 at the Continuum).

Uncertainty on the final Hα luminosities encompasses uncertainty on Δmag, as well as uncertainties in the following quantities: the stellar *r*'-band apparent magnitude (assumed to be 0.1 based on the average discrepancy between our estimates and the GPSC), the *r*'-band extinction (estimated at ± 0.2 based on the range of estimates for A_R of these objects in the literature), distance (derived from parallax uncertainty in the Gaia catalog), instrumental zero-point (estimated conservatively at 10%), and the companion's continuum brightness (where detected, estimated following the same procedure as Hα photometric uncertainty).

6.2.2. Estimation of Accretion Luminosities and Rates

Accretion luminosities are derived from Hα line luminosities following the equation:

$$L_{acc} = 10^{b + a\log_{10}(\frac{L_{H\alpha}}{L_\odot})} L_\odot \quad (3)$$

where the coefficients *a* and *b* represent an empirically or model-derived scaling law between $L_{H\alpha}$ and accretion luminosity. The value of these scaling coefficients is

[15] Available at https://www.pas.rochester.edu/~emamajek/EEM_dwarf_UBVIJHK_colors_Teff.txt

particularly poorly constrained in the substellar regime. We report accretion rates for detected protoplanetary candidates and accretion rate limits for undetected literature companion candidates following both the Aoyama et al. (2021; $b = 1.61 \pm 0.04$, $a = 0.95 \pm 0.006$, with scatter of 0.3 dex) and Alcalá et al. (2017; $b = 1.74 \pm 0.19$, $a = 1.13 \pm 0.05$, with scatter of 0.5–0.7 dex) scaling relations. The Aoyama relation is theoretically derived from planetary accretion shock models (e.g., Aoyama et al. 2018; Marleau et al. 2019), where the principal difference relative to classical magnetospheric accretion models is the contribution of the (non–fully ionized) postshock region to the line emission. The Alcalá relation is an empirically derived $L_{\mathrm{H}\alpha} - L_{\mathrm{acc}}$ relation for a large number of T Tauri stars. For the known stellar companions HD 142527 B and HD 100453 B, we report only the Alcalá-derived accretion rates, as they fall solidly within the mass regime of that sample.

Mass accretion rates/limits ($\dot{M}$) are derived from total accretion luminosities (L_{acc}) via the standard relation

$$\dot{M} = \frac{1.25 L_{\mathrm{acc}} R}{GM}, \tag{4}$$

where M and R are the mass and radius of the accreting object (Gullbring et al. 1998). As the masses and radii of protoplanet candidates are poorly constrained or unconstrained, we report most accretion rates and limits as the product of M and $\dot{M}$ and adopt a global value of $2M_J$ for object radii, which is reasonable for a range of young substellar objects.

For the stellar companion HD 142527 B, we adopt a mass of $0.26\,M_\odot$ and a radius of $1.2\,R_\odot$, following Balmer et al. (2022). For HD 100453 B, we adopt a mass of $0.2\,M_\odot$, following Collins et al. (2009), and estimate a radius of $0.5\,R_\odot$ based on the models of Baraffe et al. (2015) for a 15 Myr, $0.2\,M_\odot$ pre-main-sequence star.

In order to estimate uncertainty in derived accretion rates, we adopt the approach recommended in Aoyama et al. (2021), which uses the spread in the L_{acc}–$L_{\mathrm{H}\alpha}$ relation from their theoretical models instead of the formal error to place uncertainties on L_{acc}. We note that all $L_{\mathrm{H}\alpha}$ values estimated in this work lie in the $L_{acc} \lesssim 10^{-4} L_\odot$ regime, where the spread in their model relation increases substantially (to 1.5 dex) due to an increased optical depth at Hα. Combined with a $0.5 R_{\mathrm{Jup}}$ uncertainty on object radii, we estimate accretion rate uncertainties under these models of 2–3 dex.

For the empirical T Tauri stellar relation, Alcalá et al. (2017) reported a standard deviation of 0.41 dex around their best-fit L_{acc}–$L_{\mathrm{H}\alpha}$ scaling. Combined with ∼10% uncertainties on masses and radii, we estimate an uncertainty of ∼1 dex on accretion rates estimated under the Alcalá et al. (2017) relation.

In general, given the poorly constrained nature of young substellar objects' masses and radii, a limited understanding of which scaling relations are most appropriate in the substellar regime, and intrinsic photometric uncertainties, we caution that accretion rates should be interpreted as very rough estimates. Their utility lies primarily in comparison with one another; assuming all objects accrete material under the same paradigm, their *relative* accretion rates under a single accretion scaling relation should reflect reality.

6.3. Optimal KLIP Parameters

The products of our optimization processes (outlined in Sections 3.1. and 3.2) are, for each data set: (a) an optimal amount of data to discard to minimize contrast for a fixed choice of KLIP parameters, and (b) a set of values for the `pyKLIP` parameters `annuli`, `movement`, and `numbasis` designed to maximize the sum of all six normalized image quality metrics across some number of false planets injected into the continuum images between the IWA and control radius. In this section, we discuss trends in optimal parameters.

Optimal Data Quality Cuts—appear to be more often low than high, as only 19% ($n = 7$) were greater than 50%. Only 18% ($n = 7$) of data sets have an optimal data quality cut of 0%, indicating that a majority of GAPlanetS reductions are significantly improved by discarding some proportion of images.

Optimal `pyKLIP` *annuli*—values were also more commonly low, with 66% ($n = 24$) of the optimal `annuli` values at 10 or fewer.

Optimal `pyKLIP` *movement*— showed a strong preference for "aggressive" values of 1 ($n = 17$) or 2 ($n = 8$), with only 31% of the data sets ($n = 11$) showing an optimal `movement` of 3 or greater.

Optimal `pyKLIP` *numbasis*—values showed a peak at 20 KL modes ($n = 13$), with values of 50 and 100 somewhat less common ($n = 4$ and 2, respectively). Thirty-nine percent ($n = 14$) of data sets showed optimal KL mode values of 5 or fewer.

Somewhat surprisingly, none of these optimized parameters show clear trends with system (e.g., AO wavefront sensor binning), stellar (e.g., r'-band magnitude), or atmospheric (e.g., FWHM) variables.

6.4. Contrasts

As with any HCI survey, one of the principal products of GAPlanetS is detection limits for accreting protoplanets in all imaged systems. These curves are difficult to interpret in bulk for several reasons. First, achieved contrast is highly sensitive to both the guide star magnitude and atmospheric conditions. This is true to some extent for all AO systems, but is especially true at visible wavelengths. Achieved contrast also varies wildly from data set to data set in this regime, even for the same object (see Figure 1).

Nevertheless, the bulk contrast curves of the sample can give us a general grasp of performance for this first-generation accreting protoplanet survey and the limits that it places on the prevalence of objects with certain Hα contrast ratios embedded in transitional disk cavities, with the caveat that variable accretion will make these boundaries somewhat fuzzy. Figure 19 shows optimized contrast curves for the entire GAPlanetS sample colored by stars' r'-band magnitude.

The median achieved contrast for the survey as well as the best achieved contrast for each target at a range of separations from 0.″1–1.″5 is provided in Table 7.

6.5. Detection Rates

Computation of robust survey statistics for GAPlanetS is difficult, as this is not a large or unbiased sample, and the nature of some of the candidates is unclear. Nevertheless, the detection rate relative to other HCI surveys is striking and is a

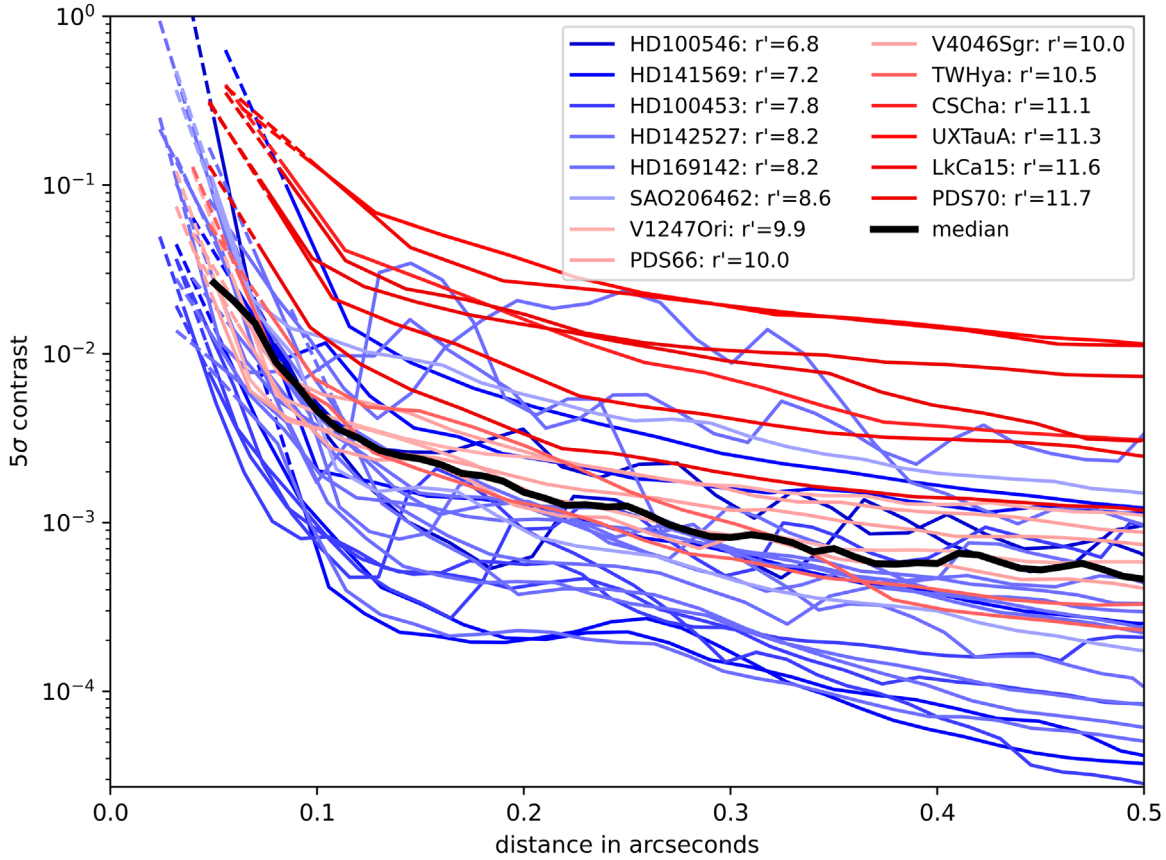

Figure 19. Contrast curves for all GAPlanetS datasets analyzed in this work. These curves were generated following our conservative survey methodology of optimizing on false continuum planets. Curves are colored by the *r*'-band magnitude of the star. While the specific contrast achieved for a given target varies widely with seeing, it is also a strong function of *r*'-band magnitude.

Table 7
GAPlanetS Best Achieved Contrast by Target from 0.″1 to1.″5 for

	Best Achieved Log Contrast						
	0.″1	0.″25	0.″50	0.″75	1.″00	1.″25	1.″50
Survey Median	−2.34	−2.90	−3.34	−3.45	−3.62	−3.69	−3.76
HD100546	−2.34	−2.89	−3.02	−3.25	−3.44	−3.40	−3.48
HD100453	−3.04	−3.41	−4.08	−4.27	−3.97	−4.32	−4.48
HD142527	−2.44	−3.15	−3.36	−3.43	−3.55	−3.65	−3.82
HD169142	−2.68	−3.03	−3.48	−3.70	−3.84	−3.94	−3.98
SAO206462	−2.26	−3.18	−3.76	−4.06	−4.25	−4.36	−4.41
V1247Ori	−2.44	−2.95	−3.24	−3.33	−3.42	−3.44	−3.46
HD141569	−1.95	−2.73	−2.94	−3.12	−3.42	−3.72	−3.94
V4046Sgr	−2.46	−3.01	−3.39	−3.64	−3.72	−3.73	−3.76
PDS66	−2.22	−2.71	−3.06	−3.24	−3.33	−3.36	−3.40
TWHya	−2.26	−3.06	−3.48	−3.58	−3.64	−3.69	−3.69
UXTauA	−0.88	−1.62	−1.94	−2.09	−2.17	−2.23	−2.27
CSCha	−1.09	−2.01	−2.51	−2.70	−2.75	−2.76	−2.80
LkCa15	−1.44	−2.30	−2.61	−2.69	−2.76	−2.76	−2.78
PDS70	−1.14	−1.92	−2.13	−2.30	−2.47	−2.62	−2.72

result of the highly targeted nature of the GAPlanetS sample (transitional disks; see Section 2). We detect two accreting stellar companions across our sample of 14 objects, one at very tight separation (HD 142527 B, ∼0.″1) and one more distant companion (HD 100453 B, ∼1″). We also detect four protoplanets or robust protoplanet candidates (PDS 70 b, PDS 70 c, LkCa 15 "b," and CS Cha "c") inside the cavities of three additional systems. This makes a total of five systems with accreting companion candidates out of 14 systems targeted, a detection rate of $\sim 36^{+26}_{-22}$% assuming binomial statistics.[16]

This is substantially higher than has been found by previous exoplanet direct imaging surveys in the NIR. In a meta-analysis of first-generation direct imaging survey results, Bowler &

[16] More specifically, the Wilson score interval with continuity correction for a detection rate of 0.36 gives a 95% confidence interval of [0.14,0.64].

Nielsen (2018) found that the occurrence rate for planets with masses ∼5–13M_J and separations ∼5–500 au was around 1%. More recently, the Gemini Planet Imager Exoplanet Survey (GPIES) detected nine companions (six planetary and three brown dwarf) in six systems among a sample of 300, yielding a planet occurrence rate estimate of 9^{+5}_{-4}% for planets between 5 and 13M_J and 10–100 au separation around stars greater than 1.5 solar masses. For brown dwarfs companions, GPIES yielded an even lower occurrence rate: only 0.8 $^{+5}_{-4}$ for brown dwarfs between 13 and 80$M_{\rm Jup}$ at 10–100 au (Nielsen et al. 2019).

GAPlanetS is not the only survey for protoplanets in the literature. Previously published Hα direct imaging surveys have yielded no new confirmed planets, though several have recovered HD 142527 B (Cugno et al. 2019; Zurlo et al. 2020) at high S/N, and/or present new yet-to-be-confirmed candidates (e.g., Cugno et al. 2019; Huélamo et al. 2022). The largest previous survey for accreting companions, which had similar selection criteria to GAPlanetS, was the 11-object VLT-SPHERE survey of Zurlo et al. (2020). They recovered HD 142527 B, but detected no new accreting candidates aside from HD98800 Ba, one of the stellar members of the HD 98800 BaBb circumbinary transitional disk and therefore akin to our (also accreting) central transitional disk host stars. They hypothesize that the prevalence of strong residual speckles in the inner 0.″2 of their post-processed images contributes to their low detection rate, and we note that three of the systems in which we have detected candidates are within this region. When expanding their sample to include three additional archival Hα observations, as well as PDS 70, their detection rate rises to 2/15 objects, or $\sim 13^{+29}_{-11}$% assuming binomial statistics, consistent with our detection rate within uncertainties.[17]

7. Conclusions

7.1. Summary of Results

In this work, we present observational results from the GAPlanetS HCI campaign, a targeted, multiepoch Hα adaptive optics study of 14 transitional disk systems with MagAO. Of these targets, we robustly recover previously reported accreting stellar and planetary companions/candidates in four systems: HD 100543, HD 142527, PDS 70, and LkCa 15. We do not recover Hα emission from previously reported planet candidates in five additional systems, namely: CS Cha (the "B" companion), HD 100546, HD 169142, SAO 206462, and TW Hya. In the remaining five systems (HD 141569, PDS 66, UX Tau A, V1247 Ori, and V4046 Sgr), we do not find evidence of accreting planetary-mass companions. We also report the detection of a single new accreting candidate companion, CS Cha "c," bringing the detection rate to 5/14, or ∼36% for the GAPlanetS sample.

While we do not detect many of the previously reported protoplanet candidates from the literature, we note that nondetections here do not speak to the robustness of those previous detections so much as to the limitations of our data. Even relatively high-mass protoplanets are likely to have accretion luminosities below our detection threshold (see Table 6) in many cases. Furthermore, very little small grain dust is required to extinct at Hα, so in the case of planet candidates that do not lie in highly cleared NIR cavities, Hα emission from protoplanets may be obscured by intervening small grain material. In other words, the absence of an Hα signal at the location of a candidate does not imply its nonexistence, or even that it is not accreting.

GAPlanetS results underscore the unique scientific capabilities and challenges of visible-light adaptive optics protoplanet imaging . Differential imaging that exploits the enhanced luminosity of emission lines from accreting companions is a powerful tool to isolate planetary signals and distinguish them from stellar and disk contributions. However, it is not without scientific and technical complexities, including challenges in distinguishing companion emission from reflected circumstellar disk light and mitigating the effects of extreme PSF variation across observations.

Similar to the eleven-target Hα transitional disk survey conducted by Zurlo et al. (2020), we are able to recover known accreting companions, but the discovery of new accreting systems is seemingly rare, even in these highly targeted disk systems that feature multiple signposts of planet formation. At the same time, this first-generation protoplanet survey achieved only moderate contrasts (10^{-2}–10^{-3}) in cleared disk regions for most of the targets in the sample, where only the most massive and actively accreting protoplanets are likely to be detectable (Mordasini et al. 2017). We also note the variable S/N of companion recoveries epoch to epoch, a likely result of both variations in observation quality and intrinsic accretion variability, which may explain the many nondetections of planet candidates associated with Hα searches like GAPlanetS.

On a more technical note, we use new systematic and robust methodologies of image post-processing optimization to improve PSF subtraction and contrast in visible light high-contrast imagery . We utilize a contrast-curve minimization strategy to select an optimal amount of raw data to discard prior to full post-processing analysis. We also implement a data-driven strategy to minimize false positives and recover only the most robust candidates, optimizing KLIP parameters for recovery of false planets injected into continuum images. We uniformly apply this technique to the full survey sample. This strategy removes the need for subjective parameter choices often made in direct imaging, without requiring a single uniform set of PSF subtraction parameters for the entire survey sample that may be poorly matched to some data sets. Our data demonstrate the need for a PSF subtraction methodology that is tuned to conditions (seeing, PSF variability, total rotation); our approach offers an unbiased method for conducting uninformed companion searches throughout a region of interest in HCI data. We find that this methodology can lead to both detections of new candidates and recoveries of previously known companions.

7.2. Future Work and Opportunities

Surveying transitional disks for Hα protoplanet emission remains a powerful and viable method to search for new exoplanets and conduct reconnaissance of the earliest stages of planet formation. To this end, future hardware improvements—i.e., the next-generation of SDI instrumentation—will greatly enhance our ability to discover and characterize such systems. New coronagraph technologies, faster wavefront control, and the use of customized beamsplitters to maximize Hα throughput are just some of the near-future improvements. The newly commissioned 2040 actuator MagAO-X high-

[17] More specifically, the Wilson score interval with continuity correction for a detection rate of 0.20 gives a 95% confidence interval of [0.02,0.42].

contrast visible light SDI imager (Males et al. 2020) should improve Hα contrasts by a factor of 10–100 over MagAO, particularly for brighter targets (Close 2020). As a result, the MagAO-X system will be able to place more stringent constraints on the population of protoplanets inside transitional disk gaps. Other visible light instruments are also performing quite well in this regime, including SCExAO's Visible Aperture Masking Polarimeter Imager for Resolved Exoplanetary Structures (VAMPIRES; Uyama et al. 2020) and SPHERE's Zurich Imaging Polarimeter (ZIMPOL; Schmid et al. 2018).

The improved stability of space-based facilities (e.g., HST, Roman) will also contribute significantly to our understanding of more distant accreting companions, and indeed has already begun to (e.g., Sanghi et al. 2022; Zhou et al. 2022).

On the ground and in space, hardware upgrades and improvements in algorithms for PSF subtraction and optimization will reveal many higher-contrast planetary accretion signals than reported here. The ability to detect lower-mass and/or more weakly accreting companions will in turn provide more, and more robust, tests of planet formation and accretion theories. The future of protoplanet imaging is bright.

We would like to thank the anonymous referee for providing supportive and constructive suggestions for improving this manuscript.

K.B.F., W.O.B., J.A., J.M., and C.S. acknowledge funding from NSF-AST-2009816. K.B.F.'s work on this project was also supported by a NASA Sagan fellowship. L.M.C.'s and K. B.F.'s work was supported in part by NASA Exoplanets Research Program (XRP) grants 80NSSC18K0441 and 80NSSC21K0397 and NSF-AAG-1615408. The MagAO system would not have been possible without construction support from the NSF MRI and ATI programs (MRI-0321312, ATI-1206422, ATI-1506818). W.O.B. thanks the LSSTC Data Science Fellowship Program, which is funded by LSSTC, NSF Cybertraining grant No. 1829740, the Brinson Foundation, and the Moore Foundation; their participation in the program has benefited this work. K.M.M.'s work has been supported by the NASA XRP by cooperative agreement NNX16AD44G. K.W. acknowledges support from NASA through the NASA Hubble Fellowship grant HST-HF2-51472.001-A awarded by the Space Telescope Science Institute, which is operated by the Association of Universities for Research in Astronomy, Incorporated, under NASA contract NAS5-26555.

This paper includes data gathered with the 6.5 m Magellan Telescopes located at Las Campanas Observatory, Chile. We thank T. J. Rodigas for his help in collecting some of the data reported in this work.

This work has made use of data from the European Space Agency (ESA) mission Gaia (https://www.cosmos.esa.int/gaia), processed by the Gaia Data Processing and Analysis Consortium (DPAC; https://www.cosmos.esa.int/web/gaia/dpac/consortium). Funding for the DPAC has been provided by national institutions, in particular the institutions participating in the Gaia Multilateral Agreement.

We would like to acknowledge the land that the observations used in this paper were taken from. Las Campanas Observatory, and the Magellan Clay Telescope, are built on Diaguita land. More on the Diaguita is available from the Museo Chileno de Arte Precolombino: http://precolombino.cl/en/culturas-americanas/pueblos-originarios-de-chile/diaguita/.

Facility: Magellan (MagAO).

Software: `astropy` (Astropy Collaboration et al. 2013, 2018), `emcee` (Foreman-Mackey et al. 2013), `photutils` (Bradley et al. 2020), `ptemcee` (Vousden et al. 2016), `pyklip` (Wang et al. 2015).

Appendix A
Individual Target Summaries

This appendix contains brief literature reviews for each of the 14 targets observed as part of the GAPlanetS Campaign. Targets are discussed in the order in which they appear in Section 5. The reviews focus on: (a) stellar age, mass, and moving group membership estimates, (b) disk morphological characteristics, and (c) previously reported direct and indirect evidence for planet candidates in these systems.

A.1. HD 142527

HD 142527 A is a young (5.0 ± 1.5 Myr; Mendigutía et al. 2014) transition disk host. Its Gaia DR3 position and motion (see Table 1) are consistent with membership in the Upper Centaurus Lupus star-forming region (membership probability of 92.10% per Banyan Σ; Gagné et al. 2018). The central star has a mass of $M_A = 2.0 \pm 0.3 M_\odot$ (Mendigutía et al. 2014) and is an F6III-V type Herbig Ae/Be star $R = 6$ mag (Ofek 2008). HD 142527 A is actively accreting (Mendigutía et al. 2014) from an unresolved inner disk that is likely replenished by gas flowing through the massive cavity (∼30 to ∼140 au; Avenhaus et al. 2014, 2017). At submillimeter wavelengths, the cavity shows complex spiral arm and horseshoe structures (e.g., Ohashi 2008; Boehler et al. 2017; Garg et al. 2021). Similarly complex and asymmetric scattered light structures (e.g., Fukagawa et al. 2006; Avenhaus et al. 2014; Hunziker et al. 2021) have also been observed in the NIR.

The low-mass stellar companion HD 142527 B was first detected via Sparse Aperture Masking at the Very Large Telescope at *H, K*, and *L*', and its mass estimated at $\sim$0.1–0.4$M_\odot$ via pre-main-sequence model fitting of its infrared photometry (Biller et al. 2012). The first noninterferometric direct detection of the low-mass stellar companion was made with MagAO in 2013 (Close et al. 2014). At a separation of just 86 mas, HD 142527 B was detected in both Hα and continuum emission using simple classical angular differential imaging. It was found to be 1.2 mag brighter at Hα than in the continuum. These data served as the first proof of concept that direct Hα emission from a companion could be isolated at $<0\farcs1$ separation with visible light HCI, and led to the development of the GAPlanetS campaign. For a full review of the literature surrounding the relationship between the HD 142527 B companion and the wide central cavity, see Balmer et al. (2022).

A.2. PDS 70

PDS 70 is a $0.82 M_\odot$ K7 star (Riaud et al. 2006). Its Gaia DR3 position and motion (see Table 1) are consistent with membership in the Upper Centaurus Lupus star-forming region (membership probability of 98.7% per Banyan Σ; Gagné et al. 2018). The companion PDS 70 b was discovered by Keppler et al. (2018) using SPHERE SHINE data in the *L*', *K*, and *H* bands, and subsequently recovered in archival NICI imagery. Comparison with various hot- and warm-start evolutionary models suggest a mass of between $5 M_J$ and $14 M_J$. Comparison

of PDS 70 b's location on the H-R diagram with pre-main-sequence evolutionary models suggest that the system has a significantly younger age (5.4 ± 1 Myr; Keppler et al. 2018) than is typical of Upper Centaurus Lupus (16 ± 2 Myr; Pecaut & Mamajek 2016). The companion was detected at a separation of 0.″195 (22 au), well inside the cleared central cavity of PDS 70.

A second companion, PDS 70 c, was detected first in Hα emission by Haffert et al. (2019), and then recovered in the NIR in reanalyzed VLT SPHERE observations by Mesa et al. (2019). Both planets were detected in VLTI/GRAVITY observations of the system by Wang et al. (2021b), who found that their orbital properties were consistent with being in 2:1 mean motion resonance. A compact submillimeter continuum signal suggestive of a circumplanetary disk has also been recovered with ALMA for PDS 70 c (Isella et al. 2019; Benisty et al. 2021), providing further evidence of its protoplanetary nature.

The transitional disk of PDS 70 has been resolved in both NIR scattered light (Hashimoto et al. 2012; Keppler et al. 2018) and in large grain thermal emission in the submillimeter (Hashimoto et al. 2015; Long et al. 2018). The NIR cavity extends to 0.″39, well beyond the observed location of PDS 70 b, and the submillimeter cavity extends even farther, to 0.″7 (Long et al. 2018). Long et al. (2018) also found evidence for an inner disk extending to ∼0.″11. The breadth of the PDS 70 cavity, as well as the variation in cavity radius with wavelength/grain size, is consistent with its nature as a multiplanetary system.

A.3. LkCa 15

LkCa 15 is a $1.25 \pm 0.10 M_{\odot}$ star (Donati et al. 2019) at a distance of 157.2 ± 0.7pc (GAIA DR3; Gaia Collaboration et al. 2022a). Its Gaia DR3 position and motion (see Table 1) are consistent with membership in the Taurus-Auriga star-forming region (membership probability of 88.2% per Banyan Σ; Gagné et al. 2018), though evolutionary model fits suggest an age of ∼5 Myr, somewhat older than the canonical age of Taurus-Auriga (1–2 Myr; Kenyon & Hartmann 2002).

Despite its very faint primary star, which makes natural guide star adaptive optics imaging difficult, the LkCa 15 system is among the most well-studied transitional disks because it was the first with a reported protoplanetary candidate inside of its disk gap. This object was first identified in NIR nonredundant masking (NRM) data by Kraus & Ireland (2012), and subsequently argued by Sallum et al. (2015) to have been at least two separate protoplanets (LkCa 15 "b" and "c") that were coincidentally aligned during the first detection epoch. Only one of those protoplanetary candidates (LkCa 15 b) was detected at Hα in the initial epoch, but both were detected in multiple LBT NRM epochs (Sallum et al. 2016). Another planet candidate, LkCa 15 d, was detected in one LBT epoch.

The system has a well-established inner cavity interior to ∼0.″3 (∼40 au; Thalmann et al. 2010, 2015, 2016; Currie et al. 2019). This cavity is not entirely cleared, however, as an inner disk component has been directly imaged in polarized scattered light in the optical with SPHERE ZIMPOL by Thalmann et al. (2015) and in the NIR with SPHERE IRDIS by Thalmann et al. (2016). Photometric and spectroscopic monitoring of LkCa 15 also suggests the presence of an inner accretion disk component near the corotation radius that is more highly inclined than the outer disk, as well as magnetospheric accretion funnels that impact the star at high latitudes, yielding an accretion rate of $7.4 \pm 2.8 \times 10^{-10} M_{\odot}/\,\mathrm{yr}^{-1}$ (Alencar et al. 2018).

A.4. HD 169142

HD 169142 is a $1.85 \pm 0.25 M_{\odot}$ F0V SpT star (Gratton et al. 2019) at a distance of 111.6 ± 0.4 pc (GAIA DR3; Gaia Collaboration et al. 2022a). This is significantly closer than its previously assumed 145 pc distance, and properties from the literature have been updated in this work to reflect this change where necessary. The Gaia DR3 position and motion of HD 169142 (see Table 1) do not suggest membership in a young moving group (99.9% probability of being a field star per Banyan Σ; Gagné et al. 2018), and its age is estimated at 6^{+6}_{-3} Myr (Grady et al. 2007). The mass accretion rate onto the primary star is estimated at $1.5\text{–}2.7 \times 10^{-9} M_{\odot}\ \mathrm{yr}^{-1}$ based on fits to the Paβ and Brγ lines obtained with SpeX on the IRTF (Wagner et al. 2015b).

The complex and asymmetric morphology of HD 169142 is highly consistent with the presence of multiple planets. The disk has a cleared central cavity at $r < 15$ au with a millimeter and NIR bright cavity rim at ∼20 au showing E/W asymmetry and suggesting a possible dust trap to the west of the star (Quanz et al. 2013; Osorio et al. 2014; Momose et al. 2015; Bertrang et al. 2018). The disk also hosts an annular gap from ∼30–55 au that is heavily depleted at millimeter wavelengths and less depleted in NIR scattered light and millimeter gas tracers (Momose et al. 2015; Fedele et al. 2017). The outer disk contains a second ring of large grain material extending from ∼55–85 au and a more extended small grain dust and gas disk that reaches ∼1.″2–1.″7 (∼200 au) (Quanz et al. 2013; Fedele et al. 2017). The outer dust ring was recently resolved with ALMA into three separate narrow rings at 57, 64, and 76 au (Pérez et al. 2019). The inner regions of the disk host several spiral arms resolved in scattered light (Gratton et al. 2019).

Given its morphological complexity, it is unsurprising that a number of point sources have been reported inside the cleared regions of the HD 169142 disk. In the inner dust cavity, Reggiani et al. (2014) reported a 12.2 ± 0.5 mag L' source at $0.″156 \pm 0.″032$ and a PA of $7.°4 \pm 11.°3$, and Biller et al. (2014) independently found an L' point source at a consistent location ($0.″11 \pm 0.″03$, PA $= 0° \pm 14°$), as well as another candidate at 0.″18 and PA of 33°. Ligi et al. (2018) imaged the disk in the NIR with VLT/SPHERE in both total and polarized intensity. In total intensity with ADI processing, they found several clumps at similar separation (∼0.″18), but the structures were fairly continuous in PDI and RDI imagery, suggesting that they may be part of an inhomogeneous dust ring at 0.″18. They also found a structure at 0.″10 consistent with the overlapping Reggiani et al. (2014) and Biller et al. (2014) L' candidate; however, it appeared extended at longer wavelengths, and they interpreted it as a potential second inner dust ring. This hypothesis is further supported by recent Keck/NIRC2 L' observations, which are consistent with an inner ∼7 au small grain dust ring (Birchall et al. 2019). The 0.″18 structures observed by Ligi et al. (2018) were followed up with SPHERE in Gratton et al. (2019) and shown to have astrometry consistent with Keplerian orbital motion. A new clump was also identified inside the outer annular gap at a separation of 0.″335 and a position angle of 35° exhibiting photometry consistent with a $\sim 2.2 M_J$ planet.

Potential circumplanetary disk detections have also been reported around HD 169142. Okamoto et al. (2017) observed an *N*-band mid-IR clump to the west of the star at $0\farcs116 \pm 0\farcs020$ and a PA of $250° \pm 5°$. In the outer annular gap, Osorio et al. (2014) reported a compact 5σ excess in 7 mm emission at a separation of $0\farcs34$ (PA $\sim$ 175) that they interpreted as a possible circumplanetary disk with an estimated mass of $\sim 0.6 M_J$.

Modeling of disk structures has also led to predictions for masses and locations of planets embedded in HD 169142. Kanagawa et al. (2015) estimated the mass of the planet clearing the 40–70 au gap to be $\geqslant 0.4 M_J$ based on an analytical relationship between planet mass and gap depletion, while Dong & Fung (2017) estimated the mass to be 0.2–2.1M_J from hydrodynamical + radiative transfer simulations of gap opening. Hydrodynamical modeling by Pérez et al. (2019) suggests that a single mini-Neptune ($M < 10_\oplus$) migrating inward from $\sim$69 to $\sim$64 au is consistent with the triple-ringed structure of the outer disk.

A.5. HD 100546

HD 100546 is an A0 star (Gray et al. 2017). Its Gaia DR3 position and motion (see Table 1) are consistent with membership in the Lower Centaurus Crux star-forming region (membership probability of 98.90% per Banyan Σ; Gagné et al. 2018) The disk around HD 100546 is morphologically complex, with evidence for an inner clearing, multiple spiral arms, and two planet candidates. The HD 100546 "b" protoplanet candidate was first reported by Quanz et al. (2013) and confirmed by Quanz et al. (2015) and Currie et al. (2015), but more recent attempts to recover the planet have failed (Rameau et al. 2017).

For a full review of the complex multiwavelength morphology of this disk and limits on candidate protoplanets in this system, see Follette et al. (2017). The GAPlanetS data for HD 100546 were analyzed in detail in Follette et al. (2017) and Rameau et al. (2017), but are revisited with improved processing in this study.

A.6. SAO 206462

SAO 206462, also referred to in the literature as HD 135344B, is a $1.7^{+0.2}_{-0.1} M_\odot$ F4Ve star (Müller et al. 2011) at a distance of 135 ± 0.4 pc (GAIA DR3; Gaia Collaboration et al. 2022a). Its Gaia DR3 position and motion (see Table 1) are consistent with membership in the Upper Centaurus Lupus star-forming region (membership probability 99.5% using Banyan Σ; Gagné et al. 2018), which has an age of 16 ± 2 Myr (Pecaut & Mamajek 2016). The disk hosts two potentially planet-induced spiral arms, first seen in scattered light by Muto et al. (2012).

Computational models with a massive outer companion have been shown to create qualitatively similar spiral features ($\sim 6 M_J$ at $r = 0\farcs6$ and PA $= 10°$, per Dong et al. 2015, $\sim 10 M_J$ at $\sim$100 au if S1 is the primary arm or $\sim 15 M_J$ at $\sim$150 au if S2 is primary, per Bae et al. 2016). However, direct imaging searches for the presence of massive perturbers in the outer disk of SAO 206462 have ruled out the presence of companions more massive than $\sim 6 M_J$ beyond the spirals, suggesting that the perturber is either located interior to the arms or is less massive than predicted (Maire et al. 2017).

At millimeter wavelengths, high-resolution ALMA imagery reveals a contiguous ring centered at $\sim 0\farcs4$, as well as a more distant azimuthally asymmetric dust crescent centered around $\sim 0\farcs6$ with multiwavelength properties consistent with predictions for dust vortices (Cazzoletti et al. 2018). The location of the millimeter overdensity is coincident with some predictions for the location of the perturber responsible for the S1 spiral arm (Muto et al. 2012; Stolker et al. 2016), suggesting that the arm may be incited by dust overdensity at this location (Pérez et al. 2014; Cazzoletti et al. 2018) rather than a point-source perturber. However, computational models have shown that planetary perturbers in the outer disk can also incite similar overdensities (Bae et al. 2016). van der Marel et al. (2016) constrained the large grain dust cavity wall to $\sim$40 au with a heavily depleted interior, but also show that the disk hosts a smaller gas cavity in ^{13}CO and C^{18}O that is heavily but not fully depleted (r $\sim$ 30 au as in the NIR, $\delta_{\rm gas} = 2 \times 10^{-4}$). The 10 au inconsistency in gap radii between large thermally emitting grains, NIR-scattering grains, and gas is suggestive of the presence of planets in the gap.

Casassus et al. (2021) imaged the disk in high-resolution J = (2-1) CO isotopologues and adjacent continuum, and in doing so, detected a fine continuum filament (sep $\sim 0\farcs468$, PA $\sim 216\fdg1$) connecting the inner disk and outer crescent. They also reanalyzed the NIR data from Stolker et al. (2017) to derive a best-fit location for the perturber, which they found to be radially shifted $0\farcs00421$ from the center of the filament.

Cugno et al. (2019) used SPHERE to search for Hα signals inside the disk gap of SAO 206462 and in the outer disk regions where, they point out, the presence of small dust grains is likely to heavily extinct Hα emission from any embedded planets. They place a limit of $< 2.4 \times 10^{-12} M_J\,{\rm yr}^{-1}$ for a $\sim 10.2 M_J$ planet (derived from the detection limit of Maire et al. 2017) at $0\farcs18$. They also reported a tentative detection of a low S/N point source at a separation of 71 mas and PA of 19°.

A.7. TW Hya

TW Hya is the nearest (60.1 ± 0.1 pc, GAIA DR3; Gaia Collaboration et al. 2022a) disk-bearing T Tauri star to Earth, and its Gaia DR3 position and motion (see Table 1) are consistent with membership in the eponymous TW Hya association (membership probability of 99.9% per Banyan Σ; Gagné et al. 2018). Pre-main-sequence model fits to the high-resolution NIR spectrum of TW Hya suggest that it is an M0.5 ($0.6 \pm 0.1 M_\odot$) star with an age of 8 ± 3 Myr (Sokal et al.2018).

High-resolution ALMA observations by Andrews et al. (2016) revealed concentric dark rings/gaps centered at 1, 24, 41, and 48 au, and fainter gaps at 13, 31, and 34 au. The sensitivity of their observations was such that disk emission was not detectable beyond $\sim$60–70 au.

The highest-resolution scattered-light images to date were reported in van Boekel et al. (2017). They revealed three concentric, moderately depleted (50%–80%) scattered light gaps centered at $\sim$7, $\sim$22, and $\sim$90au, as well as a spiral feature beyond the $\sim$90 au gap. Teague et al. (2019) searched for comparable structure in the gas disk and found spiral substructure in both the gas velocity and temperature maps.

Estimates for the masses of planets responsible for the $\sim$20 and $\sim$90 au scattered light gaps range from 0.05–0.5M_J and 0.01–3M_J, respectively (Rapson et al. 2015; Dong et al. 2017; van Boekel et al. 2017; Mentiplay et al. 2019). Results of the numerical simulations of Dong et al. (2017) suggested that the

shallow millimeter gaps at 41 and 48 au could be generated by a single $\sim 30 M_{\oplus}$ planet located between them at ~44 au, and Bae et al. (2017) suggested that the shock generated by a secondary planet-induced spiral arm might also carve the gap at ~20 au.

Recently, Tsukagoshi et al. (2019) reported the presence of a 12σ millimeter continuum excess located at 52 au and a PA of $-133°$ that they suggest is consistent with either a dust clump/vortex or a circumplanetary disk around a Neptune-mass planet, though there is no known gap at this location. Ilee et al. (2022) confirmed this with an 8σ detection of millimeter excess at nearly the same location.

A.8. HD 100453

HD 100453A is a Herbig A9.5Ve ($1.7 M_{\odot}$) star with an M4V stellar companion (HD 100453 B, $\sim 0.3 M_{\odot}$) at 1.″05 separation (Collins et al. 2009; Wagner et al. 2018b). The system, located at a distance of 103.8 ± 0.2pc (GAIA DR3; Gaia Collaboration et al. 2022a), has a Gaia DR3 distance and motion (see Table 1) consistent with membership in the 15 ± 3 Myr (Pecaut & Mamajek 2016) Lower Centaurus Crux association (membership probability of 99.3% per Banyan Σ; Gagné et al. 2018).

Scattered light imagery has revealed a depleted small grain dust cavity extending from the inner working angle of 0.″09 to ~0.″14, as well as striking spiral arm features and a number of time-variable "shadows" suggestive of an unresolved inner disk component that is misaligned with the outer disk (Benisty et al. 2016; Long et al. 2018). The disk is resolved in CO (2-1) line emission from 0.″23–1.″10. In scattered light, the spiral arms in the disk extend to 0.″37, and the inner ring of emission extends from 0.″18–0.″25 (Wagner et al. 2015a; van der Plas et al. 2019). Millimeter-continuum emission reveals an inner cavity extending from the resolution limit of 0.″09 to 0.″22, and an annular gap from 0.″40–0.″48. The observed spiral features are consistent with being driven by the known outer stellar companion HD 100453 B (Dong et al. 2016).

A.9. CS Cha

CS Chamaeleonis is a young 2 ± 2 Myr (Luhman 2004) spectroscopic binary system (Guenther et al. 2007) comprising two T-Tauri stars with spectral type K2Ve (Manara et al. 2014). Its distance of 168.8 ± 1.9 pc (GAIA DR3; Gaia Collaboration et al. 2022a) and sky position suggest membership in the Chamaeleon I association (Ginski et al. 2018).

CS Cha hosts a smooth, low-inclination disk with an outer radius of 0.″312 in polarized light ($i = 24.°2 \pm 3.°1$; Ginski et al. 2018) and a cavity that is estimated to lie interior to 18^{+6}_{-5} au based on SED modeling (Ribas et al. 2016).

The CS Cha system contains a comoving polarized ($13.7\% \pm 0.4\%$ in J-band) companion, CS Cha B, which lies beyond the outer radius of the circumbinary disk, at a projected separation of 1.″19 (Ginski et al. 2018). In order to explain the photometry of the system, Ginski et al. (2018) originally proposed that the companion was either a heavily extincted brown dwarf ($\sim 20 M_{\rm jup}$) or a planetary-mass companion with an unresolved disk or dust envelope; however, follow-up observations with with VLT MUSE by Haffert et al. (2020) suggested that CS Cha B is more likely a heavily disk-obscured mid-M type stellar companion ($M = 0.07$–$0.71 M_{\rm odot}$). They resolved the Hα emission line of the companion and found that CS Cha B is actively accreting, with an estimated accretion rate of $4 \times 10^{-11 \pm 0.4} M_{\odot}$ yr^{-1}. They estimate the continuum brightness of the companion at ~10 mag fainter than the primary (a contrast of 10^{-4}).

A.10. HD 141569

HD 141569A is a young (~5 Myr; Merín et al. 2004), $2.39^{+0.04}_{-0.05}$ $M_{\odot}$ (White et al. 2016), Herbig A2Ve star (Gray et al. 2017) at a distance of 111.6 ± 0.4 pc (Gaia Collaboration et al. 2022a). Its Gaia DR3 position and motion (see Table 1) do not suggest membership in a young moving group (99.9% probability of being a field star per Banyan Σ; Gagné et al. 2018). Aarnio et al. (2008) conducted a search for a comoving group for HD 141569 and found that the system likely formed in isolation. HD 141569A is the primary star of a hierarchical triple with two M-dwarf companions that lie ~9″ beyond the circumstellar disk.

The disk of HD 141569A is generally classified as a debris disk (Hughes et al. 2018), and it is significantly depleted in millimeter grains (Wyatt et al. 2015). It has four concentric scattered-light gaps between 0.″25–0.″4, 0.″43–0.″52, 0.″60–0.″69, and 1.″0–2.″0 (Konishi et al. 2016; Perrot et al. 2016), as well as a narrow ring of millimeter emission centered at 2.″0. The distribution of ^{13}CO (2-1) gas emission in the system is asymmetrical, with a peak 1.″1 from the star at a PA of $\sim -36°$ (Miley et al. 2018).

A.11. PDS 66

Also known as MP Mus, PDS 66 is a K1Ve (da Silva et al. 2009) $1.4 \pm 0.1 M_{\odot}$ (Avenhaus et al. 2018) star with Gaia DR3 position and motion (see Table 1) consistent with membership in the 15 ± 3 Myr (Pecaut & Mamajek 2016) Lower Centaurus Crux association (membership probability of 97.5% per Banyan Σ; Gagné et al. 2018). It should be noted that previously reported distance measurements are significantly different (~10 pc) than the most recent Gaia distance of 97.9 ± 0.1 pc (GAIA DR3; Gaia Collaboration et al. 2022a). The moderately inclined ($i = 31° \pm 2°$) disk surrounding PDS 66 has a resolved small grain dust gap from 0.″46–0.″81, as reveled in NIR polarized intensity imagery (Wolff et al. 2016). Kastner et al. (2010) used the CO line emission profile to constrain the gas disk's outer radius to ≈120 au. Cortes et al. (2009) detected 3 mm and 12 mm continuum emission toward PDS 66; however, it has not yet been resolved.

A.12. UX Tau A

UX Tau A is a K2Ve star with two companions: UX Tau B at ~5.″8 (itself a tight binary with ~0.″1 separation) and UX Tau C at ~2.″7 (Kraus & Hillenbrand 2009; Schaefer et al. 2014). The system, at a distance of 142.2 ± 0.7 pc (GAIA DR3; Gaia Collaboration et al. 2022a), has Gaia DR3 position and motion (see Table 1) consistent with membership in the 1–2 Myr (Kenyon & Hartmann 2002) Taurus-Auriga Association (membership probability of 98.1% per Banyan Σ; Gagné et al. 2018).

Submillimeter Array images have revealed a disk of large grains with a cavity interior to ~0.″18, a peak near ~0.″23, and an outer extent of ~0.″34 (Andrews et al. 2011b). Submillimeter gas emission (CO (2–1) ALMA images; Akeson et al. 2019) traces these structures closely. HiCIAO polarimetric imaging of the disk suggests that it is moderately inclined

($i = 46° \pm 2°$) and extends from an IWA of 0.″16–0.″86, but the inner gap detected in thermal emission is not resolved (Tanii et al. 2012).

A.13. V1247 Ori

V1247 Orionis is a single F0V star with a mass of $1.86 \pm 0.02 M_{\odot}$ and an age of 7.4 ± 0.4 Myr (estimated from PMS evolutionary tracks; Kraus et al. 2013). It resides at a distance of 401.3 ± 3.2 pc (GAIA DR3; Gaia Collaboration et al. 2022a) within the ϵ Ori association (Caballero & Solano 2008).

In 2016, Ohta et al. (2016) observed the star in scattered light, detecting an arc-like structure at $0.''28 \pm 0.''09$ spanning position angles from 60°–210° . Kraus et al. (2017) used ALMA to resolve the disk in 870 μm continuum, CO 3-2, and $H_{12}CO$ 4-3 emission. These images revealed an asymmetrical crescent at a separation of 0.″38. The arc-like structure revealed in Ohta et al. (2016) lies interior to the millimeter arc and may represent an accretion stream onto a planet. Kraus et al. (2017) hypothesized that this emission represents a spiral arm inclined relative to the inner disk by approximately 17°, and simulations assuming a planet mass of 3 $M_{\rm Jup}$ were able to reproduce these features to high accuracy.

A.14. V4046 Sgr

V4046 Sagittarii is a young binary system composed of two K-type T Tauri stars (K5Ve/K7Ve, 0.9/0.85 $M_{\odot}$; Nefs et al. 2012; Czekala et al. 2015) at a distance of 71.5 ± 0.1pc (GAIA DR3; Gaia Collaboration et al. 2022a) with Gaia DR3 position and motion (see Table 1) consistent with membership in the 24 ± 3 Myr (Bell et al. 2015) β Pictoris association (membership probability of 98.4% per Banyan Σ; Gagné et al. 2018).

The disk was imaged in 15 molecular gas tracers by Kastner et al. (2018), who found that the morphology varied by spectral line. Some tracers exhibited sharp (e.g HC_3N and C_2H) or diffuse (e.g., DCN, $H^{13}CO^{+}$) ring-like features, while others showed smooth disks (e.g., CO, HCN) with detectable emission extending as far as 4.″0 (^{12}CO). Scattered light images reveal a cavity interior to 0.″19 and a brighter northern edge (Rapson et al. 2015). In 1.3 mm continuum, a narrow ring-like feature has been identified at 0.″18 and a thicker outer ring from 0.″34–0.″84 (Martinez-Brunner et al. 2022).

Appendix B
Image Galleries for All Epochs

This appendix includes Figures 20-28, in which we provide Hα, Continuum, and SDI reductions (conservative and 1:1 scaled) for all GAPlanetS data sets not shown in the main text, sorted by object. Although we consider all of these data sets nondetections, we note that there are a number of $\geq 3\sigma$ point sources in many/most data sets. These sources were deemed less compelling in our survey analysis because they either (a) appear in SDI imagery without a clear Hα counterpart, or (b) do not appear in a consistent location in epochs that are closely spaced in time and similar in quality. At the same time, given the variable image quality and stochastic nature of accretion processes, we note that nondetection in subsequent epochs is not equivocal proof of a false positive. We provide full reductions of all data sets here for future reference, as some of these candidates may prove to be bona fide companions.

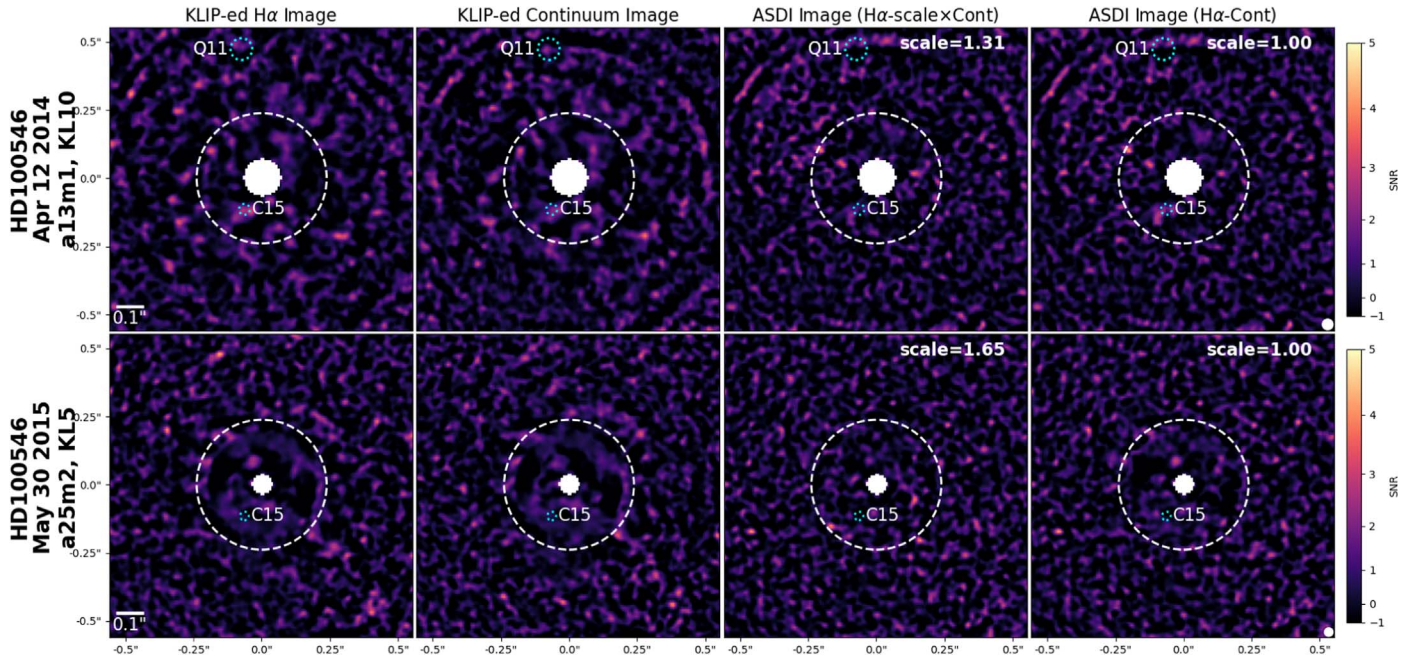

Figure 20. Final KLIPed Hα (left), Continuum (middle left), stellar Hα/continuum-scaled ASDI (middle right) and 1:1 scaled ASDI (right) imagery for both HD 100546 epochs. `pyKLIP` reduction parameters (indicated in the text labels to the left of each image panel) have been optimized for recovery of false continuum planets injected between the IWA and control radius, as described in detail in the text. The AO control radius of the images is indicated with a white dashed circle. The Currie et al. (2015) and Quanz et al. (2013) planet candidate locations at the original detection epochs are marked with dashed cyan circles labeled "C15" and "Q11," respectively

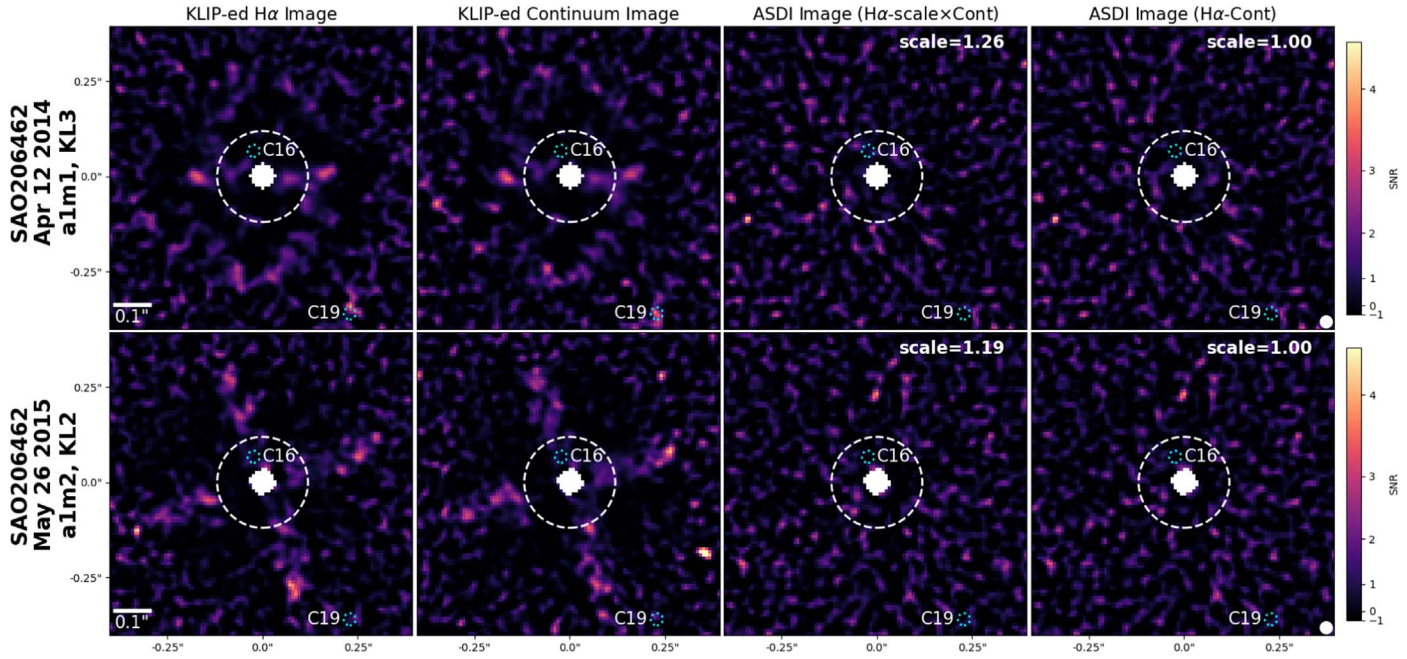

Figure 21. Final KLIPed Hα (left), Continuum (middle left), stellar Hα/continuum-scaled ASDI (middle right), and 1:1 scaled ASDI (right) imagery for both SAO 206462 epochs. `pyKLIP` reduction parameters (indicated in the text labels to the left of each image panel) have been optimized for recovery of false continuum planets injected between the IWA and control radius, as described in detail in the text. The AO control radius of the images is indicated with a white dashed circle. The Cugno et al. (2019) and Casassus et al. (2021) planet candidate locations at the original detection epoch are marked with dashed dashed cyan circles labeled "C16" and "C19," respectively.

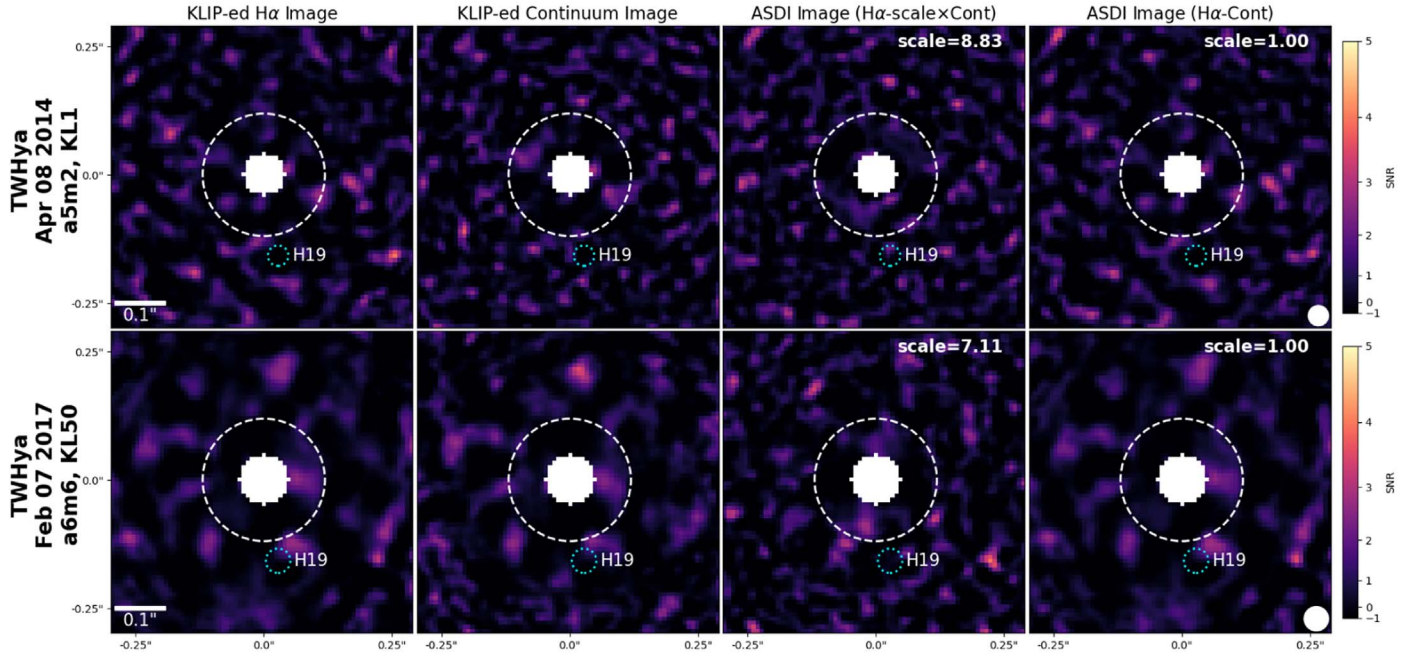

Figure 22. Final KLIPed Hα (left), Continuum (middle left), stellar Hα/continuum-scaled ASDI (middle right), and 1:1 scaled ASDI (right) imagery for both TW Hya epochs. `pyKLIP` reduction parameters (indicated in the text labels to the left of each image panel) have been optimized for recovery of false continuum planets injected between the IWA and control radius, as described in detail in the text. The AO control radius of the images is indicated with a white dashed circle. The Huélamo et al. (2022) point-source candidate (a suspected artifact according to the authors) is marked with a dashed cyan circle labeled "H19."

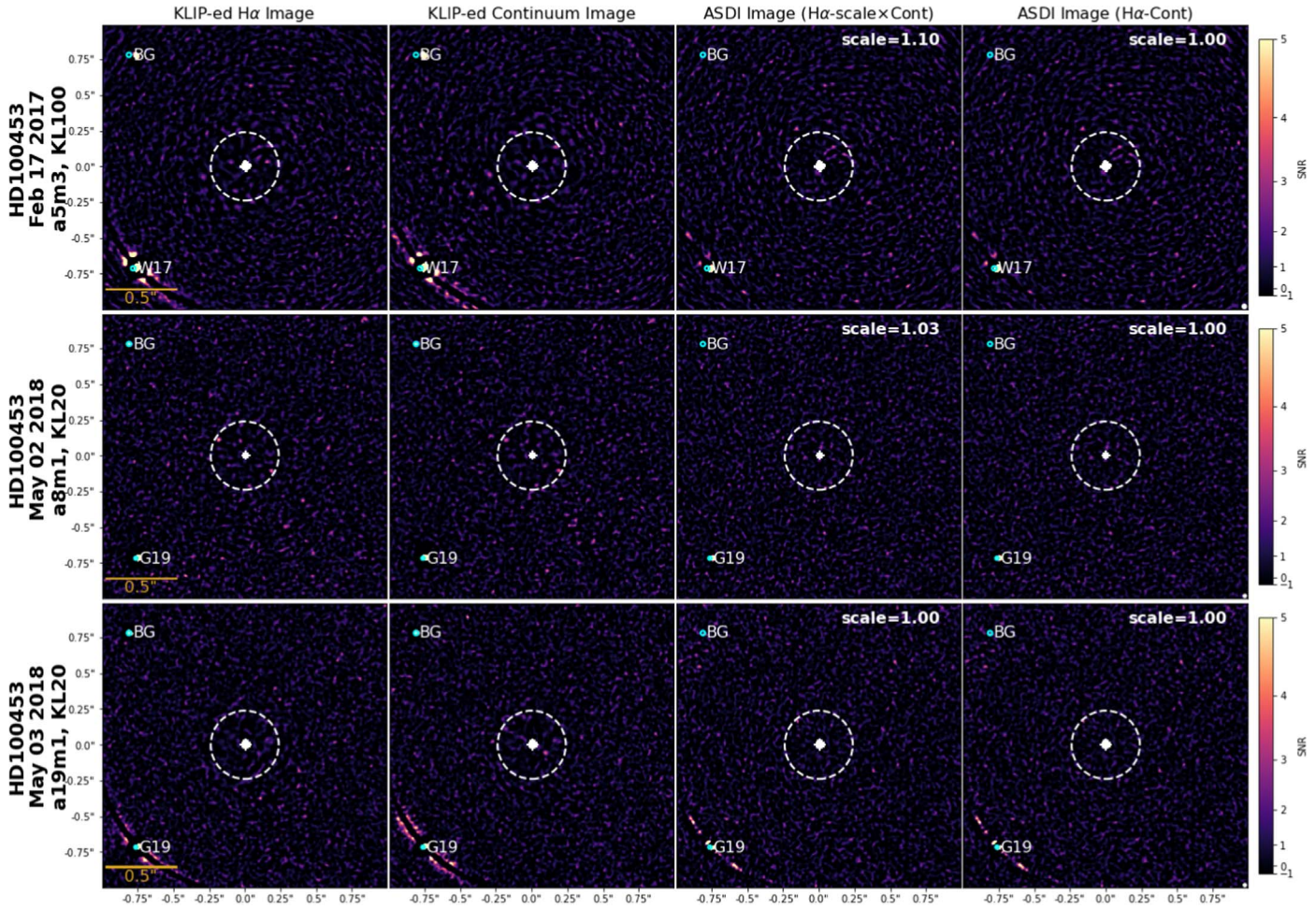

Figure 23. Final KLIPed Hα (left), Continuum (middle left), stellar Hα/continuum-scaled ASDI (middle right), and 1:1 scaled ASDI (right) imagery for all three HD 100453 epochs. `pyKLIP` reduction parameters (indicated in the text labels to the left of each image panel) have been optimized for recovery of false continuum planets injected between the IWA and control radius, as described in detail in the text. The AO control radius of the images is indicated with a white dashed circle. The companion HD 100453 B, is clearly visible in the lower left of each image panel, and its locations from Wagner et al. (2018b) and Gonzalez et al. (2020) are marked with cyan circles labeled "W17" and "G19," respectively. A known background star lies in the upper left-hand corner of each Hα and Continuum image (except in the 2018 May 2 epoch, when it is saturated and therefore not completely removed through SDI subtraction), but is absent in the SDI imagery because it is not actively accreting .

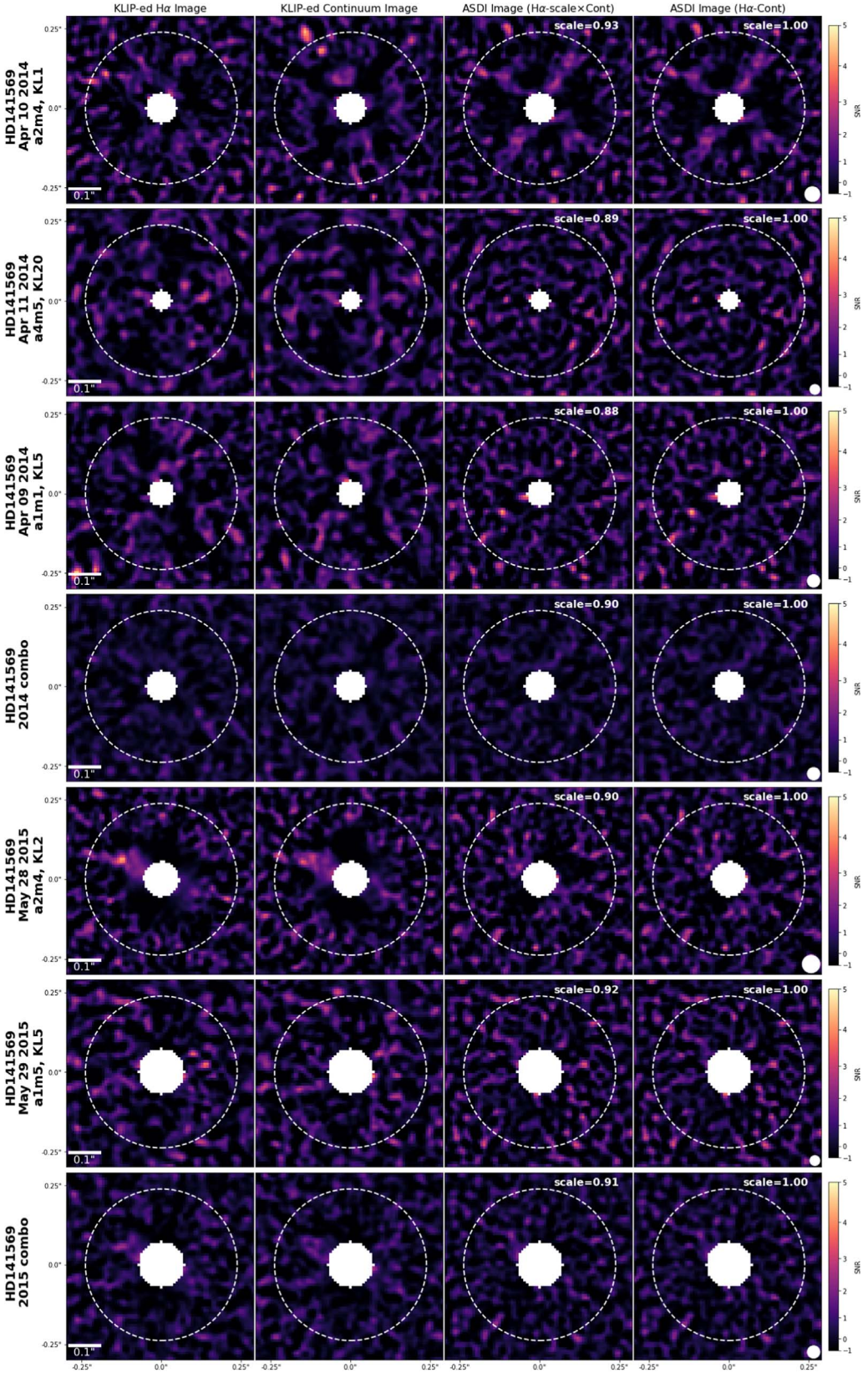

Figure 24. Final KLIPed Hα (left), Continuum (middle left), stellar Hα/continuum-scaled ASDI (middle right), and 1:1 scaled ASDI (right) imagery for all five HD 141569 epochs, as well as the combination of the three 2014 epochs (fourth panel) and the two 2015 epochs (seventh panel). `pyKLIP` reduction parameters (indicated in the text labels to the left of each image panel) have been optimized for recovery of false continuum planets injected between the IWA and control radius, as described in detail in the text. The AO control radius of the images is indicated with a white dashed circle.

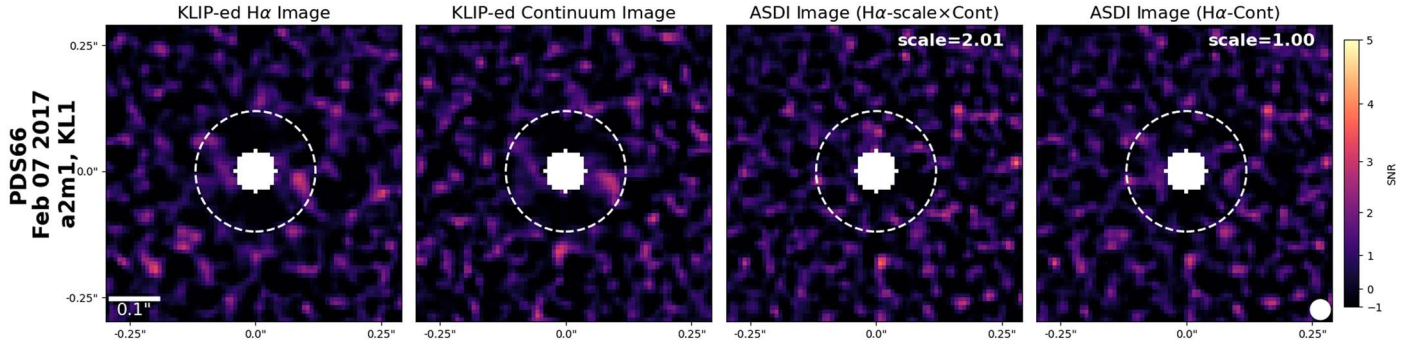

Figure 25. Final KLIPed Hα (left), Continuum (middle left), stellar Hα/continuum-scaled ASDI (middle right), and 1:1 scaled ASDI (right) imagery for the single PDS$\sim$66 epoch. `pyKLIP` reduction parameters (indicated in the text labels to the left of the image panel) have been optimized for recovery of false continuum planets injected between the IWA and control radius, as described in detail in the text. The AO control radius of the images is indicated with a white dashed circle.

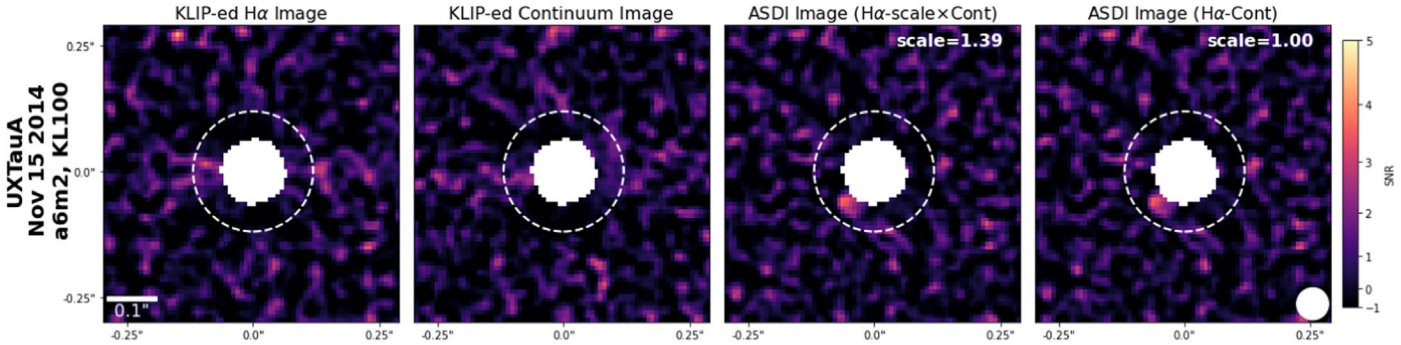

Figure 26. Final KLIPed Hα (left), Continuum (middle left), stellar Hα/continuum-scaled ASDI (middle right), and 1:1 scaled ASDI (right) imagery for the single UX Tau A epoch. `pyKLIP` reduction parameters (indicated in the text labels to the left of the image panel) have been optimized for recovery of false continuum planets injected between the IWA and control radius, as described in detail in the text. The AO control radius of the images is indicated with a white dashed circle.

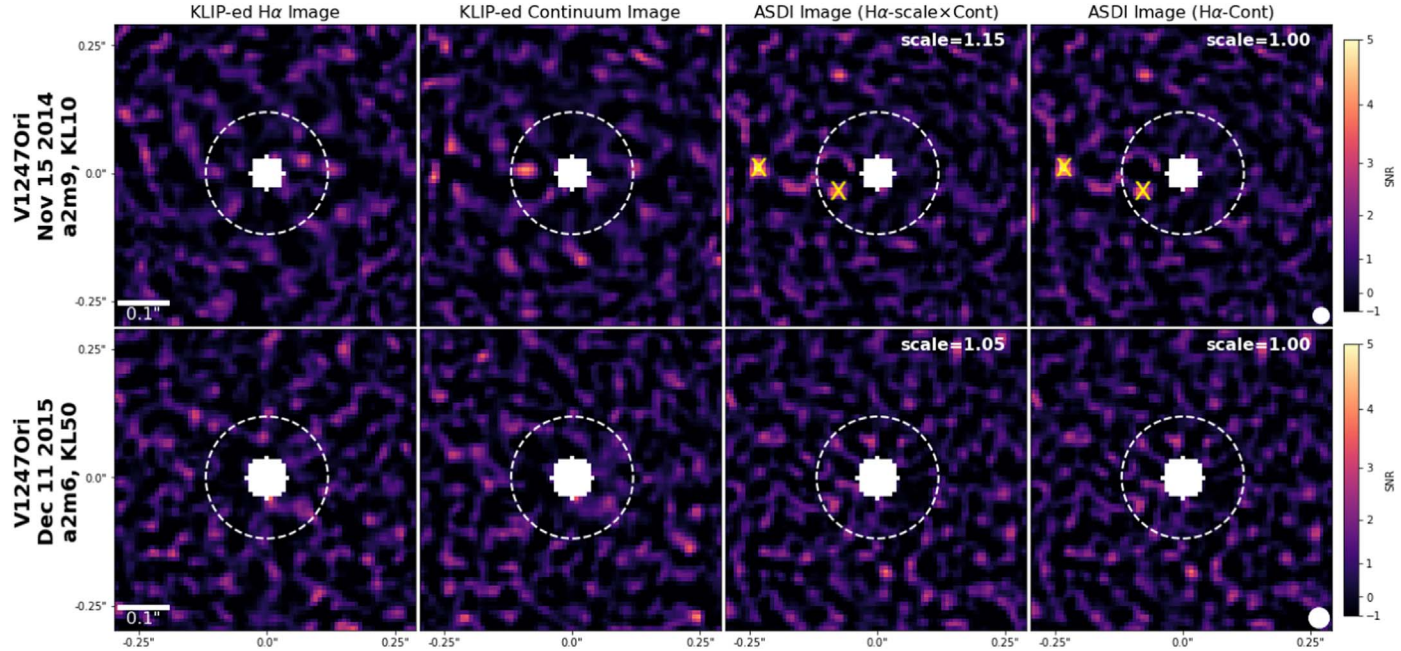

Figure 27. Final KLIPed Hα (left), Continuum (middle left), stellar Hα/continuum-scaled ASDI (middle right), and 1:1 scaled ASDI (right) imagery for both V1247 Ori epochs. `pyKLIP` reduction parameters (indicated in the text labels to the left of each image panel) have been optimized for recovery of false continuum planets injected between the IWA and control radius, as described in detail in the text. The AO control radius of the images is indicated with a white dashed circle.

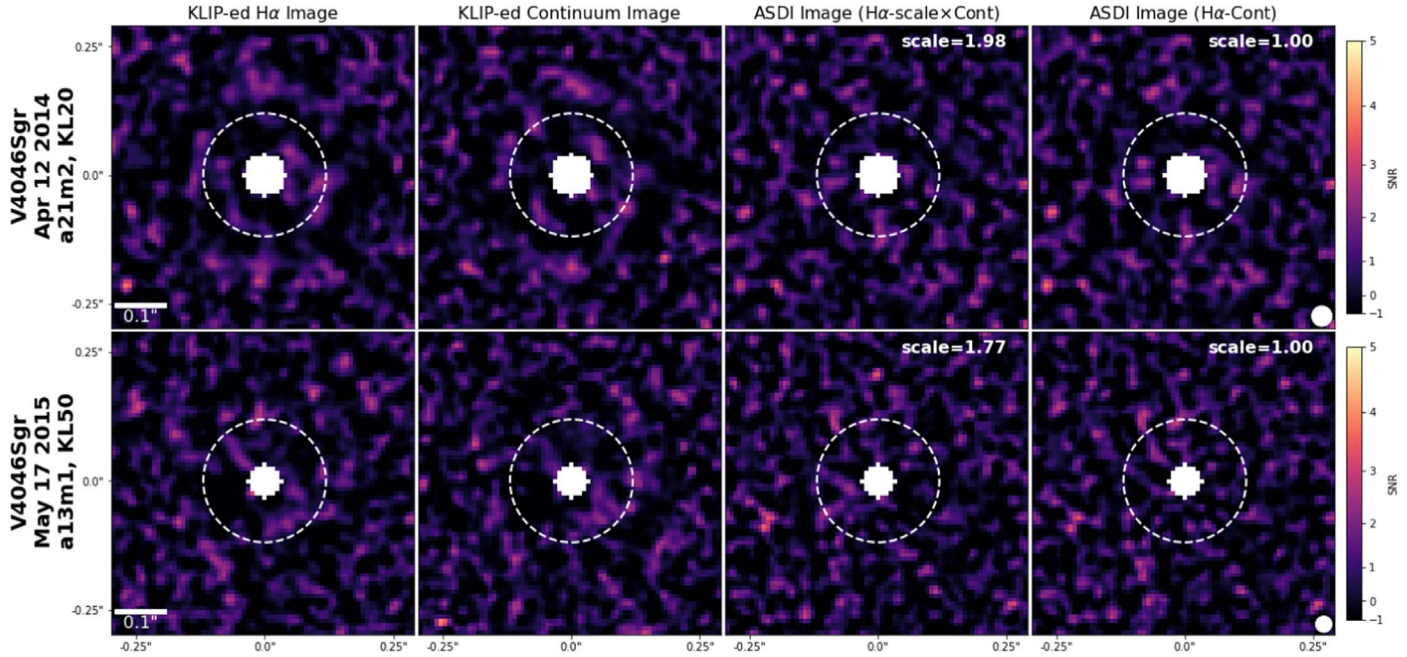

Figure 28. Final KLIPed Hα (left), Continuum (middle left), stellar Hα/continuum-scaled ASDI (middle right), and 1:1 scaled ASDI (right) imagery for both V4046 Sgr epochs. `pyKLIP` reduction parameters (indicated in the text labels to the left of each image panel) have been optimized for recovery of false continuum planets injected between the IWA and control radius, as described in detail in the text. The AO control radius of the images is indicated with a white dashed circle.

ORCID iDs

Katherine B. Follette https://orcid.org/0000-0002-7821-0695
Laird M. Close https://orcid.org/0000-0002-2167-8246
Jared R. Males https://orcid.org/0000-0002-2346-3441
Kimberly Ward-Duong https://orcid.org/0000-0002-4479-8291
William O. Balmer https://orcid.org/0000-0001-6396-8439
Jéa Adams Redai https://orcid.org/0000-0002-4489-3168
Julio Morales https://orcid.org/0000-0001-7525-7423
Robert J. De Rosa https://orcid.org/0000-0002-4918-0247
Fernando Garcia Toro https://orcid.org/0000-0002-0618-1119
Bruce Macintosh https://orcid.org/0000-0003-1212-7538
Katie M. Morzinski https://orcid.org/0000-0002-1384-0063
Helena Treiber https://orcid.org/0000-0003-0660-9776
Kevin Wagner https://orcid.org/0000-0002-4309-6343
Jason Wang (王劲飞) https://orcid.org/0000-0003-0774-6502
Alycia J. Weinberger https://orcid.org/0000-0001-6654-7859

References

Aarnio, A. N., Weinberger, A. J., Stassun, K. G., Mamajek, E. E., & James, D. J. 2008, AJ, 136, 2483
Adams Redai, J. I., Follette, K. B., Wang, J., et al. 2023, AJ, 165, 57
Akeson, R. L., Jensen, E. L. N., Carpenter, J., et al. 2019, ApJ, 872, 158
Alam, S., Albareti, F. D., Allende Prieto, C., et al. 2015, ApJS, 219, 12
Alcalá, J. M., Manara, C. F., Natta, A., et al. 2017, A&A, 600, A20
Alencar, S. H. P., Bouvier, J., Donati, J.-F., et al. 2018, A&A, 620, A195
Andrae, R., Fouesneau, M., Creevey, O., et al. 2018, A&A, 616, A8
Andrews, S. M., Rosenfeld, K. A., Wilner, D. J., & Bremer, M. 2011a, ApJL, 742, 1
Andrews, S. M., Wilner, D. J., Espaillat, C., et al. 2011b, ApJ, 732, 42
Andrews, S. M., Wilner, D. J., Zhu, Z., et al. 2016, ApJ, 820, L40
Aoyama, Y., Ikoma, M., & Tanigawa, T. 2018, ApJ, 866, 84
Aoyama, Y., Marleau, G.-D., Ikoma, M., & Mordasini, C. 2021, ApJL, 917, L30
Astropy Collaboration, Price-Whelan, A. M., Sipőcz, B. M., et al. 2018, AJ, 156, 123
Astropy Collaboration, Robitaille, T. P., Tollerud, E. J., et al. 2013, A&A, 558, A33
Appenzeller, I. 1977, A&A, 61, 21
Avenhaus, H., Quanz, S. P., Garufi, A., et al. 2018, ApJ, 863, 44
Avenhaus, H., Quanz, S. P., Schmid, H. M., et al. 2014, ApJ, 781, 87
Avenhaus, H., Quanz, S. P., Schmid, H. M., et al. 2017, AJ, 154, 33
Bae, J., Zhu, Z., & Hartmann, L. 2016, ApJ, 819, 134
Bae, J., Zhu, Z., & Hartmann, L. 2017, ApJ, 850, 201
Balmer, W. O., Follette, K. B., Close, L. M., et al. 2022, AJ, 164, 29
Baraffe, I., Homeier, D., Allard, F., & Chabrier, G. 2015, A&A, 577, A42
Bell, C. P., Mamajek, E. E., & Naylor, T. 2015, MNRAS, 454, 593
Benisty, M., Bae, J., Facchini, S., et al. 2021, ApJL, 916, L2
Benisty, M., Stolker, T., Pohl, A., et al. 2016, A&A, 42, 1
Bertrang, G. H., Avenhaus, H., Casassus, S., et al. 2018, MNRAS, 474, 5105
Bertrang, G. H. M., Flock, M., Keppler, M., et al. 2020, arXiv:2007.11565
Betti, S. K., Follette, K. B., Ward-Duong, K., et al. 2022, ApJL, 935, L18
Beuzit, J.-L., Feldt, M., Dohlen, K., et al. 2008, Proc. SPIE, 7014, 701418
Biller, B., Lacour, S., Juhász, A., et al. 2012, ApJL, 753, L38
Biller, B. A., Males, J., Rodigas, T., et al. 2014, ApJL, 792, L22
Birchall, E. K., Ireland, M. J., Federrath, C., et al. 2019, MNRAS, 486, 3721
Boehler, Y., Weaver, E., Isella, A., et al. 2017, ApJ, 840, 60
Bowler, B. P., & Nielsen, E. L. 2018, in Handbook of Exoplanets, ed. H. J. Deeg & J. A. Belmonte (Cham: Springer), 155
Bradley, L., Sipőcz, B., Robitaille, T., et al. 2020, astropy/photutils: v1.0.0, Zenodo, doi:10.5281/zenodo.4044744
Buchner, J. 2014, arXiv:1407.5459Stat Comput, 26, 383
Caballero, J. A., & Solano, E. 2008, A&A, 485, 931
Casassus, S., Christiaens, V., Cárcamo, M., et al. 2021, MNRAS, 507, 3789
Casassus, S., Marino, S., Pérez, S., et al. 2015, ApJ, 811, 92
Cazzoletti, P., van Dishoeck, E. F., Pinilla, P., et al. 2018, A&A, 619, A161
Cieza, L. A., Schreiber, M. R., Romero, G. A., et al. 2012, ApJ, 750, 157
Claudi, R., Maire, A. L., Mesa, D., et al. 2019, A&A, 622, A96
Close, L. M. 2020, AJ, 160, 221
Close, L. M., Follette, K. B., Males, J. R., et al. 2014, ApJL, 781, L30
Close, L. M., Males, J. R., Durney, O., et al. 2018, Proc. SPIE, 10703, 107034Y
Close, L. M., Males, J. R., Morzinski, K., et al. 2013, ApJ, 774, 94
Collins, K. A., Grady, C. A., Hamaguchi, K., et al. 2009, ApJ, 697, 557
Cortes, S. R., Meyer, M. R., Carpenter, J. M., et al. 2009, ApJ, 697, 1305
Coulson, I. M., & Walther, D. M. 1995, MNRAS, 274, 977

Cugno, G., Quanz, S. P., Hunziker, S., et al. 2019, A&A, 622, A156
Curran, R. L., Argiroffi, C., Sacco, G. G., et al. 2011, A&A, 526, A104
Currie, T., Cloutier, R., Brittain, S., et al. 2015, ApJL, 814, L27
Currie, T., Lawson, K., Schneider, G., et al. 2022, NatAs, 6, 751
Currie, T., Marois, C., Cieza, L., et al. 2019, ApJ, 877, L3
Czekala, I., Andrews, S. M., Jensen, E. L., et al. 2015, ApJ, 806, 154
da Silva, L., Girardi, L., Pasquini, L., et al. 2006, A&A, 458, 609
da Silva, L., Torres, C. A. O., de la Reza, R., et al. 2009, A&A, 508, 833
Dodson-Robinson, S. E., & Salyk, C. 2011, ApJ, 738, 131
Donati, J. F., Bouvier, J., Alencar, S. H., et al. 2019, MNRAS: Letters, 483, L1
Dong, R., & Fung, J. 2017, ApJ, 835, 146
Dong, R., Li, S., Chiang, E., & Li, H. 2017, ApJ, 843, 127
Dong, R., Rafikov, R., Zhu, Z., et al. 2012, ApJ, 750, 161
Dong, R., Zhu, Z., Fung, J., et al. 2016, ApJL, 816, L12
Dong, R., Zhu, Z., Rafikov, R. R., & Stone, J. M. 2015, ApJL, 809, L5
Duhalde, O., & Krzeminski, W. 1984, in European Southern Observatory Conf. and Workshop Proc. 18 (München: ESO), 119
Facchini, S., Benisty, M., Bae, J., et al. 2020, A&A, 639, A121
Fedele, D., Carney, M., Hogerheijde, M. R., et al. 2017, A&A, 600, A72
Fedele, D., Toci, C., Maud, L., & Lodato, G. 2021, A&A, 651, A90
Feroz, F., Hobson, M. P., & Bridges, M. 2009, MNRAS, 398, 1601
Follette, K. B., Rameau, J., Dong, R., et al. 2017, AJ, 153, 264
Follette, K. B., Tamura, M., Hashimoto, J., et al. 2013, ApJ, 767, 10
Foreman-Mackey, D., Hogg, D. W., Lang, D., & Goodman, J. 2013, PASP, 125, 306
Francis, L., & van der Marel, N. 2020, ApJ, 892, 111
Fried, D. L. 1978, JOSA, 68, 1651
Fukagawa, M., Tamura, M., Itoh, Y., et al. 2006, ApJL, 636, L153
Fung, J., Shi, J. M., & Chiang, E. 2014, ApJ, 782, 88
European Space Agency & DPAC Consortium 2022, Gaia Synthetic Photometry Catalogue (GSPC) (gaiadr3.synthetic_photometry_gspc), doi:10.17876/GAIA/DR.3/64
Gaia Collaboration, Vallenari, A., Brown, A. G. A., et al. 2022a, arXiv:2208.00211
Gaia Collaboration, Montegriffo, P., Bellazzini, M., et al. 2022b, arXiv:2206.06215
Gagné, J., Mamajek, E. E., Malo, L., et al. 2018, ApJ, 856, 23
Garcia Lopez, R., Natta, A., Testi, L., & Habart, E. 2006, A&A, 459, 837
Garg, H., Pinte, C., Christiaens, V., et al. 2021, MNRAS, 504, 782
Ginski, C., Benisty, M., van Holstein, R. G., et al. 2018, A&A, 616, A79
Golomb, J., Rocha, G., Meshkat, T., et al. 2019, AJ, 162, 304
Gonzalez, J.-F., van der Plas, G., Pinte, C., et al. 2020, MNRAS, 499, 3837
Grady, C. A., Schneider, G., Hamaguchi, K., et al. 2007, ApJ, 665, 1391
Gratton, R., Ligi, R., Sissa, E., et al. 2019, A&A, 623, A140
Gray, R. O., Riggs, Q. S., Koen, C., et al. 2017, AJ, 154, 31
Guenther, E. W., Esposito, M., Mundt, R., et al. 2007, A&A, 467, 1147
Gullbring, E., Hartmann, L., Briceño, C., & Calvet, N. 1998, ApJ, 492, 323
Haffert, S. Y., Bohn, A. J., de Boer, J., et al. 2019, NatAs, 3, 749
Haffert, S. Y., van Holstein, R. G., Ginski, C., et al. 2020, A&A, 640, L12
Hartmann, L., Herczeg, G., & Calvet, N. 2016, ARA&A, 54, 135
Hashimoto, J., Dong, R., Kudo, T., et al. 2012, ApJL, 758, L19
Hashimoto, J., Tsukagoshi, T., Brown, J. M., et al. 2015, ApJ, 799, 43
Herbig, G. H., & Goodrich, R. W. 1986, ApJ, 309, 294
Houk, N., & Smith-Moore, M. 1994, VizieR On-line Data Catalog:, III/133
Huélamo, N., Chauvin, G., Mendigutía, I., et al. 2022, A&A, 668, A138
Huélamo, N., Lacour, S., Tuthill, P., et al. 2011, A&A, 528, L7
Hughes, A. M., Duchêne, G., & Matthews, B. C. 2018, ARA&A, 56, 541
Hunziker, S., Schmid, H. M., Ma, J., et al. 2021, A&A, 648, A110
Ilee, J. D., Walsh, C., Jennings, J., et al. 2022, MNRAS, 515, L23
Isella, A., Benisty, M., Teague, R., et al. 2019, ApJL, 879, L25
Jovanovic, N., Martinache, F., Guyon, O., et al. 2015, PASP, 127, 890
Kanagawa, K. D., Muto, T., Tanaka, H., et al. 2015, ApJL, 806, L15
Kastner, J. H., Hily-Blant, P., Sacco, G. G., Forveille, T., & Zuckerman, B. 2010, ApJL, 723, L248
Kastner, J. H., Qi, C., Dickson-Vandervelde, D. A., et al. 2018, ApJ, 863, 106
Kenyon, S. J., & Hartmann, L. 2002, ApJS, 101, 117
Keppler, M., Benisty, M., Müller, A., et al. 2018, A&A, 617, A44
Konishi, M., Grady, C. A., Schneider, G., et al. 2016, ApJ, 818, L23
Kraus, A. L., & Hillenbrand, L. A. 2009, ApJ, 703, 1511
Kraus, A. L., & Ireland, M. J. 2012, ApJ, 745, 5
Kraus, S., Ireland, M. J., Sitko, M. L., et al. 2013, ApJ, 768, 80
Kraus, S., Kreplin, A., Fukugawa, M., et al. 2017, ApJ, 848, L11
Kurtovic, N. T., Pinilla, P., Penzlin, A. B. T., et al. 2022, A&A, 664, A151
Lafreniere, D., Marois, C., Doyon, R., Nadeau, D., & Artigau, E. 2007, ApJ, 660, 770
Lawson, K., Currie, T., Wisniewski, J. P., et al. 2022, ApJL, 935, L25
Ligi, R., Vigan, A., Gratton, R., et al. 2018, MNRAS, 473, 1774
Luhman, K. L. 2008, Handbook of Star Forming Regions, Vol II (Provo, UT: ASP Monograph Publications) doi:10.48550/arXiv.0808.3207
Long, Z. C., Akiyama, E., Sitko, M., et al. 2018, ApJ, 858, 112
Macintosh, B., Graham, J. R., Ingraham, P., et al. 2014, PNAS, 111, 12661
Maire, A. L., Stolker, T., Messina, S., et al. 2017, A&A, 601, A134
Males, J. R. 2013, PhD thesis, The Univ. Arizona
Males, J. R., Close, L. M., Guyon, O., et al. 2020, Proc. SPIE, 11448, 114484L
Males, J. R., Close, L. M., Miller, K., et al. 2018, Proc. SPIE, 10703, 1070309
Males, J. R., Close, L. M., Morzinski, K. M., et al. 2014, ApJ, 786, 32
Manara, C. F., Testi, L., Natta, A., et al. 2014, A&A, 568, A18
Marleau, G.-D., Mordasini, C., & Kuiper, R. 2019, ApJ, 881, 144
Martinez-Brunner, R., Casassus, S., Pérez, S., et al. 2022, MNRAS, 510, 1248
Mawet, D., Milli, J., Wahhaj, Z., et al. 2014, ApJ, 792, 97
Mendigutía, I., de Wit, W. J., Oudmaijer, R. D., et al. 2015, MNRAS, 453, 2126
Mendigutía, I., Fairlamb, J., Montesinos, B., et al. 2014, ApJ, 790, 21
Mendigutía, I., Oudmaijer, R. D., Schneider, P. C., et al. 2018, A&A, 618, L9
Mentiplay, D., Price, D. J., & Pinte, C. 2019, MNRAS, 484, L130
Merín, B., Montesinos, B., Eiroa, C., et al. 2004, A&A, 419, 301
Mesa, D., Keppler, M., Cantalloube, F., et al. 2019, A&A, 632, A25
Meshkat, T., Bailey, V., Rameau, J., et al. 2013, ApJL, 775, 1
Miley, J. M., Panić, O., Wyatt, M., & Kennedy, G. M. 2018, A&A, 615, L10
Milli, J., Mouillet, D., Lagrange, A.-M., et al. 2012, A&A, 545, A111
Momose, M., Morita, A., Fukagawa, M., et al. 2015, PASJ, 67, 2
Monnier, J. D., Harries, T. J., Aarnio, A., et al. 2017, ApJ, 838, 20
Mordasini, C., Marleau, G.-D., & Mollière, P. 2017, A&A, 608, A72
Morzinski, K., Close, L., Males, J., et al. 2013, in 3rd AO4ELT Conf.—Adaptive Optics for Extremely Large Telescopes 3, ed. S. Esposito & L. Fini (Florence: Arcetri Astrophysical Observatory),
Morzinski, K. M., Close, L. M., Males, J. R., et al. 2014, Proc. SPIE, 9148, 914804
Morzinski, K. M., Close, L. M., Males, J. R., et al. 2016, Proc. SPIE, 9909, 990901
Müller, A., Keppler, M., Henning, T., et al. 2018, A&A, 617, L2
Müller, A., van den Ancker, M. E., Launhardt, R., et al. 2011, A&A, 530, A85
Muto, T., Grady, C. A., Hashimoto, J., et al. 2012, ApJL, 748, L22
Nefs, S. V., Birkby, J. L., Snellen, I. A., et al. 2012, MNRAS, 425, 950
Nielsen, E. L., De Rosa, R. J., Macintosh, B., et al. 2019, AJ, 158, 13
Ofek, E. O. 2008, PASP, 120, 1128
Oh, D., Hashimoto, J., Tamura, M., et al. 2016, PASJ, 68, 1
Ohashi, N. 2008, Ap&SS, 313, 101
Ohta, Y., Fukagawa, M., Sitko, M. L., et al. 2016, PASJ, 68, 53
Okamoto, Y. K., Kataza, H., Honda, M., et al. 2017, AJ, 154, 16
Osorio, M., Anglada, G., Carrasco-González, C., et al. 2014, ApJL, 791, L36
Pascucci, I., Hollenbach, D., Najita, J., et al. 2007, ApJ, 663, 383
Pecaut, M. J., & Mamajek, E. E. 2013, ApJ, Supplement Series, 208, 9
Pecaut, M. J., & Mamajek, E. E. 2016, MNRAS, 461, 794
Pérez, L. M., Isella, A., Carpenter, J. M., & Chandler, C. J. 2014, ApJL, 783, L13
Pérez, S., Casassus, S., Baruteau, C., et al. 2019, AJ, 158, 15
Perrot, C., Boccaletti, A., Pantin, E., et al. 2016, A&A, 590, L7
Pineda, J. E., Szulágyi, J., Quanz, S. P., et al. 2019, ApJ, 871, 48
Pinilla, P., Benisty, M., Birnstiel, T., et al. 2014, A&A, 564, A51
Price, D. J., Cuello, N., Pinte, C., et al. 2018, MNRAS, 477, 1270
Quanz, S. P., Amara, A., Meyer, M. R., et al. 2015, ApJ, 807, 64
Quanz, S. P., Avenhaus, H., Buenzli, E., et al. 2013, ApJL, 766, L2
Rabago, I., & Zhu, Z. 2021, MNRAS, 502, 5325
Rameau, J., Follette, K. B., Pueyo, L., et al. 2017, AJ, 153, 244
Rapson, V. A., Kastner, J. H., Andrews, S. M., et al. 2015, ApJL, 803, L10
Reggiani, M., Christiaens, V., Absil, O., et al. 2018, A&A, 611, 10
Reggiani, M., Quanz, S. P., Meyer, M. R., et al. 2014, ApJL, 792, L23
Riaud, P., Mawet, D., Absil, O., et al. 2006, A&A, 458, 317
Ribas, A., Bouy, H., Merín, B., et al. 2016, MNRAS, 458, 1029
Robinson, C. E., & Espaillat, C. C. 2019, ApJ, 874, 129
Sallum, S., Eisner, J., Close, L. M., et al. 2016, Proc. SPIE, 9907, 99070D
Sallum, S., Follette, K. B., Eisner, J. A., et al. 2015, Natur, 527, 342
Salyk, C., Herczeg, G. J., Brown, J. M., et al. 2013, ApJ, 769, 21
Sanghi, A., Zhou, Y., & Bowler, B. P. 2022, AJ, 163, 119
Santamaría-Miranda, A., Cáceres, C., Schreiber, M. R., et al. 2018, MNRAS, 475, 2994
Schaefer, G. H., Prato, L., Simon, M., & Patience, J. 2014, AJ, 147, 157
Schmid, H. M., Bazzon, A., Roelfsema, R., et al. 2018, A&A, 619, A9
Sissa, E., Olofsson, J., Vigan, A., et al. 2018, A&A, 613, L6
Sitko, M. L., Day, A. N., Kimes, R. L., et al. 2012, ApJ, 745, 29

Sokal, K. R., Deen, C. P., Mace, G. N., et al. 2018, ApJ, 853, 120
Soummer, R., Pueyo, L., & Larkin, J. 2012, ApJL, 755, L28
Stolker, T., Dominik, C., Avenhaus, H., et al. 2016, A&A, 595, A113
Stolker, T., Sitko, M., Lazareff, B., et al. 2017, ApJ, 849, 143
Tanii, R., Itoh, Y., Kudo, T., et al. 2012, PASJ, 64, 1
Teague, R., Bae, J., Huang, J., & Bergin, E. A. 2019, ApJL, 884, L56
Thalmann, C., Grady, C. A., Goto, M., et al. 2010, ApJL, 718, L87
Thalmann, C., Janson, M., Garufi, A., et al. 2016, ApJL, 828, L17
Thalmann, C., Mulders, G. D., Janson, M., et al. 2015, ApJL, 808, L41
Thanathibodee, T., Molina, B., Calvet, N., et al. 2020, ApJ, 892, 81
Tsukagoshi, T., Muto, T., Nomura, H., et al. 2019, ApJ, 878, L8
Uyama, T., Norris, B., Jovanovic, N., et al. 2020, JATIS, 6, 045004
van Boekel, R., Henning, T., Menu, J., et al. 2017, ApJ, 837, 132
van der Marel, N., van Dishoeck, E. F., Bruderer, S., et al. 2016, A&A, 585, A58
van der Plas, G., Ménard, F., Gonzalez, J.-F., et al. 2019, A&A, 624, A33
Vieira, S. L. A., Corradi, W. J. B., Alencar, S. H. P., et al. 2003, AJ, 126, 2971
Villenave, M., Benisty, M., Dent, W. R. F., et al. 2019, A&A, 624, A7
Vousden, W. D., Farr, W. M., & Mandel, I. 2016, MNRAS, 455, 1919
Wagner, K., Apai, D., Kasper, M., & Robberto, M. 2015a, ApJ, 813, L2
Wagner, K. R., Sitko, M. L., Grady, C. A., et al. 2015b, ApJ, 798, 94
Wagner, K., Follete, K. B., Close, L. M., et al. 2018a, ApJ, 863, L8
Wagner, K., Dong, R., Sheehan, P., et al. 2018b, ApJ, 854, 130
Wang, J. J., Graham, J. R., Pueyo, L., et al. 2016, AJ, 152, 97
Wang, J. J., Kulikauskas, M., & Blunt, S. 2021a, whereistheplanet: Predicting positions of directly imaged companions, Astrophysics Source Code Library, ascl:2101.003
Wang, J. J., Vigan, A., Lacour, S., et al. 2021b, AJ, 161, 148
Wang, J. J., Ruffio, J.-B., De Rosa, R. J., et al. 2015, pyKLIP: PSF Subtraction for Exoplanets and Disks, Astrophysics Source Code Library, ascl:1506.001
Weinberger, A. J., Rich, R. M., Becklin, E. E., Zuckerman, B., & Matthews, K. 2000, ApJ, 544, 937
White, J. A., Boley, A. C., Hughes, A. M., et al. 2016, ApJ, 829, 6
Wichmann, R., Bastian, U., Krautter, J., Jankovics, I., & Rucinski, S. M. 1998, MNRAS, 301, L39
Willson, M., Kraus, S., Kluska, J., et al. 2019, A&A, 621, A7
Wolff, S. G., Perrin, M., Millar-Blanchaer, M. A., et al. 2016, ApJ, 818, L15
Wyatt, M. C., Panić, O., Kennedy, G. M., & Matrà, L. 2015, Ap&SS, 357, 103
Zhou, Y., Bowler, B. P., Wagner, K. R., et al. 2021, AJ, 161, 244
Zhou, Y., Herczeg, G. J., Kraus, A. L., Metchev, S., & Cruz, K. L. 2014, ApJL, 783, L17
Zhou, Y., Sanghi, A., Bowler, B. P., et al. 2022, ApJL, 934, L13
Zhu, Z., Nelson, R. P., Dong, R., Espaillat, C., & Hartmann, L. 2012, ApJ, 755, 6
Zurlo, A., Cugno, G., Montesinos, M., et al. 2020, A&A, 633, A119